



Université catholique de Louvain  
Secteur des Sciences et Technologies  
Institut de Recherche en Mathématique et Physique  
Center for Cosmology, Particle Physics and Phenomenology

---

## Measurements of two-photon interactions at the LHC

---

Doctoral dissertation presented by  
**Nicolas Schul**  
for the degree of Doctor in Sciences

Prof. K. Piotrkowski (Advisor)	UCLouvain
Prof. J-M. Gérard (Chairman)	UCLouvain
Prof. H. Jung	Deutsches Elektronen-Synchrotron
Prof. V. Lemaître	UCLouvain
Dr. C. Royon	C.E.A.-Saclay
Prof. P. Van Mechelen	Universiteit Antwerp

---

July 2011



# Remerciements

Le travail de recherche et de formation doctorale, dont le présent texte est l'aboutissement, n'a été rendu possible que grâce à une multitude d'apports extérieurs, et de soutien quotidien. Je voudrais tous vous en remercier ici.

Tout d'abord, mon promoteur Krzysztof qui m'a donné la possibilité de boucler cette aventure du doctorat, en me faisant confiance dès le départ, et en continuant d'insuffler de nouvelles idées et de fournir des conseils judicieux tout au long de ces cinq années. Je voudrais y associer les membres du comité d'accompagnement et de lecture pour leurs commentaires éclairés sur le texte.

Une part prépondérante du travail de recherche étant basée sur l'outil informatique, une aide essentielle a été fournie par toute l'équipe de CP3. Sans le support de Vincent, Jérôme, Pavel et Thomas auparavant, le travail quotidien aurait été très pénible. Merci pour leur savoir-faire, patience et persévérance afin de résoudre mes requêtes, toujours en un temps très court.

La qualité du travail effectué a été très probablement influencée positivement par l'environnement de travail exceptionnel au sein du centre CP3. Malheureusement, il y a ceux qui sont partis trop tôt et ceux qui sont arrivés trop tard pour que j'ai pu apprécier toute leur personnalité. Que ce soit une discussion sur le temps de midi ou en partageant un café de chez KafKaf, une plainte sur le sujet du séminaire du jeudi, une conversation dans le train de Louvain-la-Neuve à Ottignies, . . . tous ces moments ont contribué à la bonne humeur du labo. Un merci tout particulier à Loïc et Julien qui, en plus de leur délicieux humour, ont toujours répondu présents pour donner un coup de main.

Dans ce groupe, je ne saurais oublier mes deux plus proches collaborateurs Junhui et Jonathan. En vous contoyant tous les jours (dans le même bureau ou via e-mail) et en

travaillant sur les mêmes sujets, j'ai appris la vraie définition de collaboration. Merci à Jonathan d'avoir toujours répondu à toutes mes questions même les plus stupides, ainsi que pour son expérience en statistique. Mais surtout, grâce à vous deux, j'ai appris à apprécier deux cultures totalement différentes. . .

Pour finir, le plus grand remerciement devrait revenir au troisième étage en général et à Ginette en particulier, pour toutes ces petites tâches que vous faites tous les jours mais qui passent malheureusement trop souvent inaperçues à nos yeux.

Et puis il y a mon petit coeur. . . Finalement, s'il y bien quelqu'un qui m'a le plus soutenu pour la réalisation de ce travail, qui en a souffert et qui doit être remercié, c'est toi. Je ne crois pas avoir été assez reconnaissant pour tes sacrifices de soirées en solitaire ou de nuits commencées toute seule. Ni pour les week-ends et les vacances raccourcis parce que j'avais du travail. Néanmoins, tu n'as jamais manqué d'encouragement ou de tendresse pour moi dans ces moments-là.

# Contents

<b>Introduction</b>	<b>1</b>
<b>I The context</b>	<b>7</b>
<b>1 Motivation</b>	<b>9</b>
1.1 The purpose of the Large Hadron Collider . . . . .	9
1.2 A motivation for Supersymmetry . . . . .	13
1.3 Physics at the LHC . . . . .	15
1.4 First SUSY constraints from LHC . . . . .	19
<b>2 Photon interactions at the LHC</b>	<b>21</b>
2.1 Photon interactions at high energies . . . . .	21
2.1.1 Two-photon interaction . . . . .	22
2.1.2 Photo-production . . . . .	23
2.1.3 Diffractive photo-production . . . . .	24
2.2 The Equivalent Photon Approximation . . . . .	25
2.3 The LPAIR generator . . . . .	34
2.4 Central exclusive production as a background . . . . .	37

<b>II</b>	<b>The experimental tools:CMS and HPS</b>	<b>39</b>
<b>3</b>	<b>The Compact Muon Solenoid experiment at the LHC</b>	<b>41</b>
3.1	The Large Hadron Collider . . . . .	42
3.2	CMS detector overview . . . . .	43
3.3	Central sub-detectors . . . . .	47
3.4	Forward sub-detectors . . . . .	52
3.5	Event flow reconstruction . . . . .	54
3.5.1	Tracks . . . . .	55
3.5.2	Primary vertex . . . . .	55
3.5.3	Calorimeter towers . . . . .	56
3.5.4	Muon reconstruction . . . . .	56
3.6	Trigger system . . . . .	57
<b>4</b>	<b>The HPS and Gastof projects</b>	<b>61</b>
4.1	Physics with very forward detectors at the LHC . . . . .	61
4.2	High Precision Spectrometer detector overview . . . . .	63
4.3	HPS acceptance . . . . .	66
4.4	HPS background reduction . . . . .	71
4.5	Gastof as a fast timing detector . . . . .	77
4.5.1	GASTOF detector overview . . . . .	77
4.6	Ray tracing simulation . . . . .	80
4.6.1	Software details . . . . .	80
4.6.2	Reference design predictions . . . . .	84
4.6.3	Design variation . . . . .	87

<b>III</b>	<b>The measurements</b>	<b>93</b>
<b>5</b>	<b>Selection of the exclusive processes at the LHC</b>	<b>95</b>
5.1	Tagging exclusive processes at the LHC . . . . .	96
5.2	Calorimetry-based exclusivity conditions . . . . .	97
5.3	Track-based exclusivity conditions . . . . .	100
5.4	Pileup effect on track-veto . . . . .	105
<b>6</b>	<b>Measurements of exclusive dimuons with the CMS detector</b>	<b>109</b>
6.1	Exclusive dimuon final states phenomenology . . . . .	110
6.2	Event selection . . . . .	114
6.2.1	Trigger and muon selection . . . . .	114
6.2.2	Vertexing and tracking exclusivity . . . . .	114
6.2.3	Kinematic selection . . . . .	114
6.3	Data-driven efficiency correction . . . . .	117
6.3.1	Muons efficiency . . . . .	117
6.3.2	Tracking and Vertexing efficiency . . . . .	117
6.3.3	Pileup efficiency . . . . .	118
6.4	Observation of exclusive $\gamma\gamma \rightarrow \mu^+\mu^-$ . . . . .	118
6.5	Observation of $\gamma p \rightarrow \Upsilon p$ . . . . .	122
6.6	Observation of $\gamma p \rightarrow J/\Psi p$ . . . . .	126
<b>7</b>	<b>Absolute luminosity calibration</b>	<b>131</b>
7.1	LHC Luminosity determination . . . . .	131
7.2	Signal selection . . . . .	132
7.3	Systematic effects . . . . .	137
7.3.1	Pileup correction systematics . . . . .	137
7.3.2	Muon efficiencies . . . . .	138
7.3.3	Crossing angles . . . . .	138

7.3.4	Energy and momentum scale . . . . .	139
7.3.5	Tracking and vertexing efficiency . . . . .	139
7.3.6	Fit stability . . . . .	139
7.3.7	Backgrounds . . . . .	141
7.3.8	Fit systematics . . . . .	146
7.4	Results and prospects . . . . .	147
<b>IV The look forward</b>		<b>151</b>
<b>8</b>	<b>Two-photon exclusive production of supersymmetric pairs</b>	<b>153</b>
8.1	Two-photon production of SUSY pairs . . . . .	154
8.2	Detection of exclusive SUSY pairs . . . . .	155
8.3	Very forward detector information . . . . .	158
8.3.1	Two-photon invariant mass reconstruction . . . . .	158
8.3.2	Missing mass reconstruction . . . . .	159
8.3.3	Significance . . . . .	160
8.4	SUSY mass reconstruction . . . . .	162
8.5	Pileup effect . . . . .	162
8.6	Summary and prospects . . . . .	168
<b>Conclusion</b>		<b>173</b>
<b>A</b>	<b>Trigger muon paths</b>	<b>177</b>
<b>B</b>	<b>Ray Tracing plots</b>	<b>179</b>
<b>C</b>	<b>The LM1 supersymmetric benchmark point</b>	<b>185</b>
<b>Bibliography</b>		<b>193</b>





# Introduction

The first public results published recently on the analysis of data taken during 2010 at the CERN Large Hadron Collider (LHC) revealed the excellent performance of the detectors, the accuracy of their measurements and the good-control of the signal and background rates out of proton-proton collisions. Therefore, there is no doubt that if a yet-unprobed sector of the physics (Higgs, supersymmetry, . . .) is on their range of possible measurements, a discovery is "at the corner". On the contrary, the amount of statistics which will be recorded in 2011 would constitute a significant data sample to put strong constraints on new physics. At the sight of this success of the LHC, one might wonder was it the reason to devote a research thesis to the interactions between photons exchanged by beamline protons, especially when one knows that it constitutes only 1% of the total interactions. . .

However, as it will be demonstrated through the next chapters, two-photon interactions may play a important role in the next years at the LHC. On the one hand, as a powerful tool to **calibrate the total integrated luminosity** recorded by the experiments. This quantity, as it directly connects the cross-section (from the theory) and the event rate (from the experiment), is one of the most fundamental input used by the whole LHC scientific community. Although the value of the luminosity can be determined through other methods, the exclusive two-photon production of muon pairs remains one of the most accurate and reliable physics channel to measure it.

One the other hand, as a tool to **probe and to constrain new sectors in particle physics**. For instance, the detection of *new* charged pairs produced through two-photon interactions would allow for a precise and event-by-event measurement of the mass spectrum. This has to be put in contrast with the research in proton-proton interactions which own a larger discovery potential of *Beyond the Standard Model* physics, but would struggle to do precision measurements.

The advantages enjoyed by the two-photon produced events are driven by the **accurate knowledge of the cross-sections and kinematics** of these interactions, and the **striking experimental signature of exclusive pair production**. The first fact allows to predict precisely rates and physical distributions; so that any deviations from these expectations would be the sign of something 'new'. The second property makes it easy to detect such interactions: after the (elastic) photon exchange, the proton remains intact and is scattered at small angle. In exclusive two-photon interactions, the final state is therefore composed of two forward scattered protons, the pair of charged particles produced out the photons fusion and . . . nothing else!

However, it turned out to be that the "nothing else" is the most difficult to detect! In particular because two-photon interactions are occurring at the LHC with a configuration which favors simultaneous interactions within the same bunch-crossing, the famous *pileup* effect. The properties of this "nothing else", namely the **exclusivity conditions of the event**, are therefore one of the most difficult experimental characteristics to determine. One has to deal with many theoretical and experimental aspects: survival probability, inelastic photon-exchange, forward coverage, calorimeter noise, low- $p_T$  track reconstruction, vertex position resolution, . . .

The possible upgrade of the CMS detector through the installation of **very forward detectors** a few hundred meters from the interaction point may however improve the situation in the near future. With such dedicated detectors, one may thus tag a photon interaction by the detection of the associated outgoing forward proton. The measurement of the proton energy loss, and hence the photon energy, would bring valuable extra information on the initial conditions of the event. This project, supported by the *High Precision Spectrometer* (HPS) collaboration, has finally a chance to be born during the next long LHC shutdown. Once more, pileup effect will play an important role as it may fake exclusive interactions when accidental proton hits in the forward regions occur simultaneously with a measurement in the central detector. One way to suppress this background consists in the measurement of the proton time of arrival in HPS, and to check consistency with the central measurement position with  $z$ -by-timing method. A prototype of **fast timing detector with  $\sim 10$  ps resolution**, GASTOF, has been built in Louvain-la-Neuve in the purpose of such measurements.

The study of these unusual interactions at hadron colliders has been conducted during the thesis through their different facets: Monte-Carlo simulation, phenomenology, detector commissioning, data processing, . . . to study the unique aspects of two-photon interactions. Among them:

1.  **$\gamma\gamma$  properties:** What are the expected rates of two-photon interactions at the LHC? What is the effect of inelastic photon-exchange ?
2. **Exclusivity conditions:** How to characterize exclusivity in a complex detector (CMS) at hadron collider (LHC)?
3. **Two-photon production of muon pair:** Is it possible to detect such events at the LHC, even with significant pileup interactions?
4. **Luminosity:** Is the  $pp \rightarrow p\mu^+\mu^-p$  process a good candidate to calibrate the luminosity as it is claimed in literature?
5. **HPS and new physics:** With the installation of very forward proton detectors, what kind of measurements are possible in  $\gamma\gamma$  which are not in nominal  $pp$  collisions?
6. **Timing detectors:** What is the rate of accidental background expected and how much can be suppressed ?

This thesis divided between in four main parts:

## I. The context

The general (and deliberately qualitative) state-of-the-art of the particle physics knowledge at startup of the LHC is presented. The advantages of two-photon interactions at hadron colliders are highlighted, and expected rates of  $\gamma\gamma$  interactions at  $\sqrt{s} = 14$  TeV ([1]) and 7 TeV (original) are derived. They serve as a base for the calculation of two-photon production cross-section, as for example for supersymmetric pairs subject of the last chapter.

Specific Monte-Carlo techniques for lepton pairs production are detailed. For the first time, the LPAIR generator is used in association with a dedicated simulation of the proton remnant to produce together elastic, single-inelastic and double-inelastic photons-exchange for the  $\gamma\gamma \rightarrow \mu^+\mu^-$  process studied later.

## II. The experimental tools

A large overview of the current and future detectors used to select events produced through two-photon interactions is compiled. It contains description of the CMS detector [2] with an emphasis on the sub-detectors and reconstruction schemes used in 2010 to select exclusive events in  $pp$  collisions.

For the future upgrade of CMS with very-forward stations [3], tagging acceptance is computed for the newly chosen location of  $\pm 240$  m. Besides the  $\gamma\gamma$  signal acceptance, a full study of the proton accidental hits background is performed for the first time considering the full HPS system [3, 4]. Reduction of the overlap background rate with GASTOF fast timing detector is taken into consideration, along with tests of detector design to optimize the timing resolution [5].

## III. The results

The experimental characterization of the exclusivity conditions within the CMS detector is developed in the first section of this part. Starting with the original idea to monitor the calorimetric tower noise for usage as a veto to inclusive events [6], it clearly shows that the LHC configuration with pileup is spoiling this method. Therefore, a completely new method establishing the exclusivity within the tracker only –thanks to specific vertexing and tracking selection– is presented.

The demonstration of the performance of these new techniques is achieved with the observation of the  $\gamma\gamma \rightarrow \mu^+\mu^-$  process with the CMS detector [7], among the data recorded in 2010 in pileup environment, for which data-driven efficiency corrections are calculated and applied to the LPAIR Monte-Carlo samples.

The separation of the elastic signal from other contributions is done thanks to a novel fit procedure, with a first application to the calibration of the 2010 integrated luminosity. Systematics related to exclusive process selection, signal extraction and experimental uncertainties are estimated separately.

## IV. The look forward

Finally, an exploratory research of the  $\gamma\gamma$  physics potential with the HPS detectors in the beamline is presented. Using predicted rates from first studies, double-tag acceptance of HPS derived previously, and the confirmation of the performance for detecting exclusive di-leptonic events, the two-photon production and detection of supersymmetric pairs are investigated [8].

An empirical method is implemented, aiming to reconstruct the SUSY mass spectrum with a few GeV resolution only. Overlap background effect is added to the study, together with some specific methods to suppress it, including with GASTOF detector [9].



## **Part I**

# **The context**



# Chapter 1

## Motivation

*“Big Bang machine scientists look to exotic findings”*

Reuter Press (May 2010)

### 1.1 The purpose of the Large Hadron Collider

The purpose of high-energy physics is the study of the building blocks of matter and the interactions between them. As a result of decades of research, an (almost) complete comprehension of the fundamental elements and their properties has been achieved. This is codified in the so-called *Standard Model* (SM). On the one hand, the constituents of the matter are point-like particles which can be grouped according to some principles of symmetry; on the other hand, their mutual interactions are driven by elementary forces which can be explained within the framework of gauge field theories.

All the particles can also be described as fields and their interactions as mediated by gauge fields. Since the fields are quantized, the interactions can also be thought as carried by particles. All the currently known matter and anti-matter particles can then be described by fermionic fields, while the interactions are represented by bosonic fields. The current scheme of classification, and the related issues, are listed afterward.

## The elementary interaction and matter particles

The bosonic sector of the SM contains three of the four elementary interactions and their respective 'force carrier': electromagnetic (mediated by the massless and neutral photon  $\gamma$ ), strong (mediated by 8 massless and color charged gluons  $g$ , acting on quarks only) and weak (mediated by massive bosons  $W^\pm$  and  $Z^0$ ). Indeed, it is not clear if at the quantum level the gravitational force is mediated by gauge field and thus can be described within this framework.

The fermionic sector contains the quarks and the fermions constituent of the matter. For each matter particle, it also exists an anti-matter particle with the same mass and life time but opposite quantum numbers (and consequently different electric charge). The **leptons** are composed of the electron ( $e^-$ ), muon ( $\mu^-$ ) and tau ( $\tau^-$ ), each having electric charge  $Q = -1$  and no color charge; and their corresponding neutrinos ( $\nu_e, \nu_\mu, \nu_\tau$ ) which have  $Q = 0$ .

Moreover, one can find six **quarks** namely up ( $u$ ), charm ( $c$ ), top ( $t$ ) with  $Q = 2/3$  and down ( $d$ ), strange ( $s$ ) and bottom ( $b$ ) with  $Q = -1/3$ . However, an important consequence of the QCD theory is the confinement of the quarks: quarks don't exist as free particles but are confined into colorless hadrons composed of one quark and one anti-quark, or three quarks, respectively called **meson** and **baryon**.

As set of particles in nature have shown similar properties, this suggests the existence of symmetries which, from a mathematical point of view, means use of group theory. The symmetry group of the Standard Model contains the gauge group  $SU(3)_C$  from the Quantum ChromoDynamics (QCD) theory describing the strong interactions between colored quark and gluons, and the group  $SU(2)_L \otimes U(1)_Y$  of the unified electroweak interactions proposed by Glashow, Weinberg and Salam (GSW), motivated by the experimental observation of maximal parity violation, and constructed with the gauge bosons  $B_\mu$  and  $W_\mu^i$ ,  $i = 1, 2, 3$ .

Classification of particles content in the GSW model is displayed in Table 1.1. Within each generation, 15 matter fields exist: 2  $L$  leptons, 1  $R$  lepton,  $2 \times 3$   $L$  quarks and  $2 \times 3$   $R$  quarks<sup>1</sup>. Right-handed neutrinos are not included in the theory.

The major problem in the GSW model is that all the fields in the considered lagrangian are massless and that any explicit mass term like  $m\bar{L}_L L_R$  is allowed without breaking

<sup>1</sup>the factor 3 is for the color

<b>Leptons</b>	1 <sup>st</sup>	2 <sup>nd</sup>	3 <sup>rd</sup>
$L_L$	$\begin{pmatrix} \nu_e \\ e^- \end{pmatrix}_L$	$\begin{pmatrix} \nu_\mu \\ \mu^- \end{pmatrix}_L$	$\begin{pmatrix} \nu_\tau \\ \tau^- \end{pmatrix}_L$
$E_R$	$e_R^-$	$\mu_R^-$	$\tau_R^-$
<b>Quarks</b>			
$Q_L$	$\begin{pmatrix} u \\ d' \end{pmatrix}_L$	$\begin{pmatrix} c \\ s' \end{pmatrix}_L$	$\begin{pmatrix} t \\ b' \end{pmatrix}_L$
$U_R$	$u_R$	$c_R$	$t_R$
$D_R$	$d_R$	$s_R$	$b_R$

Table 1.1: List of known elementary particles constituent of matter with their electro-weak quantum numbers. A similar table can be built for anti-matter, with anti-quarks and anti-leptons ( $\bar{u}, \bar{d}, e^+, \bar{\nu}_e, \dots$ ).

the gauge invariance and the renormalization of the theory. Any of the gauge fields in the theory can then be associated with the known gauge bosons. One possible solution to solve this problem is to introduce a spontaneous breaking of the electroweak symmetry.

### The Brout-Englert-Higgs mechanism

In order to introduce a spontaneous symmetry breaking and to solve the mass problem for fermions and gauge bosons, Brout and Englert [10] as well as Higgs [11] have postulated that these masses are generated dynamically through an interaction with a new complex scalar doublet field  $\phi$ , which is assumed to exist everywhere in the vacuum. They design the potential (the famous "Mexican hat" potential) so that the groundstate, i.e. the minimal potential energy, is non-zero and is reachable for any values of the phase  $\omega$  so there exists an infinity of equivalent groundstates ( $\phi = v e^{i\omega}$ ). As in quantum field theory only one vacuum state may exist, once a particular value of the phase is chosen, it cannot change locally. Therefore, a non-zero vacuum expectation value breaks the local gauge invariance.

When the electroweak interaction is imposed, a mixing between gauge boson states takes place. The  $W_\mu^i$  and  $B_\mu$  fields mix to give rise to four new gauge bosons  $W^\pm$ ,  $Z^0$  and  $\gamma$ .

## Hierarchy and fine-tuning problems of the SM

All the parameters of the SM, including the masses of the bosons  $W^\pm$ ,  $Z^0$  and  $\gamma$ , have been measured with high precision in various recent experiments and all theoretical predictions are in good agreement with the present data. However, the Higgs boson has not yet been discovered. As it can be seen on the left side of Figure 1.3, LEP searches have put an lower bound  $m_H \geq 114.4$  GeV at [12], and TEVATRON ones have excluded it for  $158 \leq m_H \leq 175$  GeV [13], both at 95% C.L. On the same figure, one can see that the fit of the electroweak precision data tends to favor a light Higgs boson mass ( $\Delta\chi^2 = 0$  for  $m_H = 95.7_{24.2}^{+30.6}$  GeV at 95% C.L.).

Anyway, if the Higgs exists, the radiative corrections to its mass-squared, which come at first order from the insertion of a fermion or boson loop in the Higgs propagation line (see Figure 1.1), diverge quadratically at high energy:

$$\Delta m_H^2 \simeq \mathcal{O}(\Lambda^2) + \dots$$

where  $\Lambda$  is the cut-off scale, i.e. the energy at which the integral is stopped to avoid quadratic divergence. If any new-physics scale is introduced, it can be considered as the unification scale  $\Lambda \simeq M_{Planck} \simeq 10^{19}$  GeV.

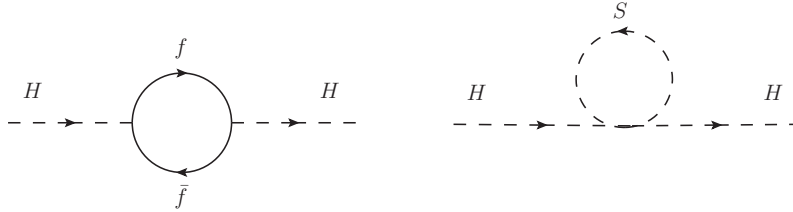


Figure 1.1: First order correction to the mass of the Higgs boson due to a loop of fermion (left) and boson (right).

This is part of the hierarchy problem of the SM: the mass of the Higgs tends to be near the highest scale of the theory while indirect experimental data shows the contrary. One possible solution consists in a fine-tuning of the parameters bringing to a cancellation between bosonic and fermionic loop. However, such a coincidence in the parameters appears extremely unnatural. Moreover, if one tries to calculate higher order corrections to  $m_H^2$ , the divergences reappear at each order of perturbative expansion and need a new fine-tuning of the parameters.

## 1.2 A motivation for Supersymmetry

One of the most popular theories assuming new physics at the TeV scale is the supersymmetry, usually abbreviated by SUSY. It postulates a symmetry between fermions and bosons, by assuming that each SM particle with a spin  $j$  has a supersymmetric partner with spin  $(j - \frac{1}{2})$ . The particle spectrum is then doubled and organized in supermultiplets: the **chiral** multiplets contain the spin 1/2 matter fields and their scalar partners; the **vector** multiplets contain the spin 1 gauge fields and their fermionic partners. All the particles in a supermultiplet have the same electric charge, weak isospin and color. Many theoretical, phenomenological and experimental arguments exist in favor of a such a symmetry upon the SM, among them:

- **SUSY solves the fine-tuning problem:**

The radiative correction to the Higgs boson mass-squared contains, in SUSY, both fermion and boson loops (Figure 1.1) which, according to Feynman rules, contribute with an opposite sign. The association of a scalar to each fermion automatically cancels the quadratic divergences and solves the fine-tuning problem, providing that the SUSY partners are not too heavy compared with the fermions of the SM, i.e.  $m_{SUSY} \lesssim 1 \text{ TeV}$ .

- **SUSY brings a candidate for Dark Matter:**

By construction, supersymmetric potential could contain some terms violating the baryon and lepton number conservation. Consequently, some models would predict the spontaneous decay of the proton through the exchange of  $\tilde{d}$ , which is ruled out by current data. To avoid such unwanted terms in the potential, one usually introduces a new symmetry called *R-parity* which is multiplicatively conserved and defined by:

$$R = (-1)^{3(B-L)+j}$$

where  $B$  is the baryon number,  $L$  the lepton number and  $j$  the spin. By definition,  $R = 1$  for all matter particles and  $R = -1$  for their super-partners. Some important phenomenological consequences of the *R-parity* conservation are that:

- supersymmetric particles can only be produced by pairs of sparticle–anti-sparticle,
- the decay products of all SUSY particles must contain an odd number of sparticles.

Consequently, the Lightest SUSY Particle (LSP) is heavy and naturally neutral and stable which makes it an excellent candidate for the dark matter[14].

- SUSY yields unification of the coupling constants:

With the SM, the inverse gauge couplings  $\alpha_1(Q^2) \sim g'^2$ ,  $\alpha_2(Q^2) \sim g^2$  and  $\alpha_3(Q^2) \sim g_S^2$  depend on the energy and run linearly with  $\ln(Q^2)$ . Although  $\alpha_1^{-1}$  decreases with  $Q^2$  while  $\alpha_2^{-1}$  and  $\alpha_3^{-1}$  increase, the extrapolation of their trend never meet to a single value (Figure 1.2, left). On the contrary, one expects a unification of these couplings

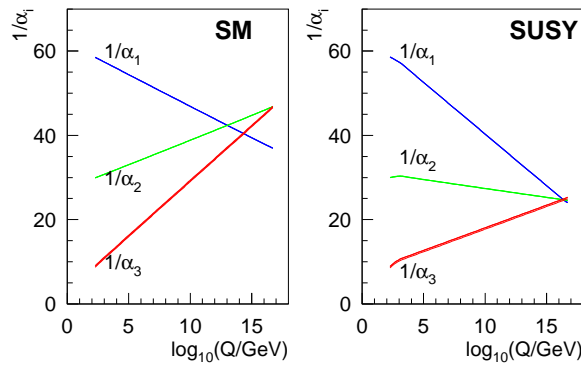


Figure 1.2: Evolution of the inverse of the gauge constants in the SM (left) and in the MSSM (right), for which the unification is obtained. The SUSY particles are assumed to contribute only above the effective SUSY scale of about 1 TeV, which cause the change in slope in the evolution.

at high energy, in the context of a  $SU(5)$  Grand Unification Theory. However, with the introduction of a new SUSY scale around 1 TeV, the unification of the constants can be reached at a scale of  $10^{16}$  GeV (Figure 1.2, right).

- SUSY predicts low-mass Higgs boson:

The lightest supersymmetry Higgs boson should not weight more than 140 GeV in most of the SUSY models [15]. This constraint is in agreement with the fit on the current electroweak precision observable, which tends to favor a light Higgs boson mass (Figure 1.3).

It has to be noticed that SUSY is not the only model solving the mass hierarchy problem, or predicting the existence of new particles not yet discovered. One can cite for example the theories of Extra Dimensions, Kaluza-Klein, Technicolor or the 4<sup>th</sup> generation to name the most famous ones.

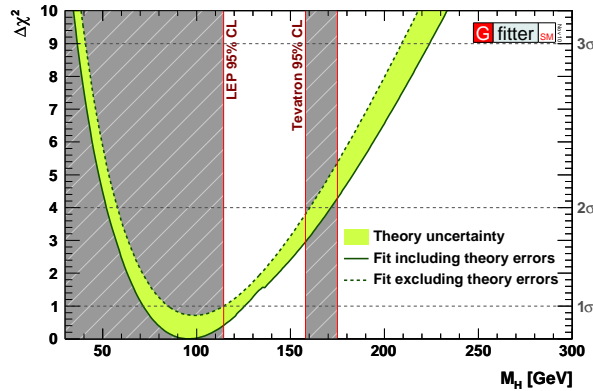


Figure 1.3:  $\Delta\chi^2$  curve derived from the all electroweak precision observable (but the Higgs boson mass) measured at LEP and TEVATRON, as a function of  $m_H$ , assuming the SM to be the correct theory [16].

### 1.3 Physics at the LHC

In order to understand the origin of the electroweak symmetry breaking for which the Higgs mechanism is supposed to be responsible for, and to probe new sectors on physics, the CERN accelerators facility center has made the choice to build a high-energy proton and ion collider in the former tunnel of the LEP close to Geneva.

Starting from hydrogen atoms on which electrons have been removed, protons are injected into a linear accelerator LINAC2 up to an energy of 50 MeV. The next steps of energy increase bring the protons to the BOOSTER (1.4 GeV), to the proton synchrotron PS (26 GeV) where protons bunches are formed, and then to the SPS (450 GeV), where there are then sufficiently energetic to be injected into the LHC ring, as represented in Figure 1.4. The operation is repeated 24 times, injecting half clockwise and half anti-clockwise. Final acceleration from 450 GeV to 7 TeV in the LHC is performed through a radio-frequency (RF) system consisting of 8 single super-conducting cavities per ring, providing an electrical field of 2MV/cavity at 400MHz.

Once in the LHC ring, specific optics composed of 1232 dipole magnets and 992 quadrupole magnets are used respectively to keep the beam on their paths and to keep it focused. Only at four points of the rings, the beams are crossed:

- ATLAS (P1) and CMS (P5) are two general-purpose experiments, mainly concentrated on search of Higgs boson and new physics,
- ALICE (P2) for the study of heavy-ion collisions,
- LHCb (P8) looking for the CP-violation in  $b$ -quark interactions.

Four other caverns are equipped with beam instrumentation as the RF system (P4), beam dump (P6) and collimators for the cleaning of the betatron (P3) and momentum (P7) of the beam.

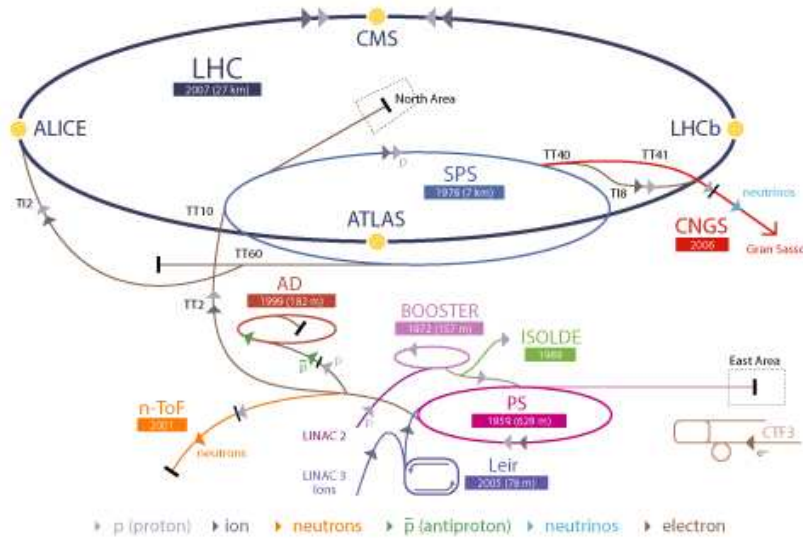


Figure 1.4: Representation of the CERN acceleration complex.

In 2010 run period, the accelerator machine ran with a energy per beam of 3.5 TeV rather than the nominal 7 TeV for security reasons related to inter-dipole electrical connections. Also, during few days in 2010, the LHC accelerated and collided heavy lead nuclei (hence the name *Hadron Collider*). In that case, the acceleration chain starts from the LINAC3, followed by the Low-Energy Ion Ring (LEIR) which store them before the injection to the PS. The primary goal of heavy-ion collisions is to study the formation and decay of quark-gluon plasma: a new state of the matter, like a dense 'soup' of quarks and gluons formed at high temperature.

The choice of a hadronic machine, despite the large success of the previous  $e^+e^-$  collisions at the LEP, has many advantages compared to a leptonic machine, in terms of discovery potential. Indeed, the nominal design of the LHC (3.5 TeV during phase I, 7 TeV for phase II) allows for parton interactions at the c.m.s. energy around 1 TeV, i.e. in high-energy region where new physics may appear, and provides large luminosities, i.e. high rate of collisions.

However, the design also brings a lot of non-convenient effects. Firstly, as the interactions happen between partons (quarks and gluons) which carry an unknown fraction of momentum and energy of the incoming protons, the initial conditions of the event remain unknown. Moreover, the parton density functions (PDF) of the proton have never been measured at these energies, and are just extrapolation of fit from previous experimental results. That leads to big uncertainties in the hard process cross-section predictions as it factorizes into a hard scatter part and a long range part:

$$\sigma_{pp \rightarrow X} = \sum_{j,k} \int_0^1 dx_1 g_j(x_1, \mu_F^2) \int_0^1 dx_2 g_k(x_2, \mu_F^2) d\hat{\sigma}_{jk \rightarrow X} \quad (1.1)$$

where  $g_a$  is the PDF which gives the probability for a parton  $a$  of the proton to enter the hard scatter with a fraction  $x$  of the original momentum.

Secondly, recorded events produced in hadron collisions have in general more complex and less clean final states than at the LEP: strong interactions result in higher track multiplicity due to gluon radiation, hadronisation of the proton remnant in the forward direction and the multiple parton interactions. Final states of interest are then embedded in a complicated jet-filled environment, as illustrated in Figure 1.5 showing an inclusive dimuon event.

Finally, in order to reach such luminosities, the LHC will have to proceed to simultaneous multiple collisions per bunch-crossing (the so-called *pileup events*, see Section 3.1) which will give rise to a large occupancy of the detectors.

On the contrary, high-energy photon interactions usually result in simple topology of the initial and final states, and clean experimental environment. Properties of such interactions have been studied in Section 2.1, while their experimental detection is covered in Chapter 5.

Although the rate of photon interactions (as well as associated cross-sections) is relatively small, studying processes mediated by photons at the LHC should bring complementary results to the nominal parton-parton interactions with interesting tests of the SM and searches for beyond SM.

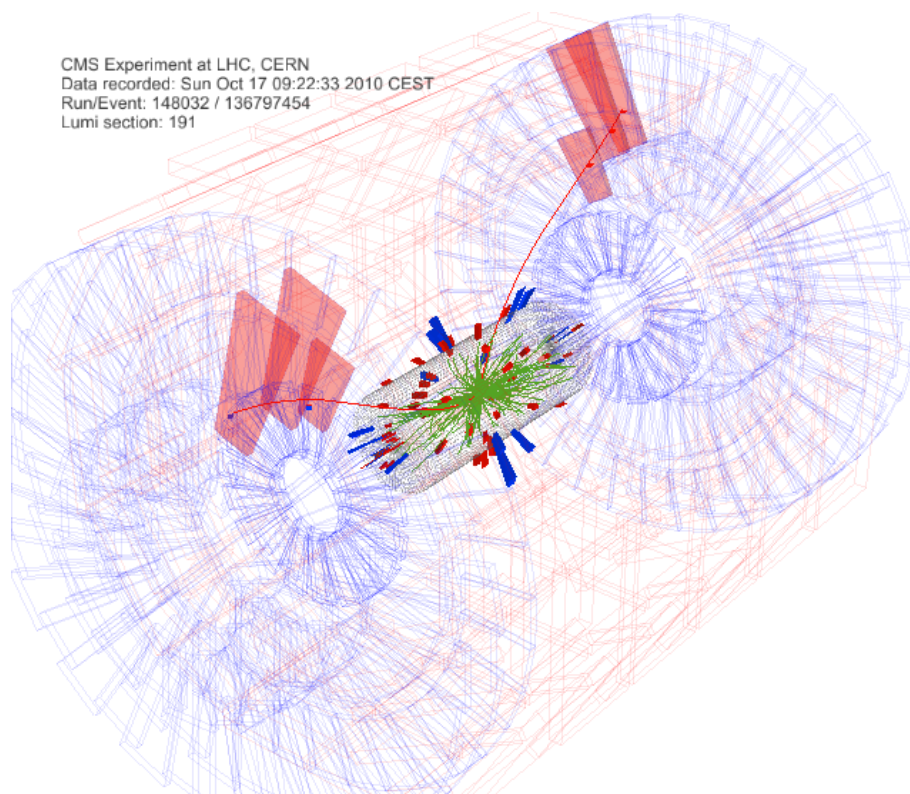


Figure 1.5: Event display of an inclusive dimuon events. The event contains 4 primary vertices, 172 tracks and 9 jets.





## Chapter 2

# Photon interactions at the LHC

*“And God said, ‘Let there be light’, and there was light. God saw that the light was good ”*

The Creation, Genesis

Photons interactions have been studied mainly at HERA to test the hadronic structure of the proton. However, similar phenomena have been seen at TEVATRON [19, 20] and at the LHC [7]. In this spirit, the LHC may be considered as a ‘parasitic’ photon collider, aiming to study photon-photon, photon-quark and photon-gluon interactions. This chapter, devoted to photon interaction properties, is divided in three sections. First, the phenomenology related to the different interaction types is explained in Section 2.1, followed by the introduction of a convenient mathematical framework design to describe these interactions at high energy: the Equivalent Photon Approximation in Section 2.2. An alternative method using the full Matrix Element computation is explained in Section 2.3. At the end of the chapter, a small section is devoted to the experimental properties of other exclusive processes.

### 2.1 Photon interactions at high energies

The  $\gamma$ -exchange in a collider experiment is characterized by striking experimental signatures. Indeed, as colorless object is emitted from the proton, large rapidity regions of the detector are devoted of any hadronic activity between the central state and the outgoing protons, and one usually refers to it as *rapidity gaps*. The experimental aspects related to the selection of exclusive events are established in Chapter 5.

Moreover in case of elastic photon exchange, the incoming proton survives, is scattered at almost zero-degree angle and escapes undetected along the beamline. Far from the interaction point (IP), some dedicated very forward stations may detect this proton, tag the photon-exchange and reconstruct their energies. Studies on the installation of such forward stations at 240 m and 420 m of the IP within the HPS project are discussed in Chapter 4.

### 2.1.1 Two-photon interaction

Photon-photon fusion is the class of interactions where photons are emitted from both sides. As shown in Figure 2.1, each of the two incoming protons emits a virtual photon. These photons fuse to give a system  $X$  of particles which is centrally produced. The proton either survives and is scattered at small angle in case of elastic emission, either dissociates to a hadronic state in case of inelastic emission (Figure 2.4).

Among the photon-interactions processes, it is without doubt the most promising class of events, in particular because the same physics as in  $e^+e^-$  collisions at the LEP can be studied, but this time probed with energies above the electroweak scale. Moreover,

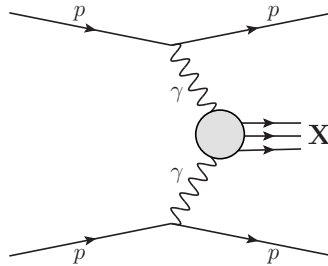


Figure 2.1: Feynman diagram for the exclusive two-photon elastic production  $pp(\gamma\gamma) \rightarrow pXp$

as there is any color flow on any sides of the interaction, two-photon induced processes lead to the cleanest final states ever: only the result of the photons fusion  $X$  is produced out of the collision, in association with the two centrally-undetected scattered protons.

The most interesting processes to be studied are the pair productions of non-strongly interacting particles, as the diffractive background contamination is small and the background from purely-hadronic interactions is easily suppressed based on low-multiplicity of tracks and/or rapidity gap requirement. In addition, if the entire event is reconstructed, transverse momentum will also provide large rejection power.

Some examples of reachable final states in  $\gamma\gamma$  fusion and their physics potential are:

- the direct pair production of 'new-physics' massive particles, as  $4^{th}$  generation, SUSY [8, 21, 22], Extra-Dimension [23, 24]. An exploratory study of two-photon production of supersymmetric pairs is presented in Chapter 8,
- search for Dirac monopole [25],
- exclusive SM Higgs production, in case of high  $H\gamma\gamma$  coupling, or charged Higgses [26],
- search for new massive gauge bosons with the anomalous (triple, quartic) gauge couplings [27, 28, 29],
- search for unparticle physics interaction with SM [30],
- pair production of leptons for luminosity normalization at the LHC [31, 32], with first measurements at CMS discussed in Chapter 7,
- pair production of leptons for HPS tracking stations alignment [3].

### 2.1.2 Photo-production

Photo-production refers to the class of processes where the photon interacts with a gluon or a quark (referred as the parton  $\hat{p}$ ) from the other proton, as represented in Figure 2.2. It results in final states less clean than the photon-photon processes as one side of the hemisphere involve a proton breaking, but one expects larger cross-sections and larger c.m.s. energies. As cross-section calculations are partially based on PDF, predictions are in general more uncertain. Physics potential of photo-production includes [1, 33, 34]:

- measurements of the top quark mass and charge,
- constraint of the  $V_{tb}$  CKM matrix element with associate  $Wt$  production,
- observation of the SM Higgs, with associate  $WH$  in case of fermiophobic Higgs
- search for FCNC with the anomalous production of single-top

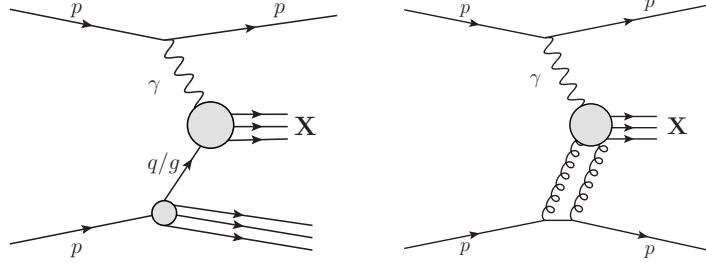


Figure 2.2: Left: Feynman diagram for the photo-production  $pp(\gamma\hat{p}) \rightarrow pXN'$ . Right: Feynman diagram for the diffractive photo-production  $pp(\gamma\mathbb{P}) \rightarrow pXp$ .

### 2.1.3 Diffractive photo-production

Diffractive photo-production is a sub-class of  $\gamma p$  interactions where the photon interacts with a QCD color-singlet state. The process can be factorized in three steps<sup>1</sup> as shown of Figure 2.2, right : (a) the photon fluctuates into a  $q\bar{q}$  pair; (b) the pair interacts, at leading order in perturbative QCD, with a two-gluon state – called pomeron<sup>2</sup> ( $\mathbb{P}$ ) – emitted from the proton which remains intact; (c) final state is formed from the pair. Only states with the same quantum numbers than the photon can be produced:  $\rho$ ,  $\omega$ ,  $\phi$ ,  $\psi$ ,  $J/\psi$ ,  $\Upsilon$  and  $Z$  boson. Unfortunately, the relative low-mass quarkonium resonances like  $J/\Psi$  are decaying, when they are produced at low- $p_T$  as in diffractive photo-production, to final states which are at the limit of the detection criteria for the current LHC experiments (small  $p_T$ , large  $\eta$ ), except if special triggers are dedicated to these signals.

Since the photon emission is relatively well known, these kind of interactions may be interesting to probe the pomeron flux from the other proton, and test the QCD saturation effects resulting from non-linear gluon dynamics [35, 36]. Indeed, the cross-section is proportional to the square of the gluon density in the proton, which is suppose to be higher at low- $x$ . As a consequence, production rates are predicted to rise as a function of  $W$ , the photon-proton c.m.s. energy, and is expressed as  $\sigma \sim W^\delta$ . Various measurements at HERA as well as fit to extract the  $\delta$  values are summarized in Figure 2.3 [37]. The detection of exclusive  $\Upsilon$  (Section 6.5) and  $J/\Psi$  (Section 6.6) at the LHC will therefore extend the cross-section measurements at higher energies that

<sup>1</sup>This picture is however only valid in the reference frame of the proton which have emitted the photon, i.e. in a reference frame where the photon moves very fast.

<sup>2</sup>The state is called pomeron in honor of the Russian physicist Pomeranchuk who studied the behavior of vacuum state exchange and postulated the existence of a new reggeon.

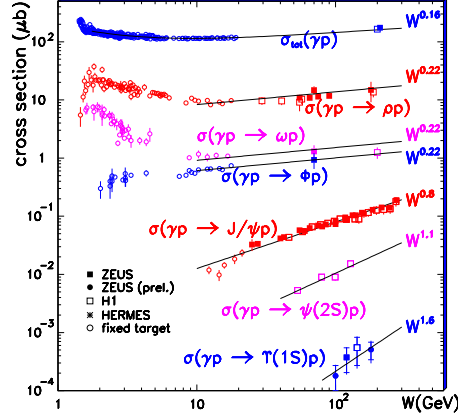


Figure 2.3: Diffractive vector meson photo-production measurements at HERA. The  $W_{\gamma p}$  dependence of the cross-section is parameterized as  $W^\delta$ , with  $\delta$  extracted from fit [37].

what was probed in  $ep$  collisions.

All the physics information is contained in the  $t$  variable which is the four-momentum squared of the proton which does not emit the photon and is sensitive to correlations between gluon pairs within the proton. This is related to previous quantities as  $\delta = 4(\alpha(t) - 1)$  with  $\alpha$  the exchanged pomeron trajectory. Although  $t$  quantity cannot be probed directly in  $\gamma\mathbb{P}$  interactions at the LHC, a good approximation is the  $p_T^2$  of the reconstructed vector meson.

## 2.2 The Equivalent Photon Approximation

Based on an original idea of Fermi [38] who pointed out that the field of a fast charged particle is similar to an electromagnetic radiation which can be interpreted as a flux of photons, Weizsäcker [39] and Williams [40] independently proposed the introduction of an equivalent real photon spectrum to compute the cross-sections for the interaction of particles in relativistic motion.

In their article of 1975 untitled '*The two-photon particle production mechanism*', Budnev and collaborators proposed an extension of the Weizsäcker-Williams method including the treatment of photon virtualities [41]. The so-called Equivalent Photon Approximation (EPA) is an approximative method to compute cross-section of

electromagnetic processes by considering them as interactions of fluxes of equivalent photons. In the EPA, the scattering amplitude factorizes as to separate the photon exchanges (process-independent) from the photons interaction (process-dependent) with the introduction of the equivalent photon spectrum  $dN_\gamma$ :

$$d\sigma_{pp(\gamma\gamma)\rightarrow pXp} = \sigma_{\gamma\gamma\rightarrow X} \otimes dN_{\gamma_1} \otimes dN_{\gamma_2} \quad (2.1)$$

This approximation consists to consider the photon as real and without polarization, which is valid only in case of low-virtuality photon exchange. As a consequence, the EPA can only be applied in situations where the cross-section is not sensitive to the virtuality of the photon, i.e. not for too low mass system  $X$ . Moreover, this corresponds only to the region of small proton scattering angles. One example of the "inapplicability" of the method is for the cross-section of the two-photon production of lepton pairs  $pp(\gamma\gamma) \rightarrow p\ell^+\ell^-p$ . One has then to use the exact matrix element solution computed with dedicated numerical methods as explained in Section 2.3.

After defining the following quantities related to the kinematics of the photon-induced process:

- $p^\mu$  the colliding proton momenta,
- $p'^\mu$  the scattered proton momenta,
- $q^\mu = p^\mu - p'^\mu$  the virtual photon momenta,
- $Q^2 = -(p^\mu - p'^\mu)(p_\mu - p'_\mu)$  the momentum transfer,
- $x = E_\gamma/E_p$  the photon/proton energy fraction,

one can write the spectrum  $dN_\gamma$  [41, 42, 43]:

$$dN = \frac{\alpha}{\pi} \frac{dQ^2}{Q^2} \frac{dx}{x} \left[ (1-x) \left( 1 - \frac{Q_{min}^2}{Q^2} F_E(Q^2) \right) + \frac{x^2}{2} F_M(Q^2) \right] \quad (2.2)$$

where  $F_E$  and  $F_M$  functions are the electric and magnetic form factors of the incoming particles.

The number of equivalent photons (or the photon spectrum) is calculated by integration over the whole virtuality range:

$$f_\gamma(x) = \frac{dN}{dx}(x) = \int_{Q_{min}^2}^{Q_{max}^2} \frac{d^2N}{dQ^2 dx}(x, Q^2) dQ^2 \quad (2.3)$$

and is shown at Figure 2.5 for elastic and inelastic contributions.

### Elastic photon exchange flux

In the literature, a photon exchange for which the proton remains intact is called *elastic* production. In that case, in the equation of the spectrum (2.2), the  $F_E$  and  $F_M$  functions take the values:

$$\begin{aligned} F_E(Q^2) &= \frac{4m_p^2 G_E^2 + Q^2 G_M^2}{4m_p^2 + Q^2} \\ F_M(Q^2) &= G_M^2 \end{aligned} \quad (2.4)$$

using the convenient dipole approximation for the proton form factor

$$\begin{aligned} G_E(Q^2) &= \left(1 + \frac{Q^2}{Q_0^2}\right)^{-2} \\ G_M(Q^2) &= \mu_p \left(1 + \frac{Q^2}{Q_0^2}\right)^{-2} \end{aligned} \quad (2.5)$$

with  $\mu_p = G_M(0) = 2.79$  and  $Q_0^2 = 0.71 \text{ GeV}^2$  the dipole form factor [41].

The flux  $dN/dx$  is found using (2.3) with:

$$Q_{min}^2 \simeq m_p^2 \frac{x^2}{1-x}; \quad Q_{max}^2 = 2 \text{ GeV}^2 \quad (2.6)$$

The upper term is motivated by strong  $\gamma$ -exchange suppression due to the presence of electromagnetic form factor and to the finite spatial charge distribution of the proton [41], while the minimal value is a kinematical limit. The full computation [41] is shown in Figure 2.5. One can notice that the spectrum is strongly peaked for low- $x$  values which means that the flux will be mostly composed of low-energetic equivalent photons. As the flux drops with virtuality as  $\sim 1/Q^2$ , for low- $x$  the virtualities are in general small,  $\langle Q^2 \rangle \simeq 0.01 \text{ GeV}^2$ . As a consequence, the low-virtuality approximation made in EPA is valid in most of the cases. From the kinematic point of view, that implies very small proton scattering angles,  $\sim 20 \mu\text{rad}$  [42].

## Inelastic photon exchange flux

Within some conditions, the proton dissociates due to the photon exchange into a hadronic system  $N$  with low-mass  $m_N$ :

$$m_N = p'^{\mu} p'_{\mu} \quad (2.7)$$

as schematically represented in Figure 2.4. In the literature, these kind of processes are called *inelastic* productions. We usually call semi-elastic production, the two-photon interaction where one of the proton survives and the other one breaks. Similarly, fully-inelastic production refers to processes where both protons dissociate. The  $F_E$

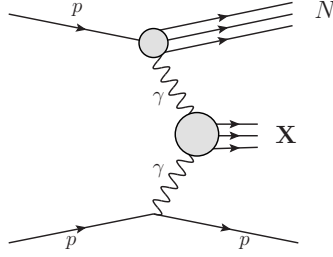


Figure 2.4: Feynman diagram for inelastic production  $pp(\gamma\gamma) \rightarrow pXN$

and  $F_M$  functions are integrated functions of the proton structure function  $F_2(x_b, Q^2)$  [42]:

$$\begin{aligned} F_E(Q^2) &= \int \frac{F_2(x_b, Q^2)}{x_b} dx_b \\ F_M(Q^2) &= \int \frac{F_2(x_b, Q^2)}{x_b^3} dx_b \end{aligned} \quad (2.8)$$

with the Björger  $x_b \simeq Q^2/(m_N^2 + Q^2)$ . This is equivalent to perform integral over the photon virtualities and over  $m_N$  from  $m_p$  to  $m_N^{max}$  which is taken as 20 GeV in the next computations. The  $F_2$  values can be extracted experimentally from the cross-section measurement of  $\gamma^*p$  interactions [44].

The flux  $dN/dx$  is found using (2.3) with:

$$Q_{min}^2 \simeq m_N^2 \frac{x}{1-x}; \quad Q_{max}^2 = 300 \text{ GeV}^2 \quad (2.9)$$

and is shown at Figure 2.5.

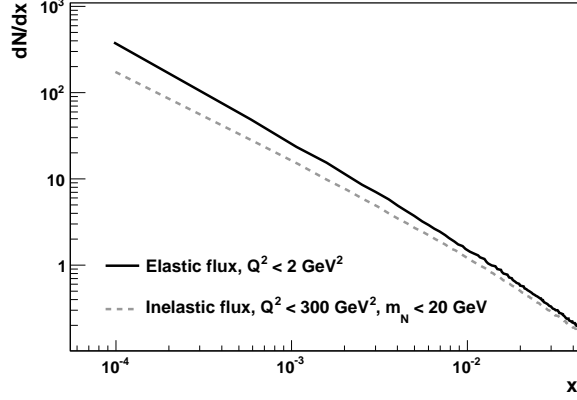


Figure 2.5: Number of equivalent photons in case of elastic (plain) and inelastic (dash) photon exchange, as a function of  $x = E_\gamma/E_p$ . Horizontal and vertical axis are log-scaled.

### Photon luminosity

In the EPA, electromagnetic interactions between charged hadrons are seen as interactions of photons. From this point of view, the LHC can thus be considered as a photon collider and the relative photon luminosity, i.e. the fraction of the luminosity which involves photon interactions to the nominal luminosity, can be computed within the same framework using the  $Q^2$ -integrated luminosity spectrum  $f_\gamma$  (2.3).

In case of two-photon interaction, the luminosity spectrum  $L_{\gamma\gamma}$  includes the integrated flux of each photon and is defined as:

$$\frac{dL_{\gamma\gamma}}{dW_{\gamma\gamma}} = \int_{W_{\gamma\gamma}^2/s}^1 2 W_{\gamma\gamma} f_\gamma(x) f_\gamma\left(\frac{W_{\gamma\gamma}^2}{xs}\right) \frac{dx}{xs} \quad (2.10)$$

with

$$W_{\gamma\gamma} = 2 \sqrt{E_{\gamma_1} E_{\gamma_2}} \quad \text{the photon-photon c.m.s. energy} \quad (2.11)$$

$$s = 4E^2 \quad \text{the proton-proton c.m.s. energy} \quad (2.12)$$

The relative luminosity spectrum  $\frac{dL_{\gamma\gamma}}{dW_{\gamma\gamma}}$  is shown at Figure 2.6 for elastic-elastic, elastic-inelastic and inelastic-inelastic processes. Two incoming proton energies are taken into consideration: 3.5 TeV and 7 TeV. Again, one should note that since the spectrum  $dN_\gamma$  is peaked for low-energy photons, the average  $\gamma\gamma$  c.m.s. energies are

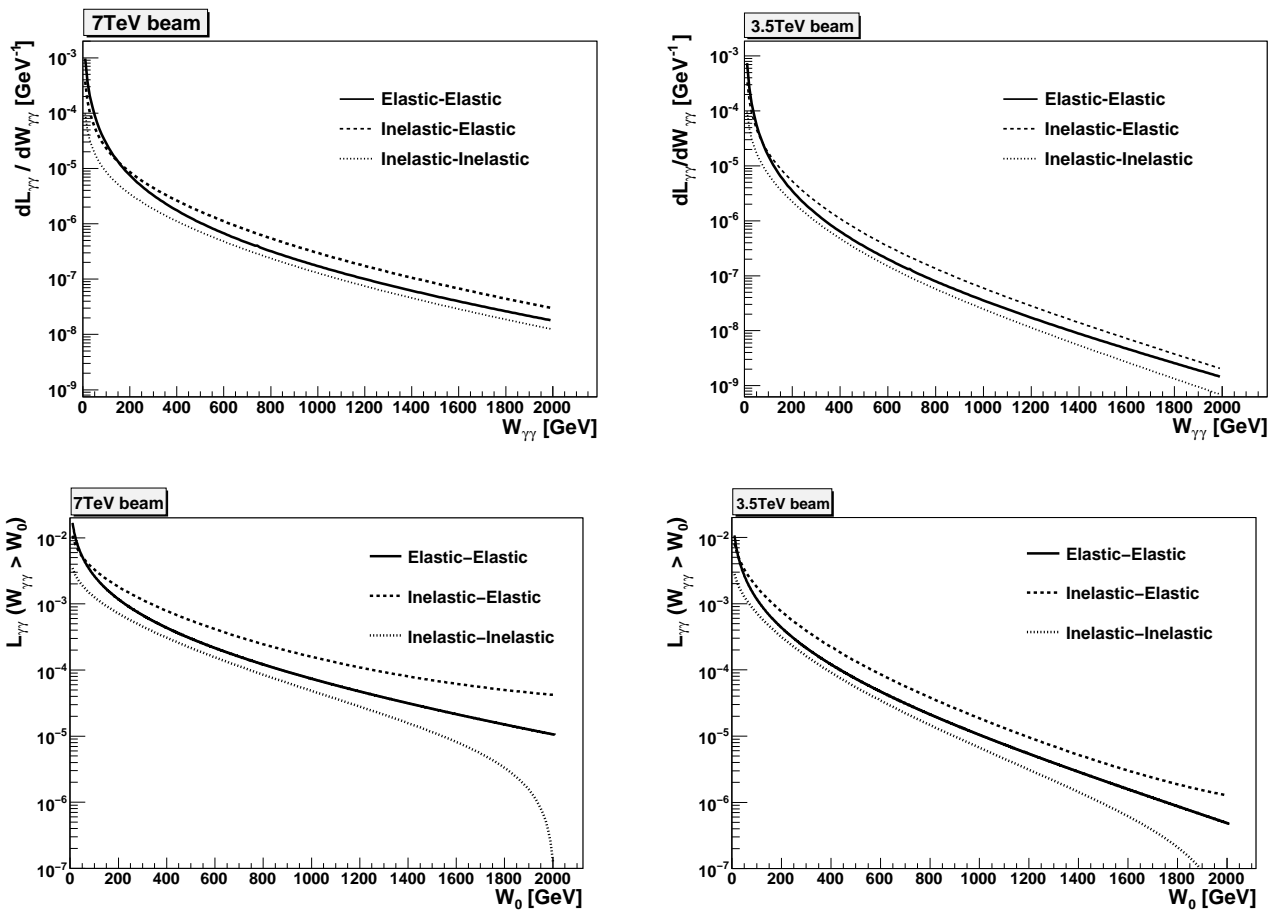


Figure 2.6: Left: Relative photon-photon luminosity  $\frac{dL_{\gamma\gamma}}{dW_{\gamma\gamma}}$  as a function of the two-photon c.m.s. energy  $W_{\gamma\gamma}$ . Right: Integrated photon-photon luminosity  $\int_{W_0}^{\infty} \frac{dL_{\gamma\gamma}}{dW_{\gamma\gamma}} dW_{\gamma\gamma}$  as the function of the minimal two-photon c.m.s. energy  $W_0$ . For elastic flux, the maximal transfer momentum is  $Q^2 < 2 \text{ GeV}^2$ , while for inelastic flux  $Q^2 < 300 \text{ GeV}^2$  and  $m_N < 20 \text{ GeV}$ .

relatively small compared to what is accessible in nominal parton-parton interactions, but extend to 1 TeV and even beyond.

The two-photon luminosity is then found by integrating the equation (2.10) over the  $\gamma\gamma$  c.m.s. energy. The spectrum is also shown in Figure 2.6 as a function of the minimum  $\gamma\gamma$  energy  $W_0$  to compute the integral, *i.e.*  $\int_{W_0}^{\infty} \frac{dL_{\gamma\gamma}}{dW_{\gamma\gamma}} dW_{\gamma\gamma}$ .

One finds that, for  $W_0 = 10$  GeV, the elastic-elastic integrated luminosity reaches 1.67% (1.08%) for  $\sqrt{s} = 14$  TeV (7 TeV), and the total available luminosity including inelastic photon-exchanges is 3.1% (2.2%). Although the relative luminosity is strongly peaked for low- $W_{\gamma\gamma}$  values, the fraction of the total  $pp$  luminosity available for elastic two-photon interactions is still 0.1% for  $W_0 = 226$  GeV (114 GeV). Taking into account the nominal LHC luminosity of  $10^{34} \text{ cm}^{-2} \text{ s}^{-1}$ , this leads to large production rate despite the relative low cross-sections.

## Cross-sections

For cases where the EPA is satisfied, the proton-proton cross-section can be written as the convolution of the probability of the proton to emit a photon with the photon-photon(parton) cross-section:

$$\begin{aligned} d\sigma_{pp(\gamma\gamma)\rightarrow pXp} &= \sigma_{\gamma\gamma\rightarrow X}(W_{\gamma\gamma}) dN(x_1, Q_1^2) dN(x_2, Q_2^2) \\ d\sigma_{pp(\gamma\hat{p})\rightarrow pXN'} &= \sigma_{\gamma\hat{p}\rightarrow X}(W_{\gamma p}) dN(x, Q^2) \end{aligned} \quad (2.13)$$

Using the equivalent luminosity spectrum defined in (2.10), it turns to:

$$\begin{aligned} \sigma_{pp(\gamma\gamma)\rightarrow pXp}(s) &= \int_{W_0}^{\sqrt{s}} \frac{dL_{\gamma\gamma}}{dW_{\gamma\gamma}}(W_{\gamma\gamma}, s) \sigma_{\gamma\gamma\rightarrow X}(W_{\gamma\gamma}) dW_{\gamma\gamma} \\ \sigma_{pp(\gamma\hat{p})\rightarrow pXN'}(s) &= \int_{x_{min}}^1 f_{\gamma}(x) \sigma_{\gamma p\rightarrow X}(x, s) dx \end{aligned} \quad (2.14)$$

It depends only on the energy of the incoming proton (which modify the flux), the charge of the produced particles, the mass and the spin, as shown in Figure 2.7 on which is displayed the elastic-elastic cross-section for different mass and spin state pairs. As any parton density function of the proton has to be accounted, it makes the two-photon interactions extremely well-known processes. Taking into account inelastic photon-fluxes, for which uncertainties remain large and without possibility of forward double-tag, the total cross-section is roughly a factor 3.5 higher than the elastic-elastic value.

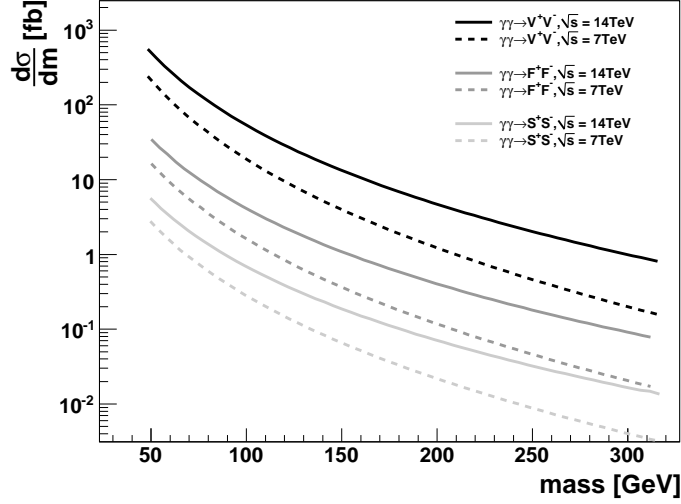


Figure 2.7: Proton-proton doubly-elastic cross-section for the two-photon production of scalar (spin 0), fermion (spin 1/2) and vector (spin 1) pairs as a function of the particle mass, using the EPA coded into CalcHEP.

### Survival probability

On top of the Equivalent Photon Approximation, we have to take account of the hadronic structure of the proton and add the rescattering effect, i.e. secondary strong interactions between spectator partons. This rescattering, because it happens simultaneously to the photons fusion, has an impact on the experimental signatures with gap requirement. Indeed, color exchange will force the proton to hadronize and then produce multiple secondary soft particles which will fill the rapidity gap, similarly to what happens in an inelastic photon exchange. For instance, at the TEVATRON, the rate of exclusive dijet events was measured to be lower by a factor 10% compared to the predicted value [45].

In order to take this effect into account, the *survival probability*  $S^2$  has been introduced in the literature as a correction factor to the theoretical cross-section. The factor  $S^2$  has not a unique value but depends on the kinematical configurations of the incoming hadron, the final states interactions and the impact parameter as

$$S^2 \sim d \sim \frac{1}{\sqrt{Q^2}}$$

which means that for low impact parameter  $d$ , the interactions stands inside the strong interaction radius and the protons can "feel" each other, leading to a small value of the survival probability. As the average  $Q^2$  increase with the energy, we expect lower survival for higher c.m.s. energies.

Two-photon interactions, since they are characterized by large impact parameters, are in general not much affected by the rescattering and the survival probability is around one. On the contrary, for interactions between photon and quark or photon and gluon, the probability that the survival proton interacts strongly with the other one is higher. In general, one also has  $S^2(\gamma\gamma) > S^2(\gamma\mathbb{P}) > S^2(\mathbb{P}\mathbb{P})$ . Various theoretical predictions exist in the literature, with different models, inputs or methods of computation. Without being exhaustive, here are a few examples of computations for different exclusive processes:

- The rescattering correction for the two-photon production of muon pairs was calculated in [31] for muon pairs produced at  $\sqrt{s} = 14$  TeV, with an invariant mass  $m_{\mu\mu} = 20$  GeV and at zero-rapidity. The correction is function of the  $p_T$  of the pair and gives  $1 - S^2 < 10^{-4}$  for  $p_T = 10$  MeV and  $1 - S^2 < 6 \times 10^{-4}$  for  $p_T = 30$  MeV.
- Similar calculations for the  $\gamma\gamma \rightarrow H$  process predicts  $S^2 = 90\%$  for a Higgs mass of 120 GeV at  $\sqrt{s} = 14$  TeV in [46].
- In the  $W$  production via photon-exchange  $\gamma p \rightarrow W + X$ , the rescattering suppresses the cross section by a factor of about 4 for  $|t| \simeq 0.1$  GeV<sup>2</sup> [47].
- Finally, the Higgs production through central exclusive process (see Section 2.4) is even more subject to rescattering effect. Using two possible values of the proton  $b$ -slope, one gets a survival factor in the range 2.4%–4.5% for a Higgs mass of 120 GeV [48, 49].

Rescattering can also appear in inelastic cases, but has a different meaning. The proton has already dissociated, so the secondary interactions happen between secondary particles of the proton remnant. These kind of interactions are not well known and thus contribute a lot to the uncertainties for the inelastic processes cross-sections.

## 2.3 The LPAIR generator

As already quoted, the EPA can only be used under some specific conditions, including the fact that the cross-section is insensitive to the photon virtualities. Therefore, this approximation is not valid for two-photon production of low-mass  $X$  system, for instance the  $\gamma\gamma \rightarrow \ell^+\ell^-$  process. In that case, the only alternative to compute cross-sections and kinematics is to use the full matrix element (ME) computation. The LPAIR generator [50] is a stable computer program devoted to the simulation of electro-magnetic production of lepton pairs in lepton-lepton, lepton-hadron or hadron-hadron interactions through two-photon interactions.

The Monte-Carlo event generation is based on a stable formula [51] adapted to take into account the specificities of the two-photon interactions. On the one hand, as there are two photons in the  $t$ -channel, most of the cross-section is found to come from the very small  $|t|$  values of the protons, i.e.  $\sigma \sim t_1^{-1}t_2^{-1}$ . Severe problems appear then when one tries to integrate it numerically (especially an integration over an experimental acceptance only), except if the integral over the phase-space is reformulated. On the other hand, the evaluation of the ME itself for such processes in a standard "Feynman rules" fashion would lead to bad cancellations between various terms.

The philosophy of LPAIR is therefore to consider kinematically the two-photon interactions as a  $2 \rightarrow 3$  process like in Figure 2.8. All the  $\gamma\gamma$  physics kinematical prop-

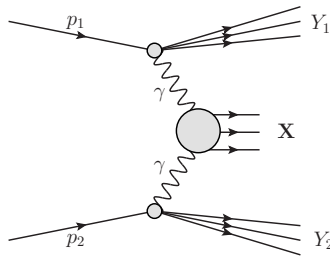


Figure 2.8: Kinematics of the  $\gamma\gamma$  process as it is considered in the LPAIR program.

erties can be found in this system, independently of the particle content of the three final systems  $Y_1$ ,  $Y_2$  and  $X$ . Once the amplitude for the sub-reaction  $\gamma\gamma \rightarrow \mu^+\mu^-$  has been written in a gauge-invariant way and the ME evaluated for this sub-reaction, the result is multiplied by a structure function of the proton available. For the elastic signal, in which protons behave like point-like particles, one needs to multiply by

the electromagnetic dipole form factor [52], to take into account the finite size of the proton.

In order to simulate the fragmentation step in case of inelastic photon exchange, the Lund shower Monte-Carlo [53] implemented in the JetSet software [54] is used, with two different structure functions on choice. For  $m_N < 2 \text{ GeV}$  and  $Q^2 < 5 \text{ GeV}^2$ , the Brasse 'cluster' fragmentation is chosen [55] while for the other cases the Suri-Yenni 'string' fragmentation is applied [56]. In the first case, the low-mass system  $N$  mostly decays to a  $\Delta^+$  or  $\Delta^{++}$  resonance, which results in a low multiplicity states. On the contrary, in the second one, the high-mass system usually decays to a variety of resonances ( $\Delta$ ,  $\rho$ ,  $\omega$ ,  $\eta$ ,  $K$ ) which produce a large number of forward protons, pions, neutrons and photons. The pseudo-rapidity<sup>3</sup> spectrum of the beam remnant particles is shown in Figure 2.9.

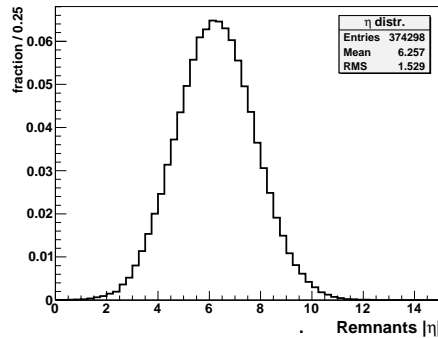


Figure 2.9: Pseudo-rapidity ( $\eta$ ) distribution particles produced in the proton fragmentation after inelastic photon emission. The events are simulated with LPAIR interfaced with JetSet and  $E_p = 3.5 \text{ TeV}$ ,  $1.07 < m_N < 320 \text{ GeV}$ .

The kinematical distribution of the particles in the proton remnant –and hence its visibility by central detectors– as function of the generated mass  $m_N$  of the proton remnant has been checked in Figure 2.10 using LPAIR + JetSet. The left side shows the most central particle pseudo-rapidity ( $\eta_{min}$ ) chosen among all particles simulated in the remnant, while the right side is for all particles with  $E > 5 \text{ GeV}$ .

One can notice that for the large majority ( $z$  axis is log scaled) of the events generated, the remnant mass is smaller than  $25 \text{ GeV}$  and is usually not visible by CMS central

<sup>3</sup>pseudo-rapidity is defined in (3.4).

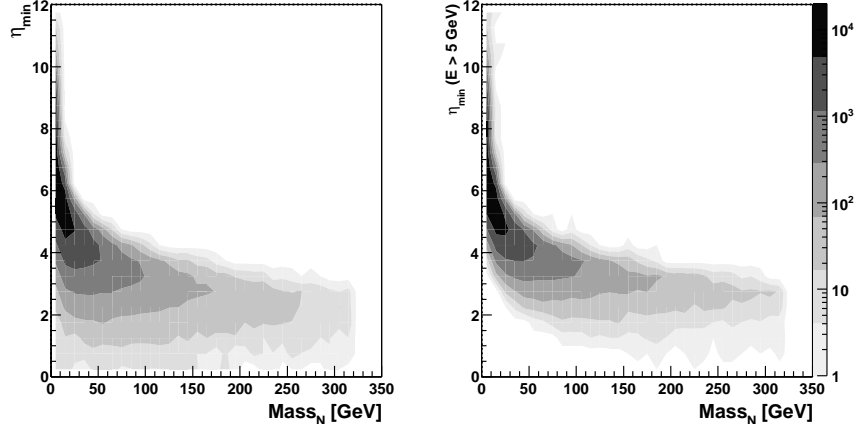


Figure 2.10: Contour plots of the most central particle pseudo-rapidity as function of the proton fragmentation mass  $m_N$ . The events are simulated with LPAIR interfaced with JetSet and  $E_p = 3.5$  TeV,  $1.07 < m_N < 320$  GeV.

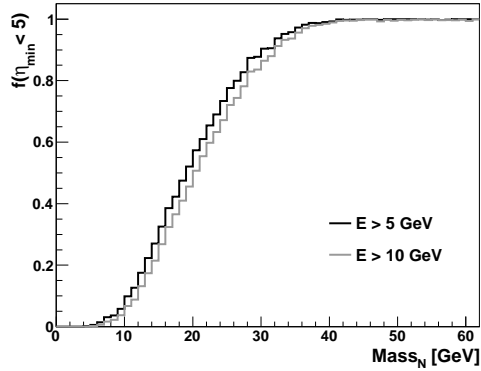


Figure 2.11: Fraction of events for which the most central particle of the remnant  $\eta_{min}$ , computed with 2 different energy thresholds, falls into the central CMS acceptance. The events are simulated with LPAIR interfaced with JetSet and  $E_p = 3.5$  TeV,  $1.07 < m_N < 320$  GeV.

detectors as  $\eta_{min} > 5$  on average. For large  $m_N$ , the number of produced forward objects increases and thus the probability to have part of the remnant produced within the acceptance of CMS. This detection efficiency of CMS to the proton remnant from inelastic photon exchange is demonstrated in Figure 2.11 which shows the fraction of events for which the most central particle with energy larger than 5 GeV (10 GeV) is in the acceptance of central detectors  $|\eta| < 5$ . One can notice a turn-on curve of the

probability between  $m_N \simeq 5 \text{ GeV}$  ( $f = 0\%$ ) and  $m_N \simeq 40 \text{ GeV}$  ( $f = 100\%$ ). That result is hence directly usable to justify the  $m_N < 20 \text{ GeV}$  cut that was set earlier to compute the inelastic photon flux as it turned out to be very rare that such high masses are produced. In addition, in such cases, most of events would be accompanied by visible remnant.

## 2.4 Central exclusive production as a background

As already introduced before, photon interactions at hadron collider lead to unusual, striking experimental signature: a central system  $X$ , forward region devoted of any activity and presence of undetected scattered protons. However, background processes resulting in the same topological final states have to be considered.

Indeed, exclusive states may also occur from central exclusive production (CEP) in which one gluon from each proton fuse to produce the central system  $X$ . In addition, a second color-screening gluon is passed between the interacting protons which allows them to remain intact, as seen for instance in Figure 2.12. The major experimental difference with respect to two-photon processes is the transverse momentum of the scattered proton which is, on average, larger in diffractive processes than in  $\gamma$ -induced ones.

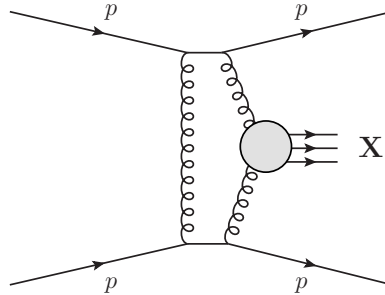


Figure 2.12: Feynman diagram for the exclusive central production  $pp(\text{CEP}) \rightarrow pXp$ .



## **Part II**

# **The experimental tools: CMS and HPS**



## Chapter 3

# The Compact Muon Solenoid experiment at the LHC

*“There are three principal means of acquiring knowledge... observation of nature, reflection, and experimentation. Observation collects facts; reflection combines them; experimentation verifies the result of that combination.”*

Denis Diderot (1713 - 1784)

The CMS experiment is a general multi-purpose detector, with a structure in layers designed to enclose at maximum the collisions happening at the center of the detector. Following the general layout of a modern collider-physics experiment, the CMS detector consists of a series of sub-detectors with specific aims: a tracker to reconstruct the kinematics of charged particles, an electromagnetic and hadronic calorimeters to measure the energy of  $\gamma$ ,  $e^\pm$  and hadrons, plus some additional muon chambers for the measurements of  $\mu^\pm$ . All sub-detectors are immersed in a high magnetic field to ensure precise momenta measurements.

The chapter is divided in 6 main sections: an introduction to the LHC accelerator characteristics for physics (3.1), an overview of the CMS detector and its purpose (3.2), a detailed description of the central (3.3) and forward (3.4) sub-detectors, the principles of event reconstruction (3.5) and a highlight on the relevant trigger properties for the following analyzes (3.6).

### 3.1 The Large Hadron Collider

The number of interactions per collision occurring at the interaction point of CMS (IP5) is function of the LHC beam configuration only and follows a Poisson distribution with a central value of

$$\mu = \sigma_{inel} \times \frac{\mathcal{L}}{n_b f_{rev}} \quad (3.1)$$

where:

- $\sigma_{inel}$  is the total inelastic cross-section,
- $n_b$  is the number of colliding bunch pairs in the LHC ring,
- $f_{rev}$  is the revolution frequency,  $f_{rev} = f/3564$ ,
- $f$  is the collision frequency, i.e. 40 MHz,
- $\mathcal{L}$  is the instantaneous luminosity which is given by:

$$\mathcal{L} = \frac{\gamma n_b f_{rev} N_p^2}{4\pi \epsilon \beta^*} S \quad (3.2)$$

with  $N_p$  the population of protons per bunch,  $\epsilon$  the transverse beam emittance,  $\beta^*$  the betatron function at the IP<sup>1</sup>. The geometric luminosity reduction factor  $S$  depends on the bunch length ( $\sigma_z$ ), the transverse beam size ( $\sigma_x = \sigma_y$ ) and the crossing angle ( $\alpha$ ) via:

$$S^{-1} = \sqrt{1 + \left(\frac{\sigma_z}{\sigma_x}\right)^2 \operatorname{tg}^2\left(\frac{\alpha}{2}\right)} \quad (3.3)$$

The design luminosity value will reach  $10^{34} \text{ cm}^{-2}\text{s}^{-1}$ , which leads to almost 1 billion proton-proton collisions per second.

The factor  $n_b/3564$  derives from the fact that only  $n_b$  of the 3564 bunches in the train will be filled with protons while injecting in the LHC. This beam structure is determined by the injection scheme and the beam dump kicker rise time of the PS, SPS and LHC and allow for maximum  $n_b = 2808$ .

The main bunch configurations, in addition to the luminosity recorded by CMS during these fills are displayed at Table 3.1 and plotted in Figure 3.1.

<sup>1</sup>These quantities are related to physical ones with  $\sigma_x \sigma_y = \epsilon \beta^*$

Start	Duration	$n_b$	$N_p(\times 10^{11})$	$1/f$	$\frac{\alpha}{2}[\mu rad]$	$L[nb^{-1}]$
25 May	10h	8	3	single	0	5
02 Jul.	37h	4	6 → 8	single	0	46
15 Jul.	38h	8	11 → 12	single	100	114
06 Aug.	93h	16	21 → 24	multi	100	626
19 Aug.	17h	16	42	multi	100	227
22 Aug.	16h	36	45	1250 <i>ns</i>	100	362
24 Aug.	14h	35	44	1000 <i>ns</i>	100	328
28 Aug.	14h	1	51	single	100	313
29 Aug.	11h	35	53	1000 <i>ns</i>	100	304
22 Sep.	14h	1	25 → 30	single	100	143
23 Sep.	16h	47	57 → 60	150 <i>ns</i>	100	743
25 Sep.	38h	93	100 → 114	150 <i>ns</i>	100	1964
30 Sep.	25h	140	156 → 181	150 <i>ns</i>	100	2081
04 Oct.	20h	186	194 → 223	150 <i>ns</i>	100	2825
08 Oct.	25h	233	264 → 278	150 <i>ns</i>	100	5974
16 Oct.	12h	295	300 → 380	150 <i>ns</i>	100	2812
24 Oct.	11h	295	380 → 405	150 <i>ns</i>	170	2686
25 Oct.	42h	348	430 → 465	150 <i>ns</i>	100	20984

Table 3.1: Main LHC bunch configurations for 2010 run. *Duration* is the cumulative time of life for all fills with the same bunch scheme. The number of protons per bunch  $N_p$  may have varied for different LHC fills with the same bunch configuration.  $L$  is the rounded total integrated luminosity recorded by the CMS detector, taking into account efficiency. In total, this corresponds to roughly  $43pb^{-1}$  from which  $40pb^{-1}$  have been declared as valid for 'Muon' physics analysis (tracking and muon system flagged as good).

## 3.2 CMS detector overview

The central feature of CMS is a super-conducting solenoid magnet (3.8 T), of 6 m internal diameter and 13 m long, providing a large bending power for an efficient momentum measurement of high-energy charged particles. In the return field outside the magnet, 4 muon stations are embedded within the iron return yoke which is used as a hadron-absorber. Each station is composed of several layers of gaseous detectors: technology of drift tubes is used in the barrel, and cathode strip chambers in the end-caps; all complemented by resistive plate chambers.

Within the field volume is the silicon pixel and strip tracker, the crystal electromagnetic calorimeter, and the brass-scintillator hadronic calorimeter. Finally, CMS has also extensive forward calorimetry. All these sub-detectors are described in the next

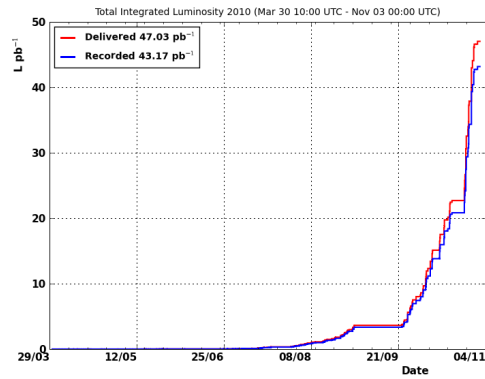


Figure 3.1: Total integrated luminosity delivered to, and recorded by CMS during stable beam at  $\sqrt{s} = 7$  TeV.

sections, emphasizing the one particularly used in the analyzes.

A 3D-view of the main sub-detectors and their locations is displayed in Figure 3.2. The longitudinal and transverse views, with technical lengths, are shown in Figure 3.3.

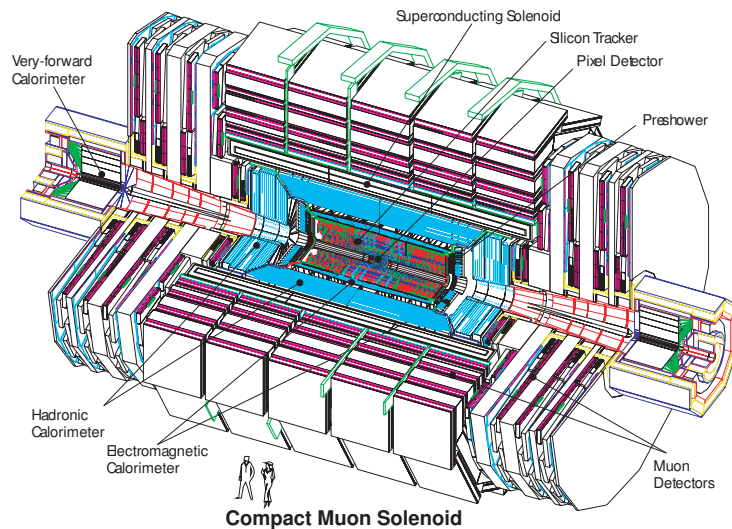


Figure 3.2: CMS detector 3D view

The design of the detector has been chosen to fulfill the prime goals of the LHC programs:

- for the search of the Standard Model Higgs boson in the range  $2m_Z < m_H < 600$  GeV , one needs a good muon identification, momentum resolution, plus a good dimuon mass resolution for the  $H \rightarrow ZZ \rightarrow \mu^+ \mu^- \mu^+ \mu^-$  process;
- within the range  $114 \text{ GeV} < m_H < 2m_Z$ , the two-photon decay mode of the Higgs requests good electromagnetic energy resolution, fine EM granularity, good diphoton mass resolution, wide geometric coverage,  $\pi^0$  rejection, and efficient photon and lepton isolation;
- for masses above 700 GeV where the  $WW$  and  $ZZ$  fusion mechanism becomes important, the tagging of resulting high-energy jets in the forward region requests hadron calorimeters with a large hermetic coverage and with fine lateral segmentation;
- the physics beyond the Standard model in general , and supersymmetry in particular, predicts signatures with significant missing energy which demand good missing transverse energy resolution;
- the cascade decays of supersymmetric particles result in an abundance of  $b$ -jets and  $\tau$ -jets, demanding an efficient triggering and offline tagging of these particular jets with tracking detectors close to the interaction region;
- the search of new massive vector bosons as  $Z' \rightarrow \ell^+ \ell^-$  needs also good lepton momentum resolution and ability to determine unambiguously the charge up to  $E \simeq 1$  TeV.

Along the next lines, the pseudo-rapidity  $\eta$  is used instead of the polar angle  $\theta$ :

$$\eta = -\ln \left( \operatorname{tg} \frac{\theta}{2} \right) \quad (3.4)$$

and varies from 0 ( $\theta = 90^\circ$ ) to infinity ( $\theta = 0^\circ$ ). The jargon usually refers to low- $\eta$  region as the *central* region, while large- $\eta$  ones are called *forward* regions.

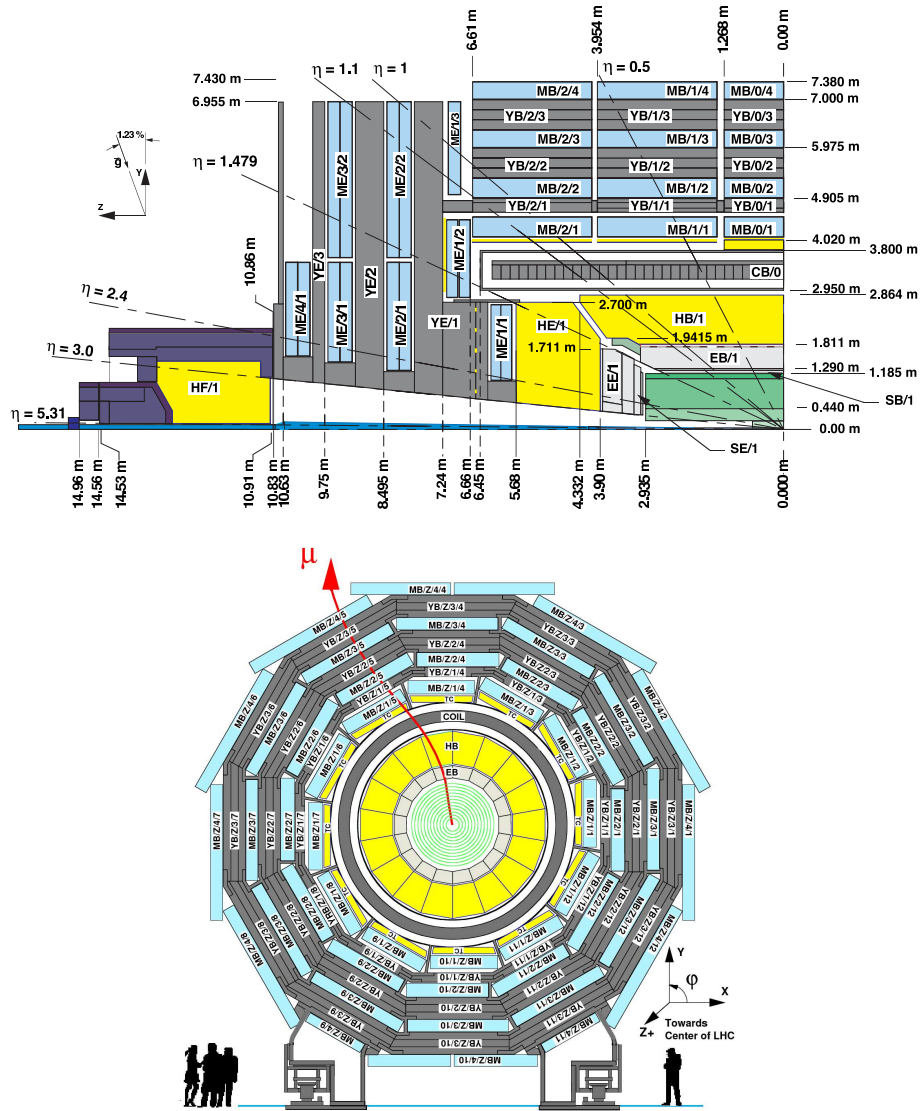


Figure 3.3: Two-dimensional views of the CMS detector. Top: Longitudinal view of a quarter of detector with metric and rapidity coordinates (the muon station ME42 is missing on the drawing). Right: Transversal view,  $z = -2, -1, 0, 1, 2$  depending on the wheel concerned. All dimensions are indicated for magnetic field off.

### 3.3 Central sub-detectors

The central region of CMS is composed of tracking and calorimeter detectors which cover roughly the region between  $-2.5 \lesssim \eta \lesssim 2.5$  and  $-3 \lesssim \eta \lesssim 3$  respectively (see Figure 3.3). The arrangement, aiming to enclose at maximum the interaction point of the collisions, implies a different orientation of the detectors with respect to the beamline based on their position. As the modules are placed like on a cylindrical surface, one refers to the "barrel" region when they are oriented parallel to the beam and to the "endcap" regions for locations with detectors placed perpendicular to beam.

#### Pixel and Strip detectors

The tracker of CMS, the closest sub-detector to the interaction point, aims to the measurements of charged particles originating from the collisions and propagating to the outer in an homogeneous magnetic field of 3.8 Tesla. In addition, informations collected with several close tracks is used to reconstruct primary and secondary vertices (see 3.5.2).

Full silicon technology is used for the sensitive module in order to fulfill the requirements to have high-granularity and fast response, while limiting the amount of material to avoid as much as possible multiple scattering, bremsstrahlung,  $\gamma$  conversion and nuclear interactions. Furthermore, silicon is supposed to be radiation-hard able to survive the high rate density of 1 MHz/mm<sup>2</sup> on the first layer located at a radius of 4 cm from the IP [2].

The tracker is constituted of 4 different sub-systems as represented in Figure 3.4:

- the pixel detector (PXL) made of 3 cylindric layers of cells ( $100 \times 150$  mm<sup>2</sup>) at radii of 4.4, 7.3 and 10.2 cm in the barrel, complemented by 2 disks on each endcap side. It delivers 3 high-precision space points at the beginning of the trajectory.
- the Tracker Inner Barrel (TIB) and Disks (TID) extend in radius up to 55 cm and are composed of 4 barrel layers plus 3 disks of silicon strip sensors. It delivers up to 4 measurements on the trajectory with a point resolution between 23  $\mu$ m and 35  $\mu$ m.

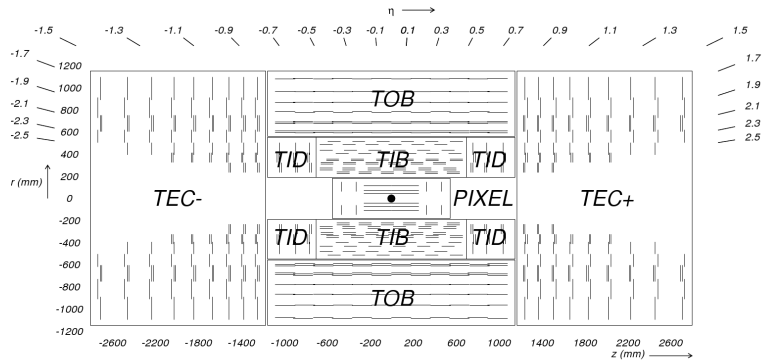


Figure 3.4: Schematic cross-section through the CMS tracker. Each line represents a detector module, double lines indicating back-to-back modules [2].

- the Tracker Outer Barrel (TOB) with an outer radius of 116 cm consists in 6 layers of strips. It provides another 6 hit measurements with  $35 \mu\text{m}$  and  $53 \mu\text{m}$  resolution.
- the Tracker Endcaps (TEC) cover the region between  $124 \text{ cm} < |z| < 282 \text{ cm}$  and consist in 9 disks with rings of silicon micro-strips.

Strips are put in parallel to the beam axis in the barrel and radial in the endcaps. In addition, the modules in the two first layers and rings of TIB, TID and TOB, as well as rings 1, 2 and 5 of TECs carry a second strip module which is mounted with a stereo angle of  $100 \text{ mrad}$  to provide a measurement of the  $z$  coordinate in the barrel and the  $r$  coordinate in the disks. This layout ensures to particles emitted within  $|\eta| < 2.4$  to have at least 9 hits in the silicon strip detector with at least 4 two-dimensional measurements.

The length and thickness of the strips vary with the distance to the IP in order to keep the occupancy at an acceptable level. The total material budget increases then from  $0.4X_0$  at  $\eta = 0$  to  $1.8 X_0$  at  $|\eta| = 1.4$ , beyond which it falls to about  $1 X_0$  at  $|\eta| = 2.5$ . The CMS tracker surface covers  $200 \text{ m}^2$  of active silicon area, with a total of 9.3 millions strips and 66 millions of pixel cells.

## Electromagnetic calorimeter

The design of the ECAL was drawn to increase the capability of CMS to detect the  $H \rightarrow \gamma\gamma$  process at the LHC. The requirement is then to have a fast calorimeter, with fine granularity and radiation-hard. To fulfill it, lead tungsten ( $PbWO_4$ ) crystals have been used as there are dense matter, short radiation length ( $X_0 = 8.9$  mm) and fast enough to emit within the first 25 ns 80% of the scintillation light generated by passage of electrons and photons through it.

The granularity of the barrel EB is 360-fold in  $\phi$  and  $2 \times 85$ -fold in  $\eta$ . A total of 61'200 crystals, with truncated pyramidal shape are mounted with a  $3^\circ$  angle with respect to the IP projection in order to avoid cracks aligned with the particle trajectories. The total length is around  $25.8 X_0$ . Crystals are contained in alveolar structures called sub-modules, grouped into modules of 400-500 crystals depending on the  $\eta$  position. A pair of avalanche photo-diode is then mounted on each crystal, which are grouped  $5 \times 5$  in the readout system.

The EE calorimeters, covering the region  $1.479 < |\eta| < 3.0$ , are made of 7324 crystals with off-pointing angles ranging from  $2^\circ$  to  $8^\circ$  for a total length of  $24.7 X_0$ . Endcap crystals are grouped in  $5 \times 5$  crystal structures called super-crystals.

Front of the EE crystals, the preshower detector has been installed aiming to identify neutral pions and single high-energy photon within  $1.65 < |\eta| < 2.6$ . It is a sampling calorimeter made of lead radiators to initiate the electromagnetic shower from  $e^-/\gamma$  particles, and silicon strip sensors to measure the energy deposit. Total thickness of the calorimeter is  $2X_0$  before the first sensor plane and  $3X_0$  before the second one, such that 95% of photons will start showering before the second sensor layer.

## Hadronic calorimeter

The hadronic calorimeter is composed of four separate sub-detectors: barrel (HB), endcap (HE), outer (HO) and forward (HF). The later one is described separately in the Forward section 3.4. The barrel one is a cylindrical calorimeter placed between the outer extend of the EB ( $R=1.77$  m) and the inner extend of the magnet ( $R=2.95$  m) and divided into two half sections in  $z$ . Each half consists in 18 identical azimuthal wedges made of a front (50.5 mm) and back (75 mm) steel plates around 14 brass absorber plates (8 of 50.5 mm and 6 of 56.5 mm) aligned parallel to the beam axis. The total HB-thickness increases with  $\theta$  as  $1/\sin(\theta)$ , starting with  $5.82$  hadronic interaction length ( $\lambda_I$ ) at  $\eta = 0$  up to  $10.6 \lambda_I$  at  $|\eta| = 1.3$ . The crystals from ECAL in front of HB bring another  $1.1 \lambda_I$ .

Plastic scintillators are build out of tiles coupled to wavelength shifting (WLS) fibers to bring out the light. To avoid reading the 70 000 tiles composing the HCAL of CMS, tiles of the same  $\phi$  layer are put together into the single scintillator tray unit. Light of each unit is collected by a 0.94 mm-diameter WLS fiber placed in a machined groove into the scintillator. After exiting the scintillators, WLS fibers are spliced to clear fibers, which are finally connected to photo-diodes. Each wedge is then segmented in 4  $\phi$  sectors, and the plastic plates divided in 16  $\eta$  towers.

The HE calorimeter covers the pseudo-rapidity region  $1.3 < |\eta| < 3.3$ . The operation and design are very similar to HB, with the purpose to minimize cracks with HB, rather than to have a good single particle response. The absorbers are bolted brass plates of 79 mm-thickness for a total length of  $10 \lambda_I$ . HE tower granularity is similar to HB for  $|\eta| < 1.6$  and increases to  $(\Delta\eta \times \Delta\phi) = 0.17 \times 0.17$  after  $|\eta| = 1.6$ . In addition, some regions of HE are also segmented longitudinally: towers  $27 \rightarrow 29$  close to the beamline have 3 divisions in depth that are readout separately, while towers  $18 \rightarrow 26$  have 2 longitudinal readouts.

Finally, the HO is placed outside the solenoid to complement the containment of the hadrons showers within the central region. HO uses magnet coil as an extra absorber to extend the equivalent depth to a minimum of  $11.8 \lambda_I$ . It is then used to identify late starting showers and to measure the shower energy deposit after HB. The HO consists of one or two (in the very-central part) layers of scintillators tiles located in front of the first layer of the barrel muon detector. Scintillation light is collected by WLS fibers to photo-detectors located on the structure of the return yoke. Each optically independent tiles formed of 4 WLS is then mapped to a tower of HB in the readout.

## Muon chambers

The muon system is composed of 1'400 chambers forming 4 layers of concentric cylinders, called "station", and inserted among the layers of the magnetic flux return plates, in both barrel and endcap regions. Three different kinds of detectors are used, all working with gaseous technology, *i.e.* collection of charges from the gas ionization produced by the passage of charged particles through it.

In the barrel ( $|\eta| < 1.2$ ), because of low muon rate and uniform magnetic field, the muon system uses Drift Tubes (DT). The DT system is composed of 4 layers (labelled MB1 to MB4 in Figure 3.3) of 60 drift chambers, for a total of approximately 172'000 tubes, each containing a stretched wire in a volume of gas. The drift time of the electrons produced out of the ionization and the position of the wire hits provide a timing plus  $2D$ -coordinate measurements. The stations have 8 chambers with wires parallel to the beam and provide a track measurement in the  $r - \phi$  coordinates. In addition, the 3 first stations have also 4 chambers with wires orthogonal and therefore measuring the  $z$  position along the beamline.

In the endcap regions ( $0.8 < |\eta| < 2.1$ ) where the muon rate is high and the magnetic field uneven, the Cathode Strip Chambers (CSC) are used. It consists of arrays of positively-charged anode wires perpendicularly crossed with negatively-charged copper cathode strips within a gas volume. Each side contains 4 stations with chambers perpendicular to the beam, in which strips provide a measurement in  $r - \phi$ ,  $\eta$  and timing information.

A complementary system, the Resistive Plate Chambers (RPCs), is installed in both the endcap and barrel regions ( $|\eta| < 1.6$ ) and provide a fast, independent and highly-segmented trigger signal with good timing resolution but coarser position resolution than the DTs and CSCs. A RPC consists of two parallel plates, a positively-charged anode and a negatively-charged cathode, both made of a very high resistivity plastic material and separated by a gas volume. A total of 6 layers of RPCs are embedded in the barrel muon system, 2 in the first 2 stations, and 1 in the last 2 stations. The redundancy in the first 2 stations allows the trigger algorithm to work even for low- $p_T$  tracks that may stop before reaching the outer 2 stations. In the endcap region, there is a plane of RPCs in each of the first 3 stations in order for the trigger to use the coincidences between stations.

### 3.4 Forward sub-detectors

At the LHC, the region located at  $|\eta| > 3$  is exposed to an extremely high flux of energy carried by particles produced at small-angles during  $pp$  collisions. The energy flow was measured to be non-uniform with the rapidity, with maximum energy deposit at highest  $\eta$  as foreseen [57]. The design of the forward detectors has therefore been driven by the need to survive at least 10 years within this harsh environment. As a consequence, quartz has been chosen for the active material in the three current forward sub-detector of CMS (HF, CASTOR and ZDC) because of its radiation hardness, its fast signal response and its ability to build compact calorimeters [58].

#### Hadronic Forward calorimeter

The two HF calorimeters [59] are symmetrically located at  $\pm 11.2\text{m}$  from the IP covering the pseudo-rapidity region  $\eta = [2.866; 5.205]$ . It consists in a 130 cm-radius 165 cm-long cylinder, made of steel absorber (equivalent to  $10 \lambda_I$ ) in which has been drilled a grid of grooves parallel to the beamline and separated by 5 mm center-to-center. In these grooves stand some quartz fibers alternating between long fibers (starting at the front of the detector) and short ones (starting at 22 cm depth).

The arrangement allows to distinguish signals generated by electrons and photons, which deposit a large fraction of their energy in the first 22 cm, from hadrons which produce equal signals in both sections on average. The signal consists of Cerenkov light generated by the passage of relativistic charged particles through the quartz. Only a small fraction of the light is collected and coupled by light-guides to radiation-shielded PMTs. The calorimeter of each side is segmented in 18 wedges of  $20^\circ$  in  $\phi$  and 13 rings with almost similar coverage in  $\Delta\eta \simeq 0.175$ .

#### CASTOR

The CASTOR detector [60, 61], which stands for "Centauro And Strange Object Research", is a sampling calorimeter with alternate plates of tungsten ( $W$ ) –as absorber– and of fused silica quartz ( $Q$ ) –as active medium–, for a total depth of  $10.3 \lambda_I$ . Plates are tilted with a  $45^\circ$  angle to maximize the collection of Cerenkov light. Located at 14.38 m from the interaction point on one side only, CASTOR geometry is designed to enable the observation of cascade development along the passage of the incoming charged particles in the acceptance range  $-6.6 < \eta < -5.1$ .

The calorimeter is segmented in 16 symmetric sectors in  $\phi$  around the pipe, and 14 sections in  $z$ : 2 for the EM part and 12 for the HAD one. There is no segmentation in

$\eta$ . Each EM part consists in a sandwich of 5  $W$  and 5  $Q$  plates of 5 mm and 2 mm respectively; while a HAD channel is composed of 5  $W$ - $Q$  plates of 10 mm and 4 mm. Cerenkov lights produced in these 224 channels are grouped per 5  $W$ - $Q$  plate pairs, and then collected along the length and focused by air-core light guides onto PMTs.

The addition of the CASTOR detector, which extends the full pseudo-rapidity coverage of CMS to  $\Delta\eta \simeq 11.5$  instead of 10 with HFs only, deserves many physics research [62]. For instance, to compute MET as a signature for new physics; to search for very backward jet from Higgs production through vector boson fusion; by means of the EM and HAD sections, to study the shower profile and to search for Centauro-type events, *i.e.* high-density showers produced by charged pions entering the atmosphere. Besides these researches for new physics, the CASTOR detector is also useful for QCD-type of physics: study of multi-parton interactions and underlying events, low- $x$  physics, diffraction and quark-gluon plasma.

### Zero Degree calorimeter

The ZDC detectors [63] are, as for CASTOR, sampling calorimeters made of  $W$  as radiator and quartz fibers ( $QF$ ) as active medium. Two identical calorimeters are located at  $\pm 140$ m of the interaction point, in the first neutral particle absorber of the LHC (TAN). The location has the advantage that charged particles have been deflected downstream by dipoles which aimed to separate incoming and outgoing beams into two pipes, such that zero-degree calorimeters are sensitive only to photons and neutrons with  $|\eta| > 8.1$ .

Each ZDC has an electro-magnetic and a hadronic section of  $7.5 \lambda_I$  in total. The EM is composed of a sandwich of 33 layers of  $W$  (2 mm width) and  $QF$  (0.7 mm width) oriented vertically and segmented in the transverse direction in 5 readout towers. The HAD section is composed by a sandwich of 24 layers of  $W$  (15.5 mm width) and  $QF$  (0.7 mm width) tilted by  $45^\circ$  and segmented longitudinally in 4 readout towers. The design also includes a 9 mm  $Cu$  plate front and back of each section. The fibers, grouped in bundles, are directly connected to the PMT in EM, while in HAD they are coupled via air-core light guides.

Although ZDC is mainly dedicated to heavy-ion runs, where it will be used to measure the reactions centrality by counting the number of spectator neutrons, some applications are already available in  $pp$  mode. For instance, one can quote the tagging of bremsstrahlung photons and neutrons from charge exchange reaction, but also to select diffractive events and reject proton-dissociative background.

## Forward Shower Counters

In the late March 2011, the FSC collaboration managed to install scintillator counters close to the beam-pipe in the region  $60 \text{ m} \lesssim |z| \lesssim 115 \text{ m}$  around CMS [64, 65]. These counters, covering the pseudo-rapidity region  $7 < |\eta| < 11$ , may detect the showers created by particles produced at small angles and interacting with the pipe or the surrounding material.

Scintillators, made from  $25 \times 25 \text{ cm}^2$  solid hard plastic with 1cm width and embedded into fibers connected to photo-multipliers, have been placed at specific spots where the elliptical beam is accessible. At  $z = 59.1 \text{ m}$  and  $z = 84.8 \text{ m}$ , two beam scintillator counters (one above, one below the beam-pipe) with half elliptical boundaries in order to fit the pipe shape are installed. At 114.1 m, four of them are put around the beamline, each with a corner cut out by a quarter of a circle.

The deployment of such detectors will be useful in 2011 runs as they may be used as (large) rapidity gap detectors for exclusive processes, and as a veto in  $L1$  trigger for both incoming and outgoing beam-halo background. In addition, they aim to measure forward showers from low-mass diffractive events.

## High Precision Spectrometer project

Another project consisting of installing proton detectors at 240 m and 420 m from IP5 is also in consideration within CMS. Aiming to detect forward scattered protons which survived from an exclusive interaction, the next chapter is entirely dedicated to this.

## 3.5 Event flow reconstruction

The reconstruction process, from the particle detection by the sub-detectors to the high-level objects as used in the next analysis, is a 3-step process. Firstly, local reconstruction within the respective sub-detectors, from the "digis" type of data to "recHits" type, which are usually position measurements and calorimeter clustering. Secondly, information from different modules of a sub-detector are combined (ex: all the tracker recHits are used to built a track). Finally, the last step consists in the combination of all reconstructed objects from different sub-detectors to create high-level candidates (ex: combining tracks from the tracker with calorimetric clusters to get an  $e/\gamma$  candidate). Only reconstruction of high-level objects used in the next sections (track, vertex, caloTower and muon) are described in the next paragraphs.

### 3.5.1 Tracks

The default track reconstruction algorithm in CMS, also used during the analysis, is the so-called '*Combinatorial Track Finder*', or CFT [2, 67]. The reconstruction follows a 5-steps procedure in which the pattern recognition plays a leading role.

Starting with the seed parameters and its covariance matrix, a combinatorial Kalman filter proceeds iteratively to build trajectory by extrapolating the track parameters to the next compatible layers with the equation of motion in magnetic field, taking into account energy loss and multiple scattering. At each step the algorithm creates, for compatible hits of the layer, a new trajectory. The track parameters are therefore updated with the new pieces of information of the compatible hits and correctly weighted according to (current and previous) hit measurements and trajectory predictions. The procedure of extrapolation is repeated until either the outermost layer of the tracker is reached, either no compatible hit is found.

### 3.5.2 Primary vertex

Using the full set of promptly reconstructed tracks, the primary vertex (PV) reconstruction is a 4-steps process, splitted between the vertex finder [68] and the vertex fitter [69] algorithms.

The performances of the PV reconstruction is studied in [70, 71]. One clearly sees an improvement of the resolution with increases number of tracks and their average transverse momenta. However, even for exclusive dimuon vertices composed of 2 low- $p_T$  tracks, the efficiency is still  $\sim 99\%$ , with a resolution of  $180 \mu\text{m}$  in transverse and longitudinal directions. The effect of misalignment was estimated to be at most  $20 - 30 \mu\text{m}$  on the resolution. An independent cross-check of the 2-tracks PV reconstruction is done in Section 6.3.2, and we found a  $98.5\%$  efficiency for a 2-tracks PV.

The effect of overlap interactions within the same bunch crossing may have two different effects known as *splitting* and *merging* which can have influences in the search of exclusive vertex. The merging is due to the fact that vertices separated in  $z$  by 2 mm or less are merged into a single reconstructed vertex. This effect was found to be  $7\%$  in early data at 7 TeV where  $\sigma_z = 4.6 \text{ cm}$ . The splitting rather happens when a soft interaction with small number of tracks is, due to the fine clustering of 2 mm, reconstructed as multiple vertices near the main one. It was computed in early data that the probability of splitting is  $0.3\%$  only.

On the one hand, the effect of the merging implies that exclusive vertices produced within the same bunch crossing and with  $\Delta z < 2$  mm are merged together, with an impossibility to disentangle the two interactions. On the other hand, splitting may lead to selecting fake exclusive vertices as composed of only 2 tracks.

### 3.5.3 Calorimeter towers

Rather than using the information from each single crystal of the ECAL and HCAL, analyzes rather use CaloTowers built with information from both calorimeters. Each of these non-physical objects is constituted with all ECAL and HCAL cells contained in a respective  $\eta - \phi$  region, following the segmentation of HCAL. The EM and HAD part of the energy of a CaloTower is obtained by summing ECAL and HCAL RecHits energies, with a minimum threshold to be reached otherwise set to zero.

Calorimeter tower objects are used for the calorimeter-based jet reconstruction and for the computation of the missing energy. In our purpose, there will be used to characterize the exclusivity conditions in the central and HF calorimeters.

### 3.5.4 Muon reconstruction

The reconstruction of muons within the central detector is a multi-step process, combining information from the silicon tracker and the muon spectrometer. Full details about the reconstruction parameters, algorithms, propagators, etc. may be found in [72]. After the local reconstruction of hits within the DT 1D cell, CSC 2D planes and RPC 1D, track segments are built with matched DT and CSC hits to provide seeds for the next steps of reconstructions:

#### Stand-Alone muon

A pre-filter (to refine the seed state) and then the filter, both based on a combinatorial Kalman technique, are applied from the outermost (innermost) layer until the innermost (outermost) compatible layer for the filter (pre-filter) process. Based on the same Kalman algorithm as the track fitter in the silicon tracker, muon track parameters are extrapolated iteratively to the next layers of the muon system, and trajectory parameters are updated at each step with the information from the new measurement. The propagation is done taking into account multiple scattering, ionization and bremsstrahlung in the chambers and the iron yoke. To consider the non-uniformity of the magnetic field further, the propagation is performed with smaller steps with a helix parameterization in regions with large inhomogeneities in the field.

**Global muon**

For each stand-alone muon, a tracker track matching is performed, starting by defining a rectangular region of interest in  $\eta - \phi$  to choose the initial set of tracks candidates roughly compatible with the stand-alone muon. Secondly, the matching of the tracker and muon tracks is done by comparing parameters after extrapolation on a common surface. Depending on the case, this surface may be the tracker outer surface, the innermost boundary of the muon system, the detector surface of the outermost tracker track hit or the innermost muon track hits. The selection is thus done such to minimize the covariant error matrix of the propagated tracks and to reduce the number of matches per muon. Finally, for all matching pair of a tracker-track – stand-alone muon, a global refit of the silicon hits and muon hits is performed in once

**Tracker muon**

A complementary approach to the global reconstruction consists to rather consider all tracker tracks as muon candidates and check for compatible segments in the muon system. This type of reconstruction is particularly suited for low- $p_T$  muons which may not leave enough hits in the muon stations to be reconstructed as a stand-alone, or to recover muons lost between wheels gap.

## 3.6 Trigger system

In order to observe a maximum of collisions during the beam life-time, the beam-crossing rate at the center of CMS is configured to be high, with a maximum of 6 MHz during 2010 (and up to 40 MHz for the nominal design). Moreover, for each beam-crossing, several collisions occur simultaneously. Since it is impossible to process and to store the large amount of data produced during these collisions, one needs to perform a large reduction of the rate. This task is achieved by the trigger system and is divided into two steps:

- the Level-1 system ( $L1$ ), based on electronic hardware to reduce it to 100 kHz,
- the High-Level system ( $HLT$ ), a software system to filter the rate to 100 Hz.

The  $L1$  uses coarsely segmented data provided by the CSC,DT and RPC independently (4 muon candidates) and by the ECAL, HCAL and HF (8  $e/\gamma$  candidates, 8 jets, 4  $\tau$ s,  $\sum E_T$ ,  $E_T^{miss}$ , ...) as input for logical decisions. The  $L1$  trigger, which has to analyze each event, has a maximum latency of 3.2  $\mu$ s between a given bunch-crossing and the distribution of its decision to the front-end electronic memories in which high-resolution data is temporarily stored. Consequently, the process needs to make use of

a buffer, designed to store a maximum of 128 events.

The *HLLT*, on the contrary to the *L1*, has access to the complete read-out data and can therefore perform complex calculations. A farm of a thousand of commercial processors is used to run the selection algorithms. A long list of trigger paths have been created, for commissioning or physics purposes. Among them, one can spot the ZeroBias trigger which selects every beam-crossing event whether there is an interaction or not; it will be used for the commissioning of the exclusivity conditions in Chapter 5. It is also worth mentioning the existence of an exclusive  $e/\gamma$  pair trigger, selecting events with low occupancy in the HF detectors. For all triggers, the cut values as well as the applied prescales are varying along the data-taking period in order to keep the output rate constant at 100 Hz while the beam intensity and crossing frequency are changing. The details about the dimuon triggers used for the 2010 analysis are contained in Appendix A.





## Chapter 4

# The High Precision Spectrometer project and Gastof detectors

*“To go forward is to move toward perfection”*

Kahlil Gibran

The HPS project consists in the installation of very-forward detectors close to the beamline of the LHC with the purpose to reconstruct outgoing protons from an exclusive interaction. The physics motivations, an overview of the prototypes and expected acceptance are quoted in Sections 4.1, 4.2 and 4.3 respectively. Finally, studies on the GASTOF detector aiming to reduce background from accidental triple coincidence are reported in Section 4.4 and 4.5.

### 4.1 Physics with very forward detectors at the LHC

In the LHC optical environment, magnets will work as a spectrometer and bend the protons which have lost a small fraction of their initial energy (as for instance outgoing protons from  $pp(\gamma\gamma) \rightarrow pXp$ ), as it is shown in Figure 4.1.

Similar techniques of proton spectrometers with forward detectors have already been applied at CDF [73] and D0 [74] experiments at TEVATRON , H1 [75] and ZEUS [76]

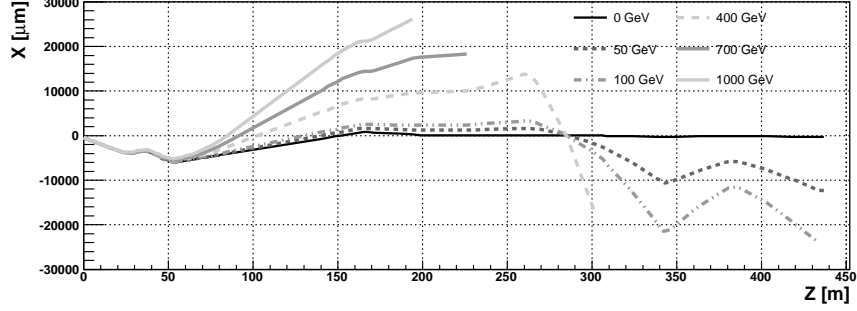


Figure 4.1: Proton path for different energy loss. Path is stopped when the proton encounters an obstacle from the LHC beamline (quadrupole, beam monitor, . . .)

at HERA, PP2PP [77] and STAR (proposal) [78] at RHIC or TOTEM [79] at the LHC.

Detectors have to be installed in the high-dispersion region at  $\pm 240$  m and  $\pm 420$  m, where the scattered protons are well distinguishable from the ones of the beamline. Figures 4.2 show the contours for positions and angles of a realistic sample of scattered protons from the  $pp(\gamma\gamma) \rightarrow pW^+W^-p$  process at  $\sqrt{s} = 14$  TeV simulated with MadGraph [80] and propagated into the LHC line with the Hector software [81] assuming half-crossing angle of  $142.5 \mu\text{rad}$ , with an angle dispersion of  $30.25 \mu\text{rad}$  and a beam energy dispersion of  $0.79$  GeV. The 90% contour of the 7 TeV protons is also highlighted by the red ellipse. The  $x$  position of the scattered protons in very forward region is, at first approximation, only function of the fraction of energy loss as:

$$\Delta x = D(s) \frac{\Delta E}{E} \quad (4.1)$$

where  $D(s)$  is the beam dispersion and is a function of the total path length  $s$  as one can see at Figure 4.1. As there are no beam dispersion in  $y$ , the spread in  $y$  is just due to the vertex smearing. The positions and angles of the same sample of scattered protons as a function of the energy loss is displayed in Figure 4.3.

The original motivation to install very forward detectors at the LHC is for the search of exclusive Higgs production in CEP, as in Figure 2.12. Indeed, measurements of outgoing proton momenta and energy loss—as they are directly related to the invariant mass of the system—allow a Higgs mass reconstruction with a 2 GeV resolution, irrespectively to the decay mode, even for final states containing jets or neutrinos, thanks to

the missing mass method [82]. In addition, if this measurement is done in coincidence with the central detector, kinematics of the Higgs boson are then fully constrained and all quantum numbers are accessible, including the spin. Beyond Higgs physics, the addition of such detectors would help to achieve the physics goals of CMS listed in 3.2 and would open up a new rich program of QCD, EWK and BSM physics.

In the first stage, when HPS-240 only will be available, only the protons which have lost a significant energy would be detectable, and hence only the masses above 200 GeV will be reachable (Figure 4.5). However, such a limited apparatus will already give access to some interesting and unique physics subjects, with for instance the study of QCD in diffraction, in CEP and in  $\gamma p$  interactions. The high-mass electroweak sector can also be probed in  $\gamma\gamma$ , by searching for anomalous couplings in  $\gamma\gamma \rightarrow W^+W^-$  or deviations in the mass spectrum from BSM physics. As an example, the phenomenology of the two-photon production of supersymmetric pairs is studied in Chapter 8.

In the second stage, the inclusion of detectors at 420 m will extend the range of detectable energy loss down to 20 GeV, and also provide extra measurements in the intermediate regime thanks to crossed  $240 \times 420$  detection. That includes the measurement of the mass and quantum numbers of the Higgs boson. The reason of the delay between the installation of 240 m and 420 m stations is mainly due to the extra engineering needed for the replacement a long cryogenic connexion by a warm pipe section plus a cryogenic bypass [83].

## 4.2 High Precision Spectrometer detector overview

The detector stations consist of a silicon tracking system which can be moved transversally thanks to a special movable beam pipe with the detectors integrated on it. During beam injection, acceleration into the LHC pipe and luminosity tuning, the detectors are parked in a safe place far from the beam line; when beam cleaning and collimation have been performed, the detectors can move step-by-step to their optimal positions.

The method to reconstruct the energy of the scattered protons initial energy is to measure the displacement and the angle at several points in a  $\sim 8$  meters-long region. To obtain the target resolution of 2 GeV on the central system mass, one would need resolutions of  $\sim 10 \mu\text{m}$  in  $x$  and  $\sim 1 \mu\text{rad}$  in  $\theta$ : these resolutions can be obtained in the tracking system by the use of 3D or pixel silicon detectors. In addition, 3D silicon has the advantage to own very small dead space and fast response.

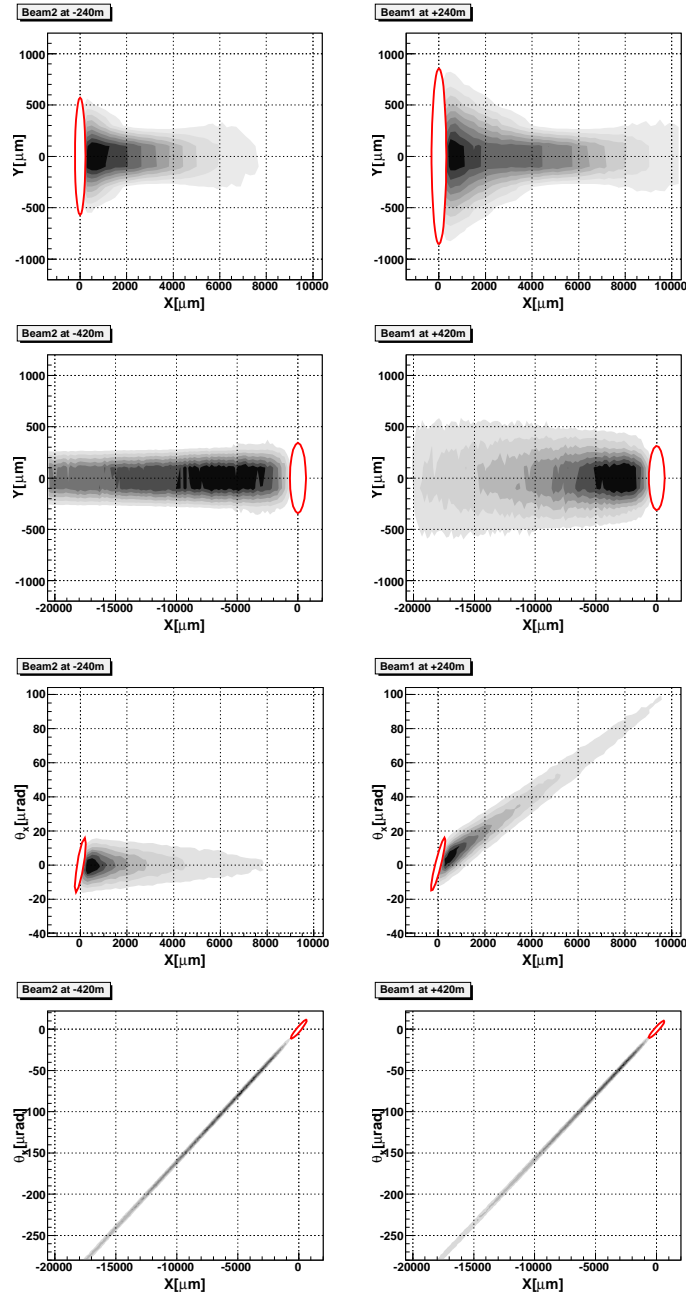


Figure 4.2: Positions and angles distribution for generated events  $\gamma\gamma \rightarrow W^+W^-$  Top:  $(x, y)$  proton positions of arrival. Down:  $(x, \theta_x)$  proton values. Distributions are divided between beam1/beam2 and  $s = 240/420$  m.

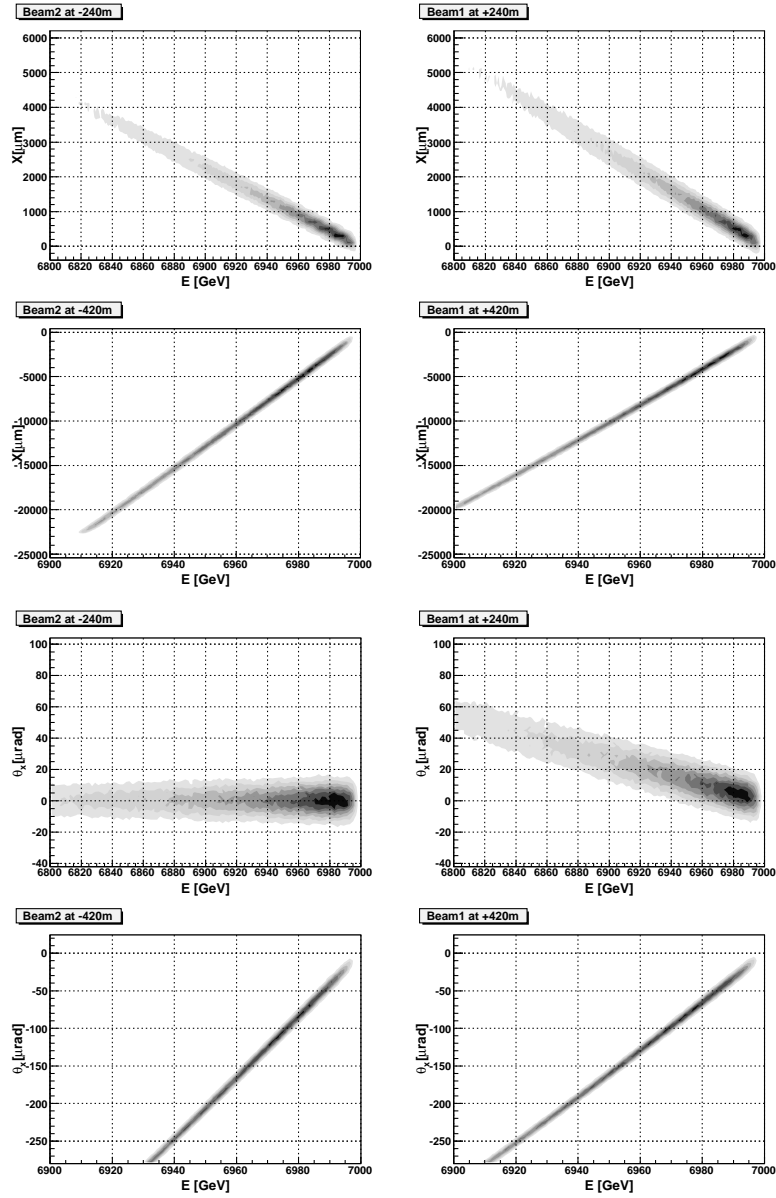


Figure 4.3: Horizontal positions and angles dependence on the proton energy loss for generated events  $\gamma\gamma \rightarrow W^+W^-$ . Top:  $(E, x)$  proton positions of arrival. Down:  $(E, \theta_x)$  proton values. Distributions are divided between beam1/beam2 and  $s = 240/420$ m.

### 4.3 HPS acceptance

In the following, a photon-exchange process is assumed tagged if the scattered proton is detected into very forward stations at 240 m or 420 m. The detection criteria taken in the next imply that the proton position has to be measured at both 240 m and 248 m to be considered as detected in HPS-240, and similarly for HPS-420. Partially detected protons by only one of the two stations at  $\sim 240$  m are considered to be affected, and not detectable at 420 m anymore, although there may be in the acceptance. It has its importance when considering non-edgeless silicon detectors for instance. The design of the 8 stations ( $\pm 428, \pm 420, \pm 248, \pm 240$  m) was considered identical for whole of them, except the distance approach. For the next figures, it was chosen 2.5 mm for HPS-240 and 4 mm for HPS-420. That corresponds to a distance of respectively  $16 \sigma_x$  and  $12 \sigma_x$  from the beam center on average.

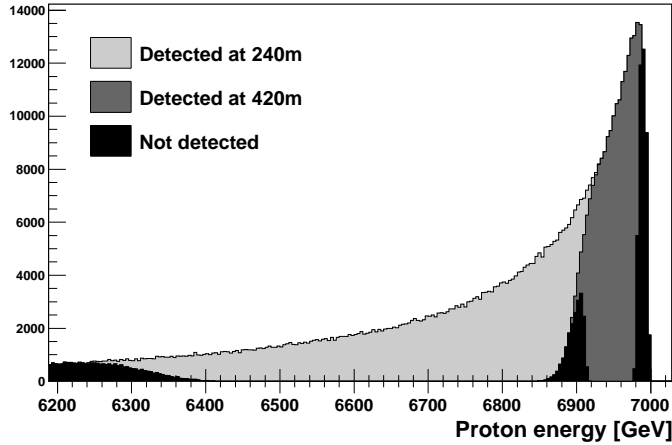


Figure 4.4: Scattered proton energy spectrum (and hence photon energy spectrum) for  $pp(\gamma\gamma) \rightarrow pW^+W^-p$  processes. Kinematic regions where proton detection is allowed are marked, considering a 2.5 mm and 4 mm approach with no dead zone.

The forward station tagging acceptance for scattered forward proton from a realistic sample of  $pp(\gamma\gamma) \rightarrow pW^+W^-p$  process which is given at Figure 4.4 is as a function of  $E_{loss}$  of the proton only, while it actually depends on the momentum transfer  $Q^2$  as well. However, it was shown in [81], at low momentum transfer the acceptance only depends on the energy, and only at high- $Q^2$  the acceptance is lowered because of the larger proton scattering angle induced by the photon emission. As the average photon

virtuality is relatively small,  $\langle Q^2 \rangle \sim 0.01 \text{ GeV}^2$ , one can consider that equation 4.1 is valid. There exists small dead zone (mainly for B2), for protons with energy loss between  $\sim 85 \text{ GeV}$  and  $\sim 120 \text{ GeV}$ , due to the fact the protons are too energetic to be detected at 240 m, but not enough for 420 m.

The convolution of both proton-tagging efficiencies is made to build the acceptance curves for double-tagging, (exclusive) single-tagging and no-tagging as a function of the  $\gamma\gamma$  center-of-mass energy in Figures 4.5. Only two-photon produced events with central system  $X$  within  $|\eta| < 2.5$  are considered to build the graph. The curves are easily understood if one remembers the proton energy range for tagging at 420 m (from  $\sim 20$  to  $\sim 100 \text{ GeV}$ ) and at 240 m (from  $\sim 100$  to  $\sim 700 \text{ GeV}$ ). The single tag spectrum from bottom left is shown separately for 240 m, 420 m and the sum; several regimes are observed <sup>1</sup>.

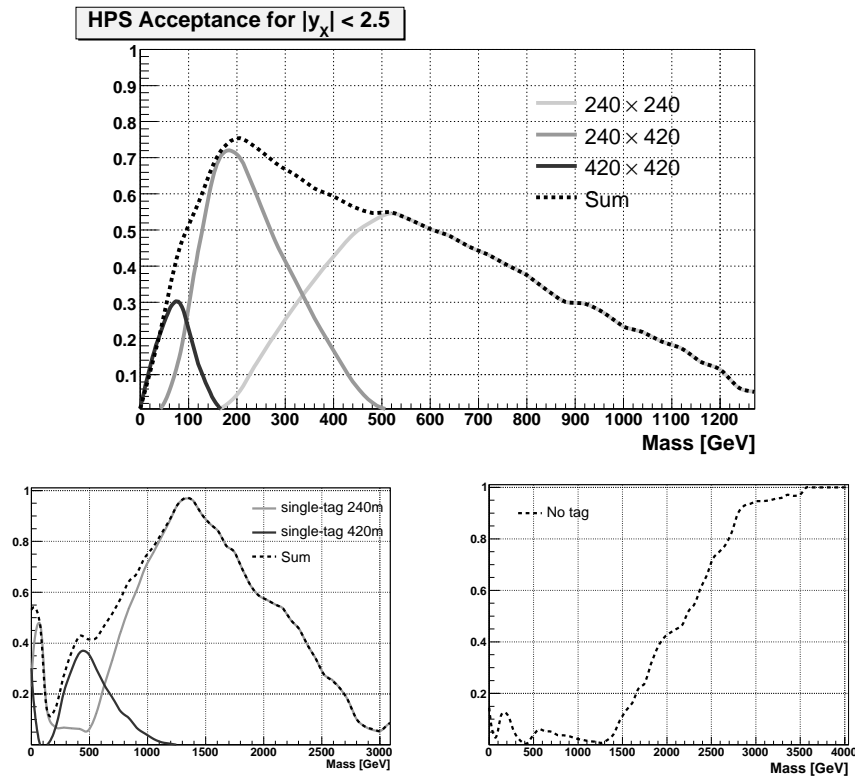


Figure 4.5: Double-tag (top), single-tag (bottom left) and no-tag (bottom right) acceptances for  $|\eta_X| < 2.5$ , assuming a 2.5 mm and 4 mm approach with no dead zone.

To optimize the acceptance for low energy-loss protons, the detectors must operate as close as possible from the beam-line at 420 m, with a maximum of 5 mm (from beam center to the edge of the sensitive area) at 420 m to be sensitive to masses around 100 GeV. For 240 m however, the positions of the detectors will have large influence on the acceptance, at 240 m and at 420 m. This is illustrated in Figure 4.6, showing the acceptance for 3 different scenarii of beam-distance and technology. With respect to

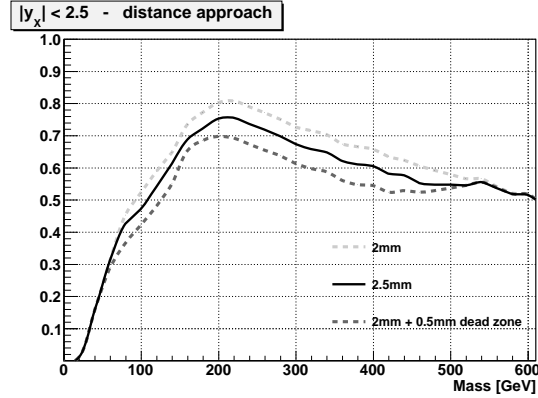


Figure 4.6: Acceptance for  $|\eta_Y| < 2.5$ . Full line is for an edgeless 2.5 mm distance approach, dashed lines are for edgeless 2 mm and 0.5 mm-edge 2 mm distance.

the nominal 2.5 mm edgeless detectors assumed here, 2 others have been considered: some edgeless detectors at 2 mm and some at 2 mm with 0.5 mm dead-edge. In the first case, the approach of 0.5 mm extra in the beam brings a  $\sim 5\%$  gain in acceptance for central system within 75 GeV and 550 GeV. In the second case, when the detectors themselves are at 2 mm from the beam, but the silicon area starts to be sensitive only 0.5 mm after, the acceptance is decreased by 5% in the range [50, 500] GeV. This is due to the shadowing effect of 240 m on 420 m stations, as it is illustrated in Figure 4.7. Going too close to the beam in HPS-240, one starts to enter in the acceptance zone of HPS-420; but if that incursion is covered by dead material protons are affected and cannot be measured neither at 240 or 420 m. Thus, the acceptance can be optimized by choosing different distance-to-beam for Beam1 and Beam2.

<sup>1</sup>For the HPS-240, single-tag is generally possible when one gets asymmetric energies configuration as  $100 < E_{\gamma_1} < 700$  GeV and  $E_{\gamma_2} < 20$  GeV ( $W_{\gamma\gamma} \lesssim 235$  GeV) or  $E_{\gamma_2} > 700$  GeV ( $W_{\gamma\gamma} \gtrsim 530$  GeV). The HPS-240 single-tag probability reaches almost 100% for  $W_{\gamma\gamma} \simeq 1400$  GeV and then decreases linearly, since for larger two-photon masses both protons get often outside the acceptance range. This is also seen in the 'no-tag' acceptance curve at the bottom right which behaves reversely. Similarly, the

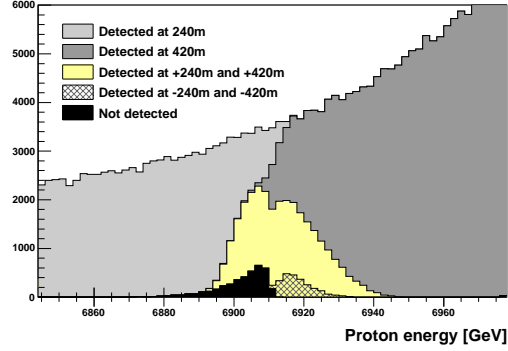


Figure 4.7: Shadowing effect of the HPS-420 by HPS-240 stations for an edgeless 2 mm approach.

The difference in beamline with respect to detectors located at 220 m –as it was assumed in many previous papers– is small. The extra magnetic elements will anyway imply a slight modification in forward angles of the scattered protons kinematics, between  $\pm 220$  m and  $\pm 240$  m, but also between  $+240$  m and  $-240$  m:

For the Beam1:

- a 4.8 m-long quadrupole (MQML), from  $s = 225.99$  m to 230.79 m,
- a 0.9 m-long arc orbital vertical corrector (VKICKER), from  $s = 230.98$  m to 231.88 m,
- a drift section of  $\sim 24$  m with constant angles  $\alpha_x = 3.41$  prad and  $\alpha_y = 4.65$  prad, until the next collimator located at  $s = 255.78$  m.

while for the Beam2:

- a 4.8 m-long quadrupole (MQML), from  $s = 225.99$  m to 230.79 m,
- a drift section of  $\sim 26$  m with constant angles  $\alpha_x = 0.45$  prad and  $\alpha_y = -2.25$  prad, until the next collimator located at  $s = 256.61$  m.

with angle values quoted for 7 TeV beam protons. The configuration has not much influence on the forward  $(x, y)$  positions, and hence the acceptance, but the  $\theta_x$  and  $\theta_y$  angles at forward positions are quite different, as it may be seen in Figure 4.2. As the

---

HPS-420 single tag can be obtained with  $20 < E_{\gamma_1} < 100$  GeV and  $E_{\gamma_2} < 20$  GeV ( $W_{\gamma\gamma} \lesssim 100$  GeV) or  $E_{\gamma_2} > 700$  GeV ( $W_{\gamma\gamma} \gtrsim 235$  GeV).

horizontal drift angle is roughly 8 times bigger for B1 than for B2, the dispersion of forward angles for beam and scattered protons is almost null at  $-240$  m and extend up to  $210 \mu\text{rad}$  at  $+240$  m.

The photon-photon spectrum displayed in Figure 2.6 for 7 TeV beam energy, after HPS acceptance (calculated without  $|y_X|$  constraint), is shown in Figure 4.8. The nominal very forward detector setup will therefore be efficient to tag  $\gamma\gamma$  interactions with invariant masses between  $\sim 20$  GeV and  $\sim 1400$  GeV.

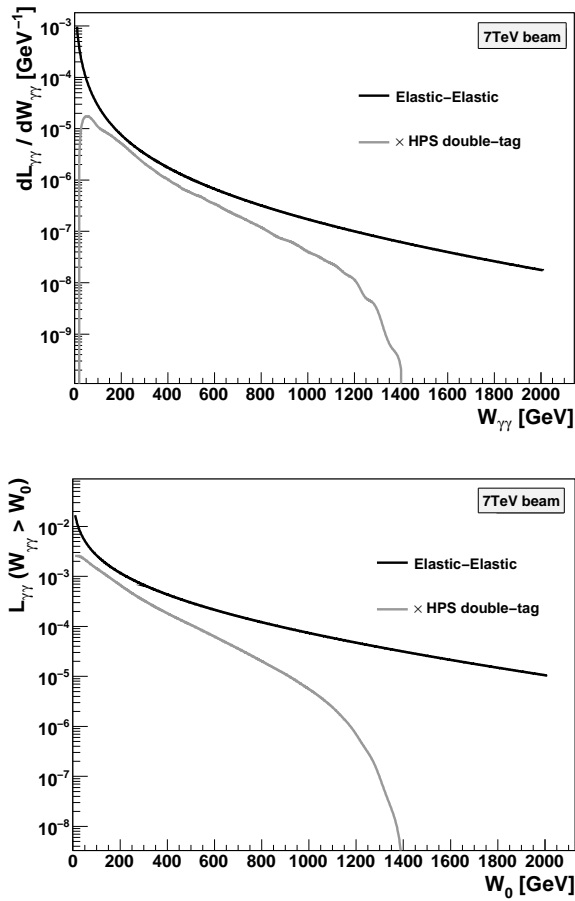


Figure 4.8: Relative (left) and integrated (right) photon-photon luminosity with HPS double-tag acceptance.

## 4.4 HPS background reduction

Since the processes of interest by the HPS project are on the femto-barn level, the detectors need to be able to run at the highest instantaneous luminosity, up to  $\mathcal{L} = 10^{34} \text{ cm}^{-2}\text{s}^{-1}$ . With the increased luminosity, the number of simultaneous interactions per bunch-crossing is raising too. Therefore, the probability to have fake triple coincidence event with one or two protons coming from parasitic interactions as shown in Figure 4.9 would be so high that it would dominate the signals.

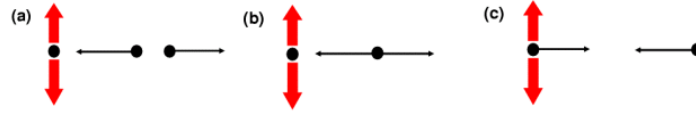


Figure 4.9: Schematic illustration of overlap backgrounds to exclusive production: (a)  $[p][X][p]$ : 3 interactions, one with a central system, and two with opposite direction single protons (b)  $[pp][X]$ : 2 interactions, one with a central system, and the second with two opposite direction protons (c)  $[p][pX]$ : 2 interactions, one with a central system and a proton, the second with a proton in the opposite direction, copied from [3].

In order to reduce this overlap background, one possible technique consists to request a strong matching between the vertex reconstructed by the central tracker of CMS and the point of origin of two scattered protons reconstructed with a  $z$ -by-timing method. One only needs to measure the relative arrival time of the two protons at forward stations,  $t_L$  and  $t_R$ . Assuming that the two protons are originating from the same interaction, the  $z$  position can be reconstructed as

$$z_{pp} = \frac{1}{2}(t_L - t_R) \times c \quad (4.2)$$

The resolution of the vertex position  $\delta z_{pp}$  is therefore only function of the timing resolution  $\delta t$  on single-side as  $\delta z_{pp} = \frac{c}{\sqrt{2}}\delta t$ . In order to achieve the precision resolution of 2 mm on the reconstructed  $pp$  vertex, one therefore needs a 10 ps time resolution on each measurement.

In case the two protons are not coming from the same interactions, the reconstructed vertex positions  $z_{pp}$  and  $z_{CMS}$  will not match in general, allowing a large rejection factor.

## Overlap events at the LHC

The rate of accidental triple coincidence background within the central and forward detectors is obviously function of the delivered instantaneous luminosity. Therefore, the overlap background will be computed for two benchmark luminosities corresponding to 'low' ( $\mathcal{L} = 2 \cdot 10^{33} \text{ cm}^{-2}\text{s}^{-1}$ ) and 'high' ( $\mathcal{L} = 10^{34} \text{ cm}^{-2}\text{s}^{-1}$ ) pileup regime at  $\sqrt{s} = 14 \text{ TeV}$ . The labelling convention to use square brackets to specify the interaction to which the proton belongs is used in the following. For instance, two single-diffractive events plus an prompt inclusive event will be noted by  $[p][X][p]$ , while two-photon production would be  $[pXp]$ .

The total cross-section prediction for  $\sqrt{s} = 14 \text{ TeV}$  from Pythia is around 100 mb and is composed of the following processes:

- Elastic production:  $pp \rightarrow pp$ , simulated with MSUB(91), is not contributing to the visible cross-section;
- Single diffraction:  $pp \rightarrow pX$  or  $pp \rightarrow Xp$ , simulated with MSUB(92) or MSUB(93), has a production cross-section of 14.3 mb;
- Double diffraction:  $pp \rightarrow X$ , simulated with MSUB(94), with a 10.21 mb cross-section value;
- Non-diffractive inelastic production:  $pp \rightarrow X$ , simulated with MSUB(95) and also sometimes called *low- $p_T$  production*, has the largest contribution with 54.71 mb.

The energy spectra of all charged particles with  $|\eta| > 7$  are displayed for each sub-process independently in Figures 4.10, with the same color code.

Only a small fraction of the produced particles will reach 240 m or 420 m locations, but enough to lead to significant concern at high luminosity.

The fraction of events with single and double tag is shown in Table 4.1 for each MinimumBias process independently. The cross-section for events at the LHC containing a forward particle detected in HPS is then clearly dominated by single-diffraction. Reweighting individual probabilities of Table 4.1, the probabilities of single and double tag per pileup event turn to be:

$$f_{[p]}^+ = 2.69\% \quad f_{[p]}^- = 2.78\% \quad f_{[pp]} = 0.05\% \quad (4.3)$$

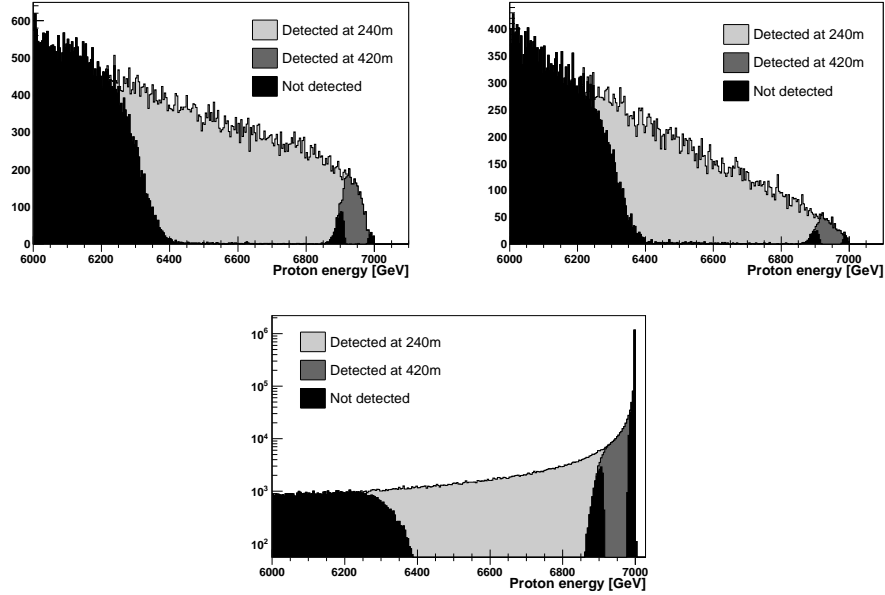


Figure 4.10: Zoom on forward particle spectrum, with HPS-240 and -420 acceptance, for MSUB(94) (top left), MSUB(95) (top right) and MSUB(92), MSUB(93) (bottom) processes.

with the single tag efficiency computed for both sides separately. It has to be noticed that not only protons are sources of overlap background. Although there are the main source (93.7%), one also expects some significant contributions from forward  $\pi^+$  (2.5%),  $\Sigma^+$  (2.2%) and  $K^+$  (1.8%).

Process	Single Tag only				Double Tag
	+240m	-240m	+420m	-240m	
$pp(\gamma\gamma) \rightarrow pW^+W^-p$	8.96%	6.00%	7.34%	8.45%	57.45%
Single diffraction (92)	1.03%	13.23%	0.07%	11.35%	0.25%
Single diffraction (93)	13.89%	1.14%	12.24%	0.07%	0.27%
Double diffraction (94)	1.42%	1.57%	0.09%	0.08%	0.02%
Non-diffractive Inelastic (95)	0.30%	0.34%	0.01%	0.01%	<0.01%

Table 4.1: Fraction of events with single/double tag for MinBias and signal.

The cross-section for overlap background may therefore be estimated as [84]:

$$\begin{aligned} \sigma_{olap} &= \sigma_{[X]} \left( \sum_{N=3}^{\infty} \frac{\lambda^N e^{-\lambda}}{N!} P_{[p][p]}(N-1) + \sum_{N=2}^{\infty} \frac{\lambda^N e^{-\lambda}}{N!} P_{[pp]}(N-1) \right) \\ &\quad + \sigma_{[pX]} \sum_{N=2}^{\infty} \frac{\lambda^N e^{-\lambda}}{N!} P_{[p]}(N-1) \end{aligned} \quad (4.4)$$

$$= \sigma_{[X]} (\mathcal{E}_{[p][p]} + \mathcal{E}_{[pp]}) + \sigma_{[pX]} \mathcal{E}_{[p]} \quad (4.5)$$

where  $\sigma_{[X]}$  is the inclusive cross section with the same final state  $X$  of interest,  $\lambda$  is the average number of  $pp$  interactions per bunch crossing and  $N$  is the actual number of interactions in the considered bunch crossing. The sum is performed over all possible number of interactions and weighted for each configuration by a Poisson distribution. In the first term,  $P_{[p][p]}(n)$  is the probability that, given  $n$  interactions, there are at least two events that produce a forward particle detected in HPS (one on each side), which is given by [84]:

$$P_{[p][p]}(n) = \sum_{r+q=2}^n \sum_{q=1}^{r+q-1} \frac{n!}{(n-[r+q])! r! q!} \left(f_{[p]}^+\right)^r \left(f_{[p]}^-\right)^q \left(1 - f_{[p]}^+ - f_{[p]}^-\right)^{n-r-q} \quad (4.6)$$

where, for example,  $f_{[p]}^+$  is the fraction of events that produce a forward particle within HPS-240 or HPS-420 acceptance from equation 4.3.

In the second term,  $P_{[pp]}(n)$  is the probability that there is at least one event that contains an HPS hit on each side of the IP, and is distributed as a binomial distribution:

$$P_{[pp]}(n) = \sum_{q=1}^n \frac{n!}{(n-q)! q!} \left(f_{[pp]}\right)^q \left(1 - f_{[pp]}\right)^{n-q} \quad (4.7)$$

Finally, the third term stands for the coincidence probability between an overlap event and a single-diffractive event  $pp \rightarrow pX$  which produce the same final state of interest plus a HPS hit.  $P_{[p]}(n)$  is therefore defined as the probability that there is at least one event with a forward particle detected on the opposite side of the IP to the single diffractive proton from the hard event. The corresponding formula is similar to  $P_{[pp]}(n)$  but using the event fraction  $f_{[p]}$ .

The Poisson mean number of interactions  $\lambda = 5.03$  for the "low-luminosity" period, and  $\lambda = 25.14$  for the "high-luminosity" periods, correspond respectively to  $\mathcal{L} = 2 \times 10^{33} \text{ cm}^{-2}\text{s}^{-1}$  and  $\mathcal{L} = 1 \times 10^{34} \text{ cm}^{-2}\text{s}^{-1}$  if one considers a 40 MHz frequency,

the nominal number of 2808 proton bunches in the pipe and a total visible cross-section of 79.22 mb. Therefore, the computation of integrated probabilities gives:

$$\begin{aligned}\mathcal{E}_{[p][p]} &= 1.12\% \text{ for low lumi} \\ &= 23.36\% \text{ for high lumi}\end{aligned}\tag{4.8}$$

$$\begin{aligned}\mathcal{E}_{[pp]} &= 0.20\% \text{ for low lumi} \\ &= 1.23\% \text{ for high lumi}\end{aligned}\tag{4.9}$$

At leading order, that means that in high-pileup conditions roughly 25% of the beam crossings will produce a fake double-tagged event. In the next studies, the low probability due to  $[pX][p]$  has been neglected.

For similar computations assuming only forward stations at HPS-240 as it will be the case for the first stage of the HPS project, one finds a probability of accidental double-tag events of 0.6% and 12.4% for 'low' and 'high' luminosity conditions respectively.

### Accidental coincidence reduction

Although one bunch crossing over four will produce accidental forward coincidence at high luminosity, such kind of background can be reduced by several techniques. As the overlap events are uncorrelated, one can request kinematics consistency between central and forward detectors. Also, as final state of interest is usually produced in association with many tracks attached to the prompt vertex, on contrary to the two-photon interactions where the pair is produced exclusively, a constraint on the number of neighbored tracks will already suppress accidental coincidence background to an acceptable level.

The third technique uses the comparison of the central and forward vertex positions, the latter ones being built with the proton time of arrival at the very forward stations. The rejection factor will depend on the following parameters, discussed afterwards:

- intrinsic timing resolution  $\delta t$ ,
- longitudinal spread of the interaction points  $\sigma_z$ ,
- vertex size window,
- difference in path length between left and right sides

The main source of degradation in the timing resolution is mainly due to the intrinsic jitter of the Photo-Multiplier tubes (PMT) used to detect the Cerenkov photons. Currently, a time resolution of 10 ps was achieved in laboratory (testing PMT only) and in test beam conditions (including signal amplification and oscilloscope processing) with Photek-brand tubes.

The other important factor influencing the rejection is the longitudinal spread of the vertices positions: broader the distribution, lower the probability to have accidental triple coincidence with matched vertices. The spatial and time distributions of the current densities, as well as the crossing angle have influence on the spread value. The full computation of the luminosity profile along  $z$  integrated over time and taking into account all LHC machine parameters for the nominal design as the half-crossing angle of  $142.5 \mu\text{rad}$  has been done in [85] and result in  $\sigma_z = 48.2 \text{ mm}$ . For protons not com-

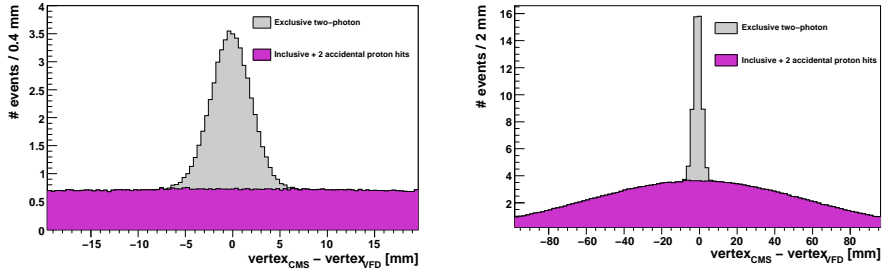


Figure 4.11: Simulation of the distance between reconstructed vertices for signal ([pXp]) and overlap ([p][X][p]) events, taking into account a vertex spread of  $\sigma_z = 48.2 \text{ mm}$  and a timing resolution of 10 ps.

ing from the same interaction, the distance between the "false" vertex reconstructed in the forward station  $z_{VFD}$  and any prompt vertex in the central detector  $z_{CMS}$  will be reconstructed on average as a Gaussian with  $\sigma = \sqrt{1.5} \sigma_z \simeq 59 \text{ mm}$ , as represented in Figure 4.11.

The vertex size window is the degree to which we require the reconstructed  $pp$  vertex to match with the central vertex. As it is clearly analysis-dependent, the value should be balanced between a small (higher background rejection) and a large (higher signal selection) vertex size. For the study of two-photon production of supersymmetric pairs in Chapter 8, the highest value of  $S/\sqrt{B}$  was obtained for a window of  $1.5\sigma$ , *i.e.* selecting 87% of the signal events. The efficiency selections for a  $1.5\sigma$  vertices

matching, for the signal and the overlap events, are displayed on the table next page assuming different timing resolutions.

Process type	$\delta t = 5\text{ps}$	$\delta t = 10\text{ps}$	$\delta t = 20\text{ps}$
[pXp]	87%	87%	87%
[p][X][p]	2.13%	4.26%	8.49%
[pp][X]	1.84%	3.68%	7.36%

Table 4.2: Forward and central vertices matching efficiencies for different timing resolutions. The  $1.5\sigma$  window size is set here.

Finally, as it can be seen from the Figures 4.12 computed with HECTOR, the difference between left and right side is at most  $8\ \mu\text{m}$  which leads to a negligible contribution to the time jitter of around  $2.5 \times 10^{-2}$  ps.

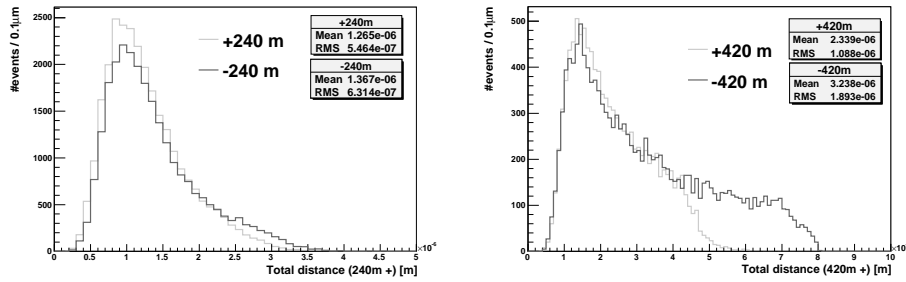


Figure 4.12: Total path length for 2-HPS hits protons.

## 4.5 Gastof as a fast timing detector

### 4.5.1 GASTOF detector overview

The concept of a dedicated timing detector for the HPS experiment needs to take the following requirements into account:

- the full system timing resolution should be  $\mathcal{O}(10\text{ ps})$  for measurement of single proton time of arrival,

- the sensitive detectors have to survive at the rate of scattered forward (signal and background) particles,
- the complete setup has to disturb as less as possible kinematics of the proton candidates

To fulfill them, the design involves detection of Cerenkov light produced by the passage of forward scattered particles within a gas volume [86]. The gas is contained in a rectangular box of few 10s cm length with a very thin wall adjacent to the beamline and aligned on the parallel with the scattered proton propagation axis, as shown in Figures 4.13 for a  $\sim 35$  cm long GASTOF . The use of gas medium as a radiator has the advantage to create fast light pulses, with well predicted kinematics.

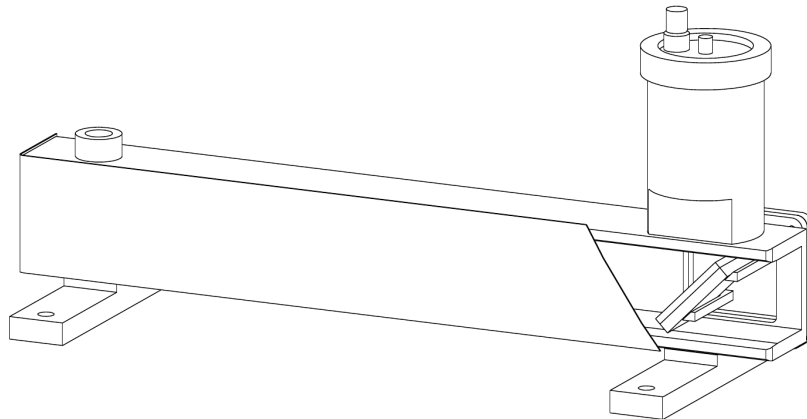


Figure 4.13: 3D view of Gastof detector, for the 30 cm-long version.

The proposed gas, already in use in the prototypes, is the  $C_4F_{10}$  at a relative pressure of  $\sim 1.2$  bars which has a reflective index  $n = 1.0014$  and thus produces light cone with a narrow angle of  $3^\circ$  in the  $[200, 650]$  nm wavelength range. Produced photons are then reflected by a thin metallic front-surface mirror on a fast Photo-Multiplier Tube (PMT), placed out of the protons trajectory. The mirror has a special aluminium coating with a magnesium fluoride overcoat which protects the aluminium and enhances the reflectivity for short wavelengths. It has a spherical shape with radius of 10 cm which slightly focuses reflected photons. Mirror is aligned such that the symmetry axis of the box is projected on the center of the photo-cathode surface, as drawn in Figure 4.14, and event displays from Figures 4.15. Usage of a lens to further focus

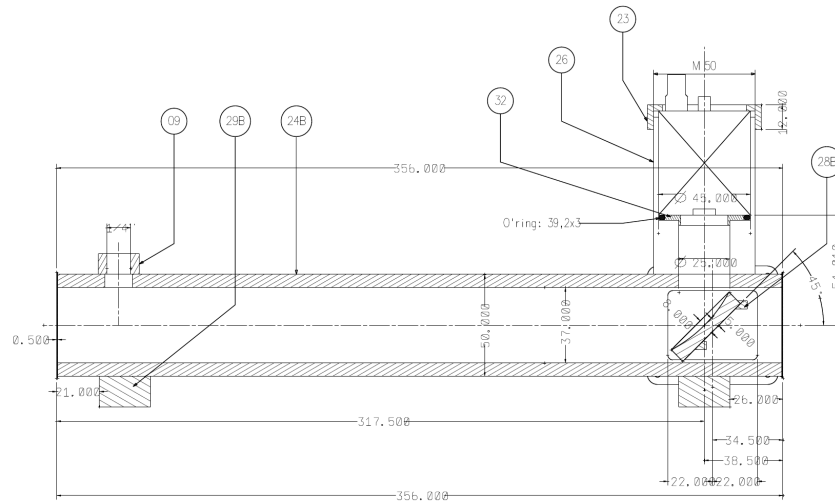


Figure 4.14: 2D view of Gastof detector, with technical distances, for the 30 cm-long version.

is also in consideration for future upgrades.

In the reference design, the main source of timing resolution degradation is coming from the transit time spread in the PMT, *i.e.* difference of time distribution between photon impinges the photo-cathode and current collection on the anode. Indeed, for a 15 cm length GASTOF, the Cerenkov light production should last only 2 ps, and photons would travel at speed close to  $c$  in gas; such that the spread of time of arrival of photons on the photo-cathode is limited to 1.5 ps, as shown with simulation in Figure 4.19.

The photo-multiplier tubes used for last GASTOF detectors are the Micro-Channel Plates PMT (MCP-PMT). These are special PMT consisting of a 2D array of parallel glass capillarities of a few  $\mu\text{m}$  diameter, called channel. Each channel, of which inner wall is covered by material with secondary electron properties, works as an independent electron multiplier. The MCP-PMTs are well suited for fast timing measurements as a strong electric field is applied parallel from the photo-cathode to the MCP entrance and from the MCP exit to the anode. Thanks to this strong field, effects of emission-angle distribution and initial-velocity distribution of photo-electrons, which usually have tendency to broaden the signal pulse, are avoided.

The other type of timing detector QUARTIC (QUARtZ TIming Cerenkov) is using a different technology. Instead of gas, it has fused silica bars as Cerenkov radiators, oriented with respect to the beam line at the average Cerenkov angle ( $48^\circ$ ) aiming to minimize the light reflections into the bars. These 4 bars (in  $x - z$  plane) are then coupled to traditional MCP-PMT. The main advantage of QUARTIC is its possibility to measure the time of arrival of several protons per bunch, thanks to its  $x$ -segmentation.

A pair of QUARTICs will be inserted, in their own pocket, at the very back of the HPS station as they may disturb the proton trajectories with multiple scattering. On the contrary, the amount of material that has to travel scattered protons into GASTOF is relatively small (a thin front aluminium layer, the thickness of the mirror, and the back thin aluminium layer) and therefore detectors are expected to be placed among silicon tracking stations.

## 4.6 Ray tracing simulation

### Work done in collaboration with Tomasz Pierzchala

The simulations of forward scattered proton interactions with the detector, the Cerenkov rays development and the signal emission out of the PMT deserve two aims. On the one hand, for its prediction on the average number of photons or photo-electrons collected in GASTOF for typical events, as the resolution of time measurement is supposed to be directly related to the number of detected photons. On the other hand, it can become a powerful tool to search for the best design with specific constraints.

Next studies concentrate on the derivation of GASTOF properties considering first a reference prototype and then some variations in the design. Most of technical figures as reflectance, refraction index, . . . are placed in the Appendix B.

#### 4.6.1 Software details

As the geometry (a rectangular box with a circular output) and the physics (Cerenkov effect) of the proton interaction are quite simple, the simulation software was developed in C++ language, rather than using heavy full simulation software like GEANT. The concept is therefore based on linear geometry and transmission/reflection efficiency dependence with the energy. The simulation, from proton incoming into GASTOF up to signal pulse out of the PMT, is stepped in different parts detailed in the next:

1. **Photon generation:** Cerenkov light is generated along the proton path in the gas volume;
2. **Photon propagation:** each light ray is propagated individually into the volume, interacting with walls, mirror, lens, etc. up to the exit window of GASTOF;
3. **Photon detection:** surviving photons are collected on the photo-cathode and output signal pulse is simulated;

For the next figures, a realistic distribution of proton  $x$  and  $y$  entrance positions in GASTOF has been assumed as in HPS-240 –as illustrated in Figure B.1– with the detector aligned parallel to the proton direction. Otherwise explicitly quoted, the following geometric and physical assumptions have been set for the reference detector:

- GASTOF lateral position is at 2.5 mm for the LHC beamline, such that  $x = 0$  in the plots corresponds to  $x_{LHC} = 2.5$  mm;
- horizontal ( $x$ ) and vertical ( $y$ ) widths are 30 and 37 mm-long respectively,  $z$  length is 16 cm from indoor face to the exit window center;
- mirror has a spherical shape of 10 cm radius and it covers  $0 < x < 30$  mm and  $6 < y < 37$  mm; its reflection efficiency is assumed as shown in Figure B.3;
- gas is  $C_4F_{10}$  at a pressure of 1.3 bars;
- a circular exit window of 12.5 mm radius, centered on mirror focus point;
- PMT is the R3809U-50 from Hamamatsu with Quantum Efficiency (QE) as in Figure B.6 and Collection Efficiency (CE) of 25%;
- reflection of the thin wall close to beam is set to 20%, while other walls are considered as black;

Basic geometry as it is implemented in the software and seen by the Frog event display [87] is shown in Figure 4.15.

### Cerenkov photon generation

Photons are created along the whole path of the proton within the gas volume. In order to optimize the event simulation CPU, it was decided to attach a weight to each generated photon rather than simulate a large sample and count the surviving ones. The initial weight associated to each produced photon corresponds to the probability

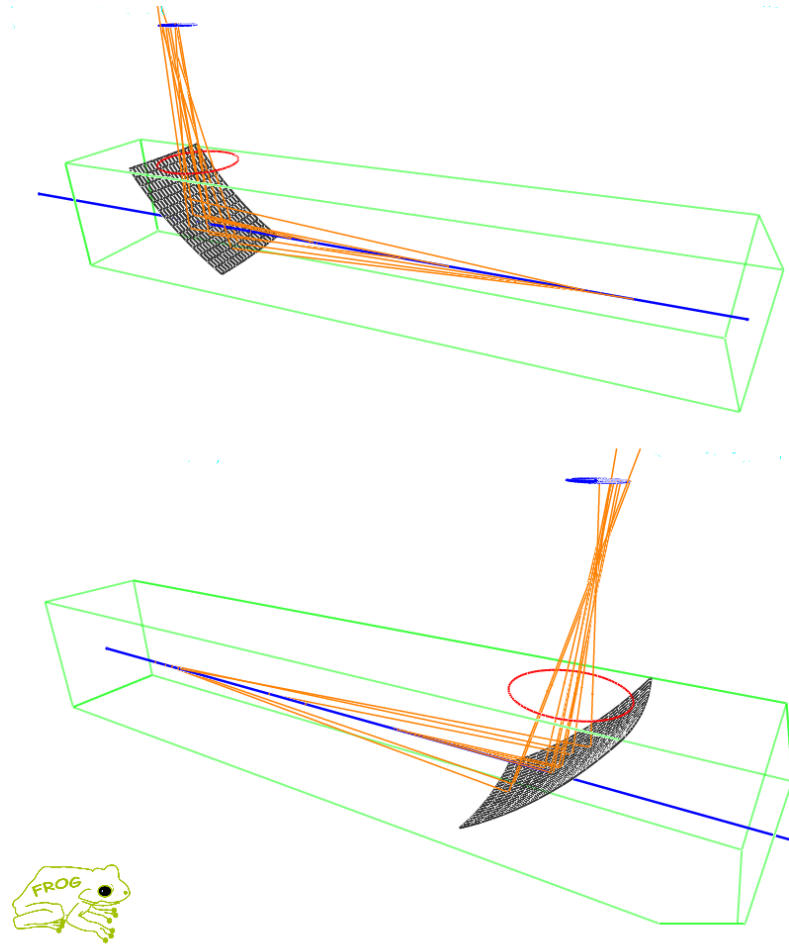


Figure 4.15: Event display of the implemented geometry and a typical event in GASTOF. The gas is contained within the box (green lines) which is fully hermetic but at the exit window (red circle), where rays can exit and touch the photo-cathode (blue disc). Proton (blue line) and photons (orange lines) paths are displayed for a typical event.

of Cerenkov photon emission with a typical energy, normalised by the total number of photons emitted along the path length. This total number is fixed per trajectory and easily computed as:

$$\begin{aligned}
 dN &= \frac{\alpha}{hc} dz dE \sin^2(\theta) \\
 &= \frac{\alpha}{hc} dz dE \left( 1 - \frac{1}{\beta^2 n^2} \right)
 \end{aligned}
 \tag{4.10}$$

with  $dz$  the total path length of the proton in the gas, and  $dE$  the energy distribution. In the simulation process, the photon wavelengths are generated only from 160 to 900 nm, as light produced outside this range would not be reflected by the mirror and/or detected by the PMT.

Rays are generated at the Cerenkov angle of  $\sim 3^\circ$  since refractive index, which is a function of the incoming energy, varies between 1.0013 and 1.0017 in the energy regime we are restricted as displayed in Figure B.2. The  $\phi$  angle is chosen randomly among  $[0, 2\pi]$ .

### Cerenkov photon propagation

Light rays are propagated into the volume, starting from their generation position on the proton path, at the group velocity roughly equivalent to  $1/n$ . Photons propagate freely following a straight line until they reach a surface. At each surface crossing, the direction and the weight of the photon are modified, with actions depending on the encountered material:

- black wall: photon is absorbed by the wall, so the weight associated to ray is set to zero;
- aluminium wall: photon weight is multiplied by the assumed aluminium reflectance (20% in the examples below), and the direction is modified as for a reflection by a flat surface;
- mirror: photon weight is multiplied by the mirror reflectance, which is a function of the photon energy (see Figure B.3), and the direction is modified as for a reflection by a hemisphere;

In addition, timing information is updated at each surface crossing.

### Cerenkov photon detection

If the Cerenkov ray reaches the exit window of GASTOF detector with a non-null weight, its trajectory is continued outside the rectangular box towards the PMT. The sensitive area of the photo-multiplier, the photo-cathode, is simulated by a disk of 5.5 mm radius. Prior the collection by the photo-cathode, photons have to travel a quartz layer of 3.2 mm width which is meant to protect the cathode itself. As the reflective index of quartz (from 1.54 to 1.82 for the wavelengths under consideration) is different from the gas, the trajectory of the photon into quartz will be slightly modified

with respect to the initial direction. The modification of the photon path length into the quartz is somehow very limited and increases the time-of-flight by 6.5 ps on average for the total length. On the contrary, the velocity in quartz being different from the velocity in the gas, the propagation of the photon into  $\frac{3.2 \text{ mm}}{\cos\theta}$  of quartz leads to an increase of 0.2 ps for the time of arrival on the photo-cathode of different photons from the same proton. As an example, the distribution of the time of arrival with and without quartz window for the reference setup is shown in Figure 4.19.

The weight of each collected photon by the photo-cathode is then multiplied by the Quantum Efficiency (QE) and Collection Efficiency (CE) of the PMT under consideration in order to simulate the generation of photo-electrons. For the Hamamatsu tubes that were tested so far, the QEs dependence with the input wavelength are displayed in Figure B.6, derived from the photo-cathode sensitivity also shown in the same Figure. The CE, for which value remains unknown, was fixed to 25% as the best value to fit 2009 Test Beam data.

After computing the probability of such a  $N(\text{photon})$  to  $N(\text{photo-electron})$  transformation, simulation of the signal pulse height is performed as a convolution of  $N$  single-photon response curves as Figure B.7, with  $N$  a random number from Poisson distribution with mean of expected photo-electrons.

#### 4.6.2 Reference design predictions

The distribution of the photon hit positions on the photo-cathode from a realistic sample of  $pp(\gamma\gamma) \rightarrow pW^+W^-p$  events at HPS-240 is displayed in Figure 4.16 (right) where two zones with higher density can be observed. There are both due to the high density of protons hitting the front surface of GASTOF detector at  $x \simeq 3$  mm, observed in Figure B.1. The highest zone collects photon emitted in the direction of the detector center and photons reflected by the aluminium wall. The other zone, less dense, is due to the Cerenkov photons emitted in the direction of the beam-wall, but not enough to hit it before reaching the spherical mirror.

For comparison, the same hits distribution for entrance points distributed uniformly horizontally and fixed to mid-height vertically is shown on the same Figure. The distribution is rather uniform but two same zones due to the spherical mirror configuration.

The response of the detector as a function of the incoming proton position is studied in Figure 4.17. Protons are generated with fixed  $y$  position at the middle of the detector

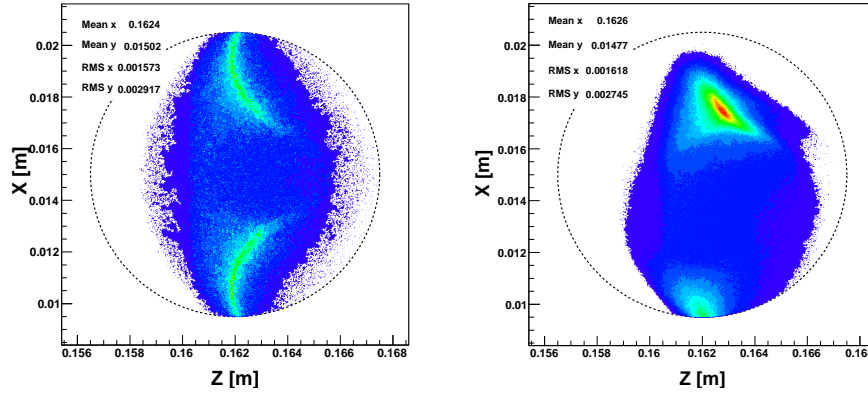


Figure 4.16: Two-dimensional distribution of the photon hit positions on the photo-cathode for horizontally uniformly distributed proton entrance points (left) and for realistic HPS-240 case (right) and reference design.

(indeed,  $y$  dispersion of scattered proton in forward detector is very limited), and  $x$  positions uniformly distributed among the full range of GASTOF acceptance. One can

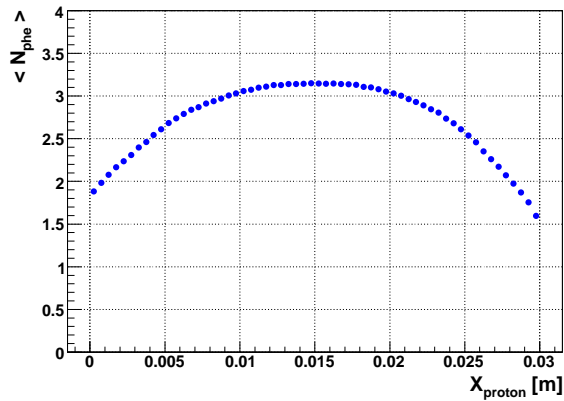


Figure 4.17: Mean number of produced photo-electrons in the reference design as a function of the horizontal proton entrance position  $X_{\text{proton}}$ , and vertical position  $Y$  fixed to the mid-height ( $Y=16.5$  cm). The maximal signal is expected for  $X_{\text{proton}}$  in the middle of the detector, and efficiency decrease is observed when  $X_{\text{proton}}$  approaches a wall as (part of) the Cerenkov light is absorbed.

clearly notice the slight decrease of the mean signal for horizontal entrance position moving away from the center, as part of the Cerenkov emission will be (highly or

fully) absorbed by the wall material. Compared to protons emitted on the detector symmetry axis, protons with initial position close to the beam wall produce a 40% smaller signal if the reflectance of the aluminium wall is set to 20%, or even 50% if it is assumed fully black as the opposite-beam wall. It is worth to note that the efficiency never drops to 0% on average anyway, thanks to the geometric distribution of the Cerenkov rays as a cone.

The spectrum of these detected photons is actually shown in Figure 4.18. Starting from the pure spectrum of emitted Cerenkov rays, the effects of the collection and photo-electron transformation are visible. For the photo-electron curve, the wavelength is the one from the original photon. At the end of the process, the spectrum of photons contributing to the signal is peaked for wavelengths around 250 nm, mainly due to the higher PMT quantum efficiency in this region.

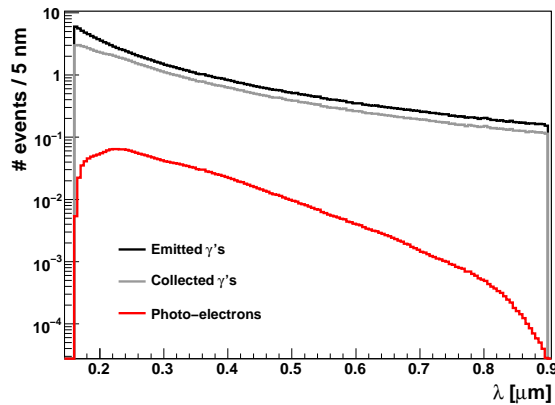


Figure 4.18: Spectrum of the produced Cerenkov photons, collected photons and photo-electrons as a function of the  $\gamma$  wavelength, for realistic HPS-240 case and the reference design. For the photo-electrons, the wavelength corresponds to the one of the initial photon.

One of the most important quantity (with the efficiencies dependence) that could be derived from the simulation, is the photon time of arrival on the photo-cathode. Indeed, the time spread of the hits on the PMT will contribute to the timing resolution itself. For the  $\sim 15$  cm long GASTOF, the RMS of the time distribution is only 1.5 ps as it is shown in Figure 4.19, on which effect of the 3.2 mm quartz window is also visible.

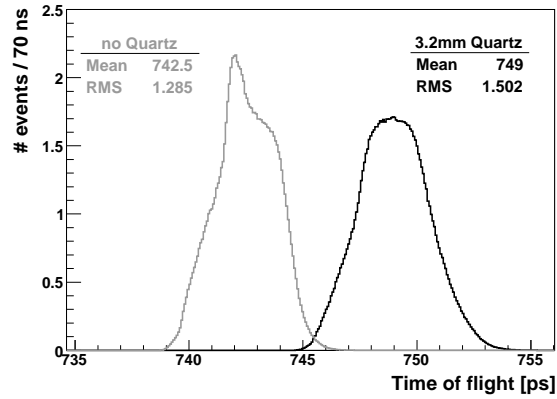


Figure 4.19: Time of arrival of photons on the photo-cathode for realistic HPS-240 case and the reference design. The effect of the 3.2 mm quartz window placed front the photo-cathode is emphasized by plotting the non-realistic case without such quartz layer.

### 4.6.3 Design variation

The same simulation package may also be used to search for the best design by the optimization of the detection efficiency and the time spread. Various modifications are under study, and few of them are addressed in the following. All the parameters set for the reference design are fixed, but the one under consideration.

#### Length influence

The total length of the GASTOF detector, and hence the path length of the proton inside the gas volume, has an influence on the timing measurement. Indeed, longer GASTOF implies more Cerenkov photons created, but also larger time spread of the photo-cathode hits. The effect is shown in the table below for different lengths computed as the distance from the front face to the mirror. The realistic benchmark simulation at HPS-240 has been assumed.

Length	$N_{phe^-}$	Mean Time	RMS Time
0.162 m	$2.56 \pm 0.01$	749 ps	1.41 ps
0.2 m	$2.94 \pm 0.01$	876 ps	1.46 ps
0.25 m	$3.28 \pm 0.01$	1043 ps	1.51 ps
0.3 m	$3.51 \pm 0.01$	1210 ps	1.60 ps
0.35 m	$3.65 \pm 0.01$	1377 ps	1.66 ps

As an example, roughly doubling the total length of the detector (16.2 to 30 mm), the number of photo-electrons increases by  $\sim 35\%$  for only a 0.2 ps extra contribution to the RMS.

## Pressure

Pressure inside the box has two effects on the physical process as the gas refractive index is a function of the pressure:

$$n(p) = \sqrt{1 + p (n^2(1) - 1)} \quad (4.11)$$

with  $p$  the pressure expressed in units of atmosphere. Therefore, increased pressure implies a larger refractive index and hence a larger Cerenkov angle of emission. In addition, from equation 4.10, increased index also means that more Cerenkov photons are emitted. The variation of the mean number of photo-electrons for realistic HPS-240 case is plotted in Figure 4.20.

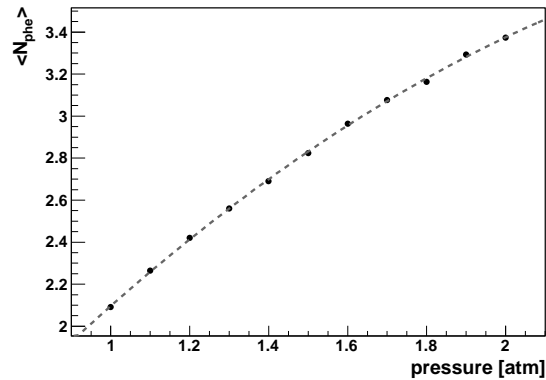


Figure 4.20: Mean number of produced photo-electrons as a function of the gas pressure into the GASTOF volume for realistic HPS-240 case.

It is by consequence planned to use the adjustment of the pressure to compensate the decrease of the quantum efficiency because of the ageing issue.

## Reflective wall

One of the major loss of signal comes from protons which are entering close to the wall into GASTOF, and for which roughly half of the Cerenkov light is emitted into the di-

rection of this wall. For the nominal simulation case, a fixed value of 20% reflectance has been set for the wall closest to the beamline, and one can see in Figure 4.21 that the efficiency decreases for proton incoming position closer to beam-wall.

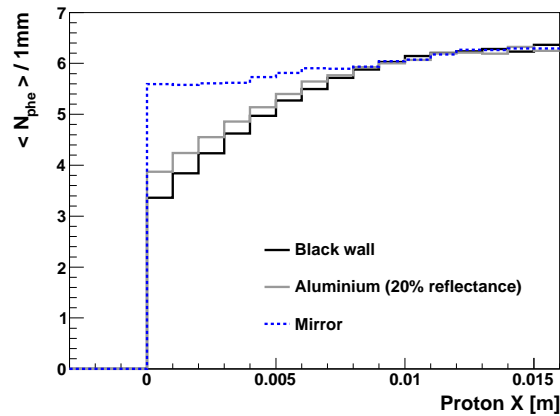


Figure 4.21: Mean number of produced photo-electrons for realistic HPS-240 case and for different beam wall material.

For the final design, it is therefore planned to build it with high-reflectance material. To show the effect of such improvement, the beam wall has been assumed to have the same reflective properties as the mirror with the reflectance plotted in Figure B.3; one notices that for the same sample of realistic protons, the insertion of the mirror tends to uniform the signal efficiency over  $x$ .

## Lens

Finally, the last upgrade possibility that has been cross-checked with the simulation software is the insertion of a lens between the exit window and the photo-cathode, and aiming to focus the photons on the sensitive area of the PMT. A realistic commercial lens with transmission properties of Figure B.4 has been assumed for the simulation. The Figure 4.22 shows the effect of the lens on the position of photon hits on the photo-cathode where, the  $2D$  distance with respect to the area center is used. With the usage of the lens, the whole reflected photons by the mirror are collected by the PMT, while without focusing part of them were missed.

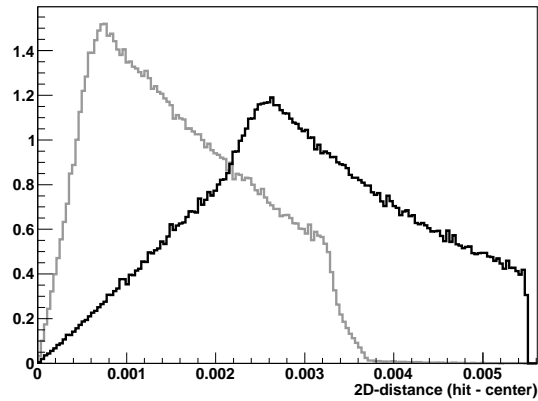


Figure 4.22: Distribution of the detected Cerenkov hit distance to the photo-cathode center, for realistic HPS-240 case, without (black line) and with (gray line) lens inserted after the exit window.

## Summary

The simulation of proton interaction within the GASTOF detector, although it was built with generic C++ classes simply based on linear geometry, showed to give valuable predictions for the search of the final design. In particular, it predicts no region without signal visibility.

In addition, the insertion of a lens and the increase reflectance of the wall close to the beam are two possible options to improve the design: the first to increase the signal collection on the photo-cathode, the second to increase the signal for near-to-wall incoming protons.





## **Part III**

# **The measurements**



## Chapter 5

# Selection of the exclusive processes at the LHC

*“L’heure n’est pas aux exclusives”*

J. Milquet, Belgian politician

*“Il faut éviter les exclusives”*

D. Bacquelaine, Belgian politician

*“Il n’y a pas d’exclusive”*

J.M. Javaux, Belgian politician

*“Marre de toutes ces histoires d’exclusive”*

C. Gennez, Belgian politician

With single-interactions, the exclusive signal from two-photon interactions in the central CMS detector would be characterized by the presence of the prompt scatter, no additional tracks, and no activity above threshold in the calorimeters. The presence of pileup events with exclusive signal event will however spoil this picture by producing additional tracks and energy deposits in the calorimeters. The exclusivity conditions are therefore applied using the pixel and silicon tracker only, as the accurate track and primary vertex reconstructions allow discrimination between different interactions within the same bunch-crossing.

The principle for tagging (5.1), and the commissioning of the exclusivity conditions with the calorimetry (5.2) and the tracking system (5.3) are subjects of this chapter.

## 5.1 Tagging exclusive processes at the LHC

The detection of two-photon interactions is simplified by the simple topology of the final states. As illustrated in Figure 2.1, it is composed of the photons fusion result  $X$  produced exclusively, and two forward protons. Without forward proton detectors available in 2010 runs, the selection of exclusive processes –produced in  $\gamma\gamma$ ,  $\gamma\mathbb{P}$  and CEP– has to be achieved with the central system of the CMS detector only.

The experimental features of exclusive processes are completely uncommon to  $pp$  interactions driven by QCD-type of physics: many other tracks produced in association with the central hard scatter of interest, and large forward energy deposit due to proton remnants hadronisation after the interaction.

It is then *a priori* easy to select exclusive interactions among events from  $pp$  collisions by imposing exclusivity of the pair in the detector. Using the high-level objects available out of the reconstruction (Section 3.5), that would demand no other extra tracks in tracker plus no calorimeter tower with a significant energy above the noise level.

This definition of the exclusivity conditions would however be inefficient to select exclusive processes produced at the LHC, due to collider and detector concepts. On the one hand, though the CMS detector has a large coverage of the forward region thanks to HF, CASTOR and ZDC calorimeters, the main source of background faking exclusive events arises from inelastic photon exchanges as these processes produce particles at forward angles which escape outside the CMS coverage. The effect is visible in Figure 5.1 showing the energy- $|\eta|$  distribution of the most central particle in the proton remnant.

On the second hand, the instantaneous luminosity delivered by the LHC in 2010 went up to  $0.7 \mu\text{b}^{-1}\text{s}^{-1}$  (for non-certified periods it even reached  $205 \mu\text{b}^{-1}\text{s}^{-1}$ ), leading to multiple interactions occurring simultaneously within the same bunch crossing, and making it unusable information from the calorimetric towers to veto the inclusive interactions. At the TEVATRON, the CDF collaboration had to face the same issue and therefore decided to restrict the analysis to single-interaction events only. This was made possible by looking at end-of-run events, where the protons population per bunch is significantly lower than at the beginning of the spill life, and therefore the probability of overlap events. At the LHC in the 2010 data, less than 20% of the total luminosity was estimated to have been collected with single-interactions, leading to a significant decrease of the available statistics if the full calorimeter veto is used. In addition, the selection efficiency of exclusive sample could be strongly affected by

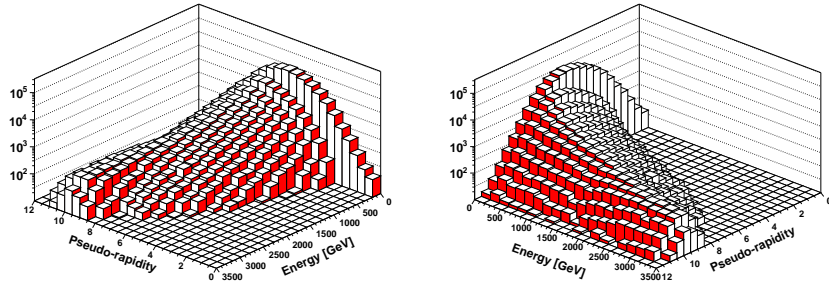


Figure 5.1: Pseudo-rapidity ( $\eta$ ) distribution of the most central particles produced in the proton fragmentation after inelastic photon emission. The events are simulated with LPAIR interfaced with JetSet and  $E_p = 3.5$  TeV,  $1.07 < m_N < 320$  GeV.

'invisible pileup', *i.e.* high-mass diffractive events which deposit large energy in the forward calorimeters but produce no signal in tracking system.

Instead, the track-based exclusivity conditions are successfully used to select exclusive events in the harsh environment of overlap events, with a high inefficiency to select fake inclusive events. The method consists in the rejection of all events with any additional tracks associated to the primary hard scatter. The efficiency of the technique is discussed in Section 5.3.

Finally, the optimal technique to tag exclusive events would consist in the installation of dedicated detectors located far from the IP and aiming to select events with small-angle scattered protons. With the capability to tag such protons, both inclusive and inelastic photon-exchanged events would be at a high level of rejection.

## 5.2 Calorimetry-based exclusivity conditions

The "ZeroBias" data are triggered by beam bunch crossing, *i.e.* for signals with coincidence between BPTX+ and BPTX- [88]. Since selecting all possible ZeroBias events would use valuable bandwidth for the detectors read-out, only a fraction of them, with a maximal frequency of 20 Hz, are recorded. Within the CMS collaboration, ZeroBias data are used to study detector behavior in non-colliding beam crossing conditions for jet energy background, beam-beam effects, etc. To our purpose, it will be used to

monitor the mean noise level of each sub-detector with time.

The energy threshold for noise rejection is computed on a 99% noise rejection basis, independently for each sub-group of CaloTowers of HF+ and HF-, as there are the most forward sub-detectors and hence the most sensitive to the forward component of the produced final state.

The 99% noise thresholds are checked with two different beam conditions:

1. events with BPTX+ – BPTX- in coincidence and no valid tracks<sup>1</sup> (blue);
2. events with exclusively BPTX+ or BPTX-, *i.e.* unpaired bunch crossing (black).

In addition, the maximal energy deposit due to real collisions events, *i.e.* coincidence of BPTX+ – BPTX- and at least two tracks (red), is also displayed in Figures 5.2. The leading calotower energies are displayed for two different beam conditions: on the left plots for Runs between 132440 and 139975 where the instantaneous luminosity reaches a maximum of  $0.32 \mu^{-1}\text{s}^{-1}$  (mean number of offline reconstructed primary vertices is 0.08); and on the right plot for Runs in 148819 to 149294 with maximum

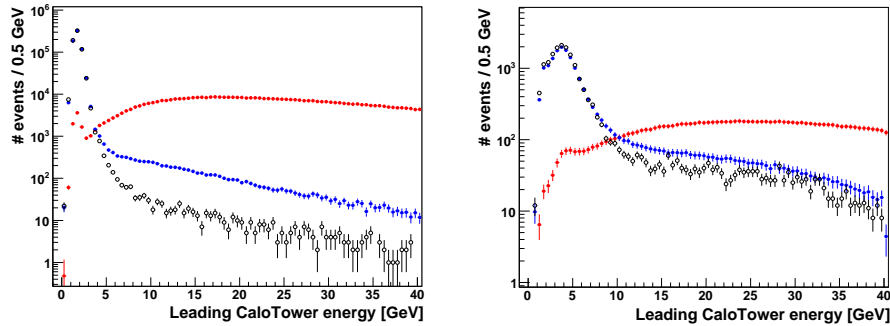


Figure 5.2: Leading calotower energy for low pileup (left) and high pileup (right) conditions. Distributions are normalized to the same number of events between unpaired BX (black), paired BX without tracker activity (blue) and paired BX with tracker activity (red).

of  $0.71 \mu^{-1}\text{s}^{-1}$  (mean vertex multiplicity is 1.83). For barrel and endcap sub-regions (not displayed here), calotower noises in paired and unpaired bunch-crossings are behaving similarly, which proves that beam backgrounds were not relevant during the commissioning phase for central detectors. On the contrary, one can notice a large

<sup>1</sup>A track is considered as valid if flagged as `HighPurity` track and  $|z| < 24$  cm.

discrepancy in the HF histograms, due to the fact the high-mass diffractive events may lead to non-activity in the central tracker but may deposit some energy in the forward region. This effect is visible in Figure 5.2 (black vs. blue), and one usually refers to it as "invisible pileup" effect since it is not seen by the tracking system.

To avoid this effect, only low-statistics but purer unpaired bunch crossing events are used to compute the noise rejection levels. The noise value for the first runs is shown in Figure 5.3 for HF+ and HF- only. Starting from an initial value of 4.1 GeV for HF+ and 3.3 GeV for HF-, one can notice a slight increase of the noise threshold in both sides of the calorimeters. Various sources are at the origin of this noise in-

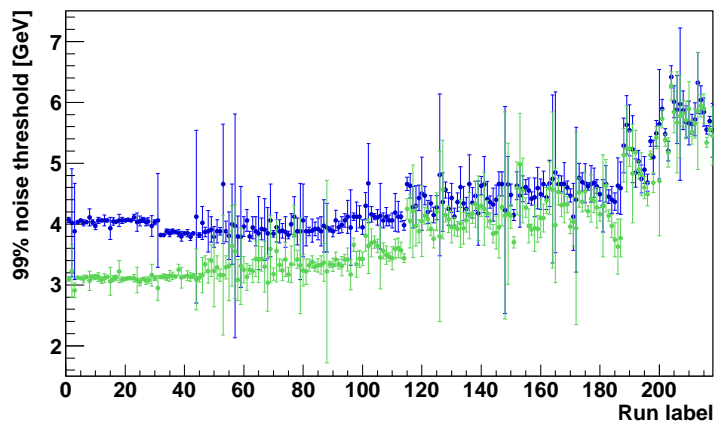


Figure 5.3: 99% noise threshold for HF+ (blue) and HF- (green) over the time (one point per run number), from Run 132440 to 144114. Only selected runs with significant statistics of unpaired bunch are used.

crease. First of all, with increased number of bunches per fill, the number of parasitic collisions grows. These are interactions happening outside CMS and for which fluxes of produced particles are coming "delayed" to CMS. For later runs not displayed here, the LHC encountered a problem of vacuum leak which led to a large increase of beam halos and pushed the 99% noise threshold of HFs to as high value as 35 GeV with the computation method used.

The efficiency of selecting exclusive interactions with calorimeter-veto, is then strongly affected by the increase of instantaneous delivered luminosity by the LHC. In order to prove once more the futility of the method, the Figure 5.4 shows the efficiency of

selecting, among coincident BPTX ZeroBias events, 'empty' event by asking for less than 5 CaloTowers with an energy above the noise as computed in the commissioning period. The efficiency drops below 50% already after  $L = 0.2 \mu^{-1}\text{s}^{-1}$ .

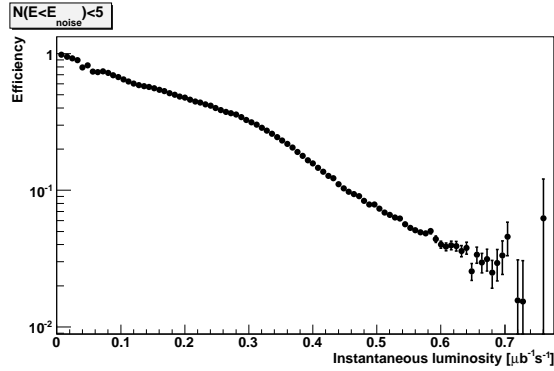


Figure 5.4: Calorimeter exclusivity ( $N_{E > E_{noise}} < 5$ ) efficiency vs. instantaneous luminosity.

### 5.3 Track-based exclusivity conditions

Since the method consisting of counting the extra CaloTowers cannot be used in high pileup environment to select two-photon interactions, one has therefore to restrict the exclusivity search to the tracker coverage only ( $|\eta| < 2.5$ ), as its fine granularity allows to discriminate the different interactions occurring simultaneously by looking at the reconstructed clusters of tracks.

Consequently, the philosophy is rather to count the number of extra tracks reconstructed offline and associated to the hard scatter vertex to select exclusive ones. For  $\gamma\gamma \rightarrow \mu^+\mu^-$ , this selection rule is very powerful. Sometimes, electronic noise in the tracker creates an extra fake track, but on average it is reconstructed far from the original vertex.

The power of the method is then strongly dependent of the efficiency to reconstruct charged particles trajectory, even at low transverse momentum, on of their spatial resolution. The first factor was studied with Monte-Carlo samples of inclusive Drell-Yan, for which any charged particle within the tracker coverage  $|\eta| < 2.5$  is considered to compute the efficiency to find an associated reconstructed track matching with it (requesting an angular distance  $\Delta R = \sqrt{(\Delta\eta)^2 + (\Delta\phi)^2} < 0.15$ ). The  $p_T$  spectrum of

*gen* and *reco* tracks, as well as the efficiency curve, are displayed in Figure 5.5. One can notice that the tracking algorithm is very efficient down to 250 MeV, for which tracking efficiency is still above 80%. Below that threshold, it drops rapidly as almost any charged particle with  $p_T < 100$  MeV is reconstructable. However, as majority of the tracks are supposed to be produced with a transverse momentum larger than 250 MeV, the integrated efficiency remains quite high with roughly 85% of the spectrum reconstructed for inclusive Drell-Yan Monte-Carlo sample.

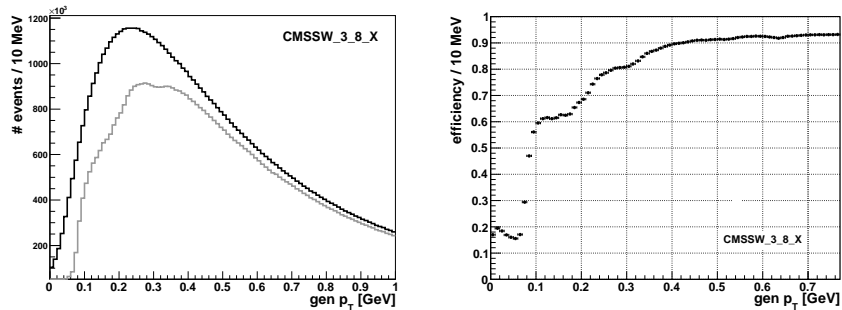


Figure 5.5: Left: transverse momentum spectrum of any charged particles with  $|\eta| < 2.5$  from inclusive Drell-Yan processes, at the generator level (black) and those matching with a reconstructed track (grey). Right: Reconstruction efficiency as a function of generated  $p_T$ .

The primer selection criteria is therefore to select events with only a two-tracks vertex. The efficiency of the method is display in Figure 5.6 showing the number of tracks on vertex (but the two muon ones) for inclusive dimuon sample. Comparison with Drell-Yan and dimuon-enriched QCD Monte-Carlo samples normalized to  $40 \text{ pb}^{-1}$  is also done.

On the left plot, one sees that the global  $N(\text{extra tracks})$  multiplicity distribution is reproduced by the addition of both inclusive samples; the high-multiplicity region is dominated by the QCD-type of events, and the low-multiplicity by DY events. The high fluctuations of the QCD sample is due to limited statistics, and in particular the content in bins 3 or 6 is only due to one Monte-Carlo event with a large weight applied. With increased Monte-Carlo statistics, one expects this bin to be "diluted" among the neighbors.

On the right plot, the zoom on the region of interest of exclusive processes shows an excess in the 0 extra-track bin which cannot be explained by inclusive Monte-Carlo processes.

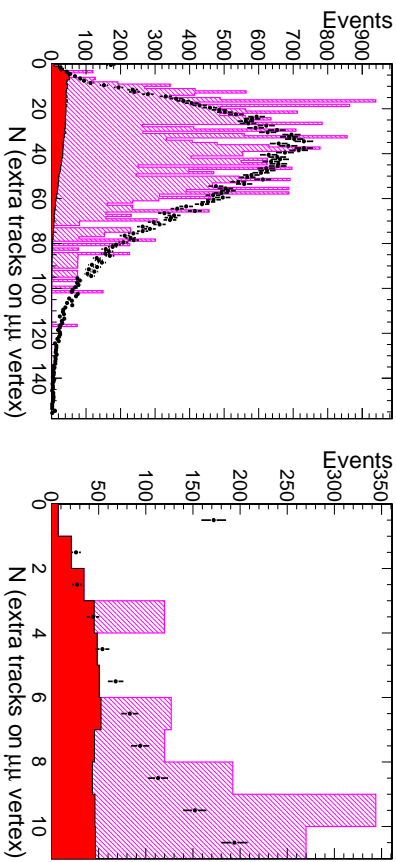


Figure 5.6: Multiplicity of extra tracks associated to dimuon vertex, with all other selections applied. The data is shown compared to the expected contributions from Drell-Yan ( $Z2$  tune, solid histogram) and dimuon-enriched QCD (light histogram) for the full region at left, and zoomed on the region near  $N_{tracks} = 0$  at right

The effect of vertexing efficiency was studied both in inclusive dimuon data and signal Monte-Carlo by computing, among events with a valid dimuon vertex reconstructed with an independent Kalman vertex fitter and for which no tracks exist around 2mm in  $z$ , the efficiency to reconstruct a vertex with only 2 tracks attached and matching with the Kalman one. To ensure the selection of real dimuon vertices and reject those made of two random muons, stringent cuts on the transverse ( $0.085 < vtx_T < 0.115$  cm) and longitudinal ( $|vtx_Z| < 15$  cm) positions of the Kalman vertex have been imposed, as well as on the muons  $z$  separation ( $\Delta z < 0.5$  mm). Results show that the vertexing efficiency in the simulation ( $98.45 \pm 0.03\%$ ) and in the data ( $98.48 \pm 0.09\%$ ) are close to 100% and compatible among them.

In order to further suppress inclusive background which produce a 2-tracks vertex because of vertexing inefficiency, an extra cut on the surrounding tracks is performed. The vertex-to-track distance is computed as the 3D-distance between the offline dimuon vertex position and the reference point of the track, which is taken as the point of transverse closing approach to the  $z$  axis.

This value is selected based on the signal efficiency and background rejection found in ZeroBias data and Drell-Yan Monte-Carlo simulations. For the ZeroBias data this is accomplished by introducing a “fake” dimuon vertex into each event as a proxy for an exclusive dimuon interaction. The fake dimuon vertex position is chosen with a fixed position in  $x$  and  $y$  and Gaussian distribution in  $z$ , with  $\langle x \rangle$ ,  $\langle y \rangle$ ,  $\langle z \rangle$  and  $\sigma(z)$  corresponding to the measured beamspot profile computed on a run-by-run basis. The

extra-track veto is then applied around this position, and the event is accepted if no tracks fall within the veto.

The efficiency and rejection of the track-veto are studied as a function of the veto-size for the ZeroBias “signal” and Drell-Yan background (Figures 5.7 for the comparison and Figure 5.8 for the full data computation). With no extra vertices in the ZeroBias, the efficiency approaches 100% as expected for the no-pileup situation. With the addition of overlap events the efficiency decreases, reaching  $\sim 65\%$  with 8 extra vertices reconstructed.

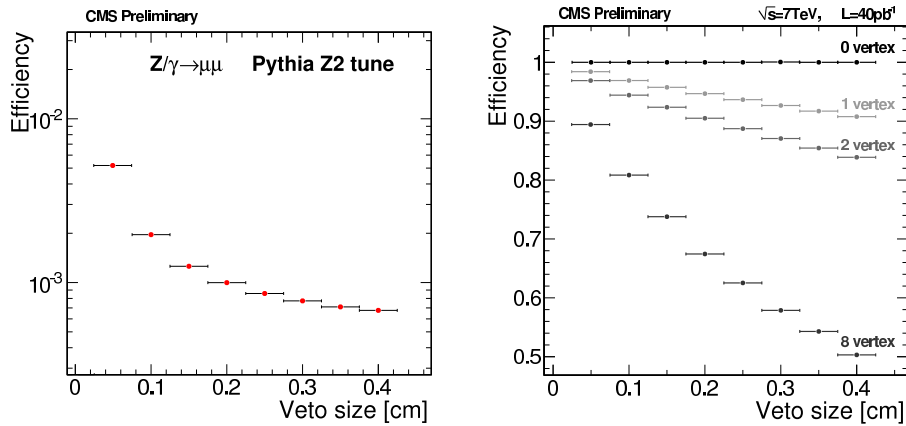


Figure 5.7: Efficiency vs. distance to closest track computed with “fake” vertex method in ZeroBias data (right) and for Drell-Yan Monte-Carlo events (left).

The properties of the extra tracks are displayed on the plots at Figure 5.9. Among selected events passing all the trigger and kinematic criteria, tracks within the range 0 – 2 mm around the primary dimuon vertex are chosen to fill the histograms. The large majority of these tracks have a large number of hits, and 94% are tagged as high-purity tracks. Most of them are reconstructed with a transverse momentum below 1 GeV, down to 100 MeV.

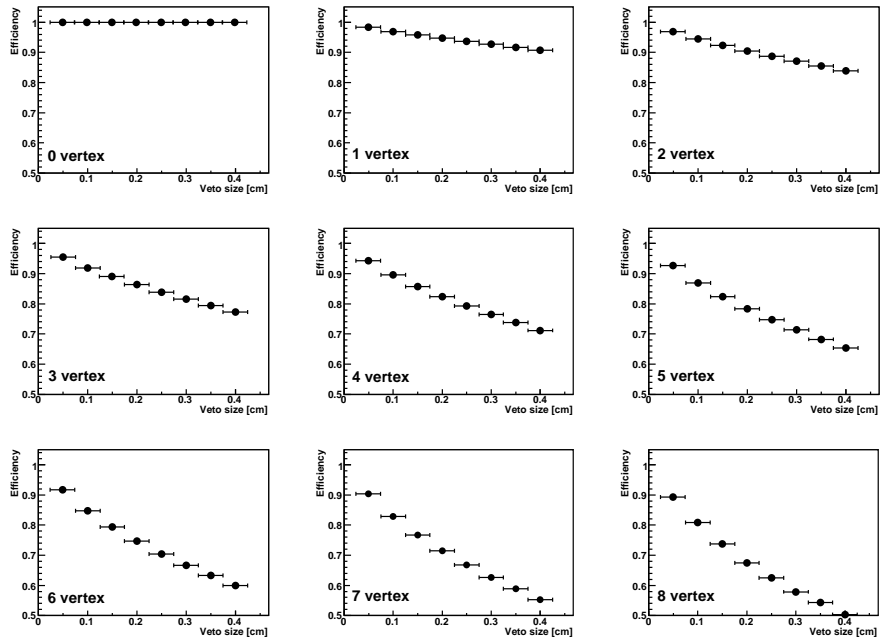


Figure 5.8: Efficiency vs. distance to closest track computed with "fake" vertex method in ZeroBias data.

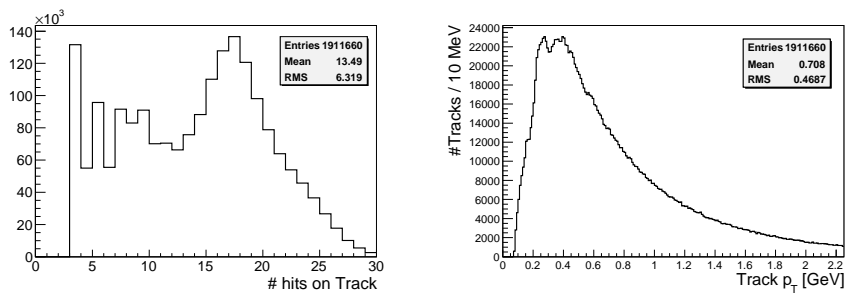


Figure 5.9: Properties of extra tracks within the 2 mm range around the primary vertex.

## 5.4 Pileup effect on track-veto

An additional correction is applied to account for the presence of extra interactions in the same crossing as a signal event. These pileup interactions will result in an inefficiency if they produce a track with a position within the nominal 2 mm veto around the dimuon vertex. This effect is studied in ZeroBias data using the method described in Section 5.3. The nominal 2 mm veto is then applied around the dimuon vertex, and the event is accepted if no tracks fall within the veto. Efficiencies are computed for each different beam bunch crossing configuration per unit of roughly 25 seconds. They are reweighted according to the associated normalised instantaneous luminosity per bunch. The resulting corrections are 95.69% for Run2010A, 91.85% for Run2010B, and 92.29% for the full 2010 data set, with negligible statistical uncertainties.

The exclusivity efficiency variation with time is displayed in Figure 5.10, where the 2 mm track-veto (averaged over all beam configurations of a run) is shown for each run, labelled from 1 to 281. For runs within the same LHC fill, the efficiency increases with time, due to lower population of the proton bunches at the end of a fill. Similarly, the efficiency decreases in the later runs, corresponding to higher pileup.

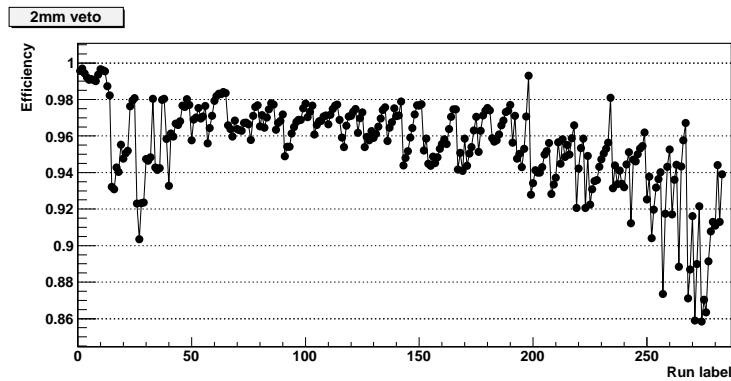


Figure 5.10: Track-based exclusivity efficiency vs. Run number, for a 2 mm veto size.

The efficiency (averaged over all runs) with respect to Bunch-Crossing (BX) is displayed in Figure 5.11 (right); no significant dependence is observed.

This dependence of the efficiency with the pileup conditions is clearly visible in Figure 5.12, showing the mean efficiency with respect to the instantaneous delivered lu-

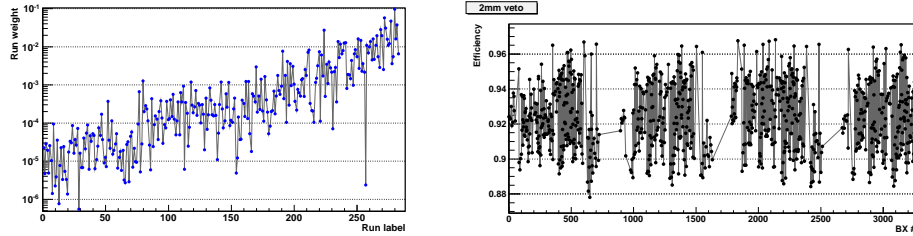


Figure 5.11: Track-based exclusivity efficiency vs. bunch-crossing (right), for a 2 mm veto size. The weight associated to each run of Figure 5.10 is also displayed (left).

minosity expressed in  $\mu\text{b}^{-1}\text{s}^{-1}$ . Two different regimes are observed: for events taken with  $\mathcal{L} < 0.35 \mu\text{b}^{-1}\text{s}^{-1}$ , the efficiency is decreasing as

$$\epsilon = 0.9988 - 0.2085 \times \mathcal{L}$$

while for higher instantaneous luminosities, the reduction is larger as

$$\epsilon = 1.0194 - 0.2810 \times \mathcal{L}$$

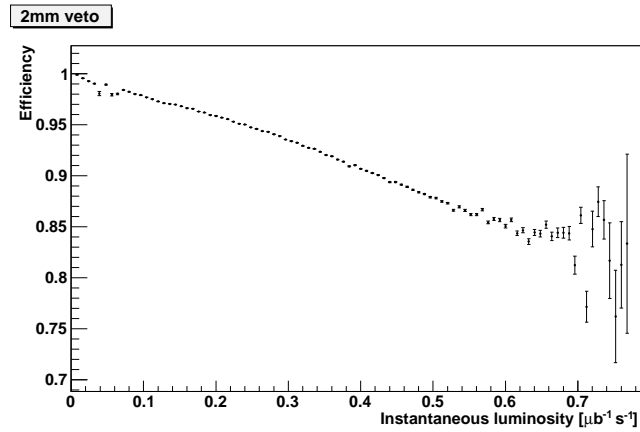


Figure 5.12: Track-based exclusivity efficiency vs. instantaneous luminosity, for a 2 mm veto size

As a cross-check, an alternative efficiency computation uses the track-veto efficiency as a function of the number of visible primary vertices, reweighted by the  $N - 1$  vertex multiplicity derived from inclusive dimuon data triggered on the same data-taking period. The method, illustrated in Figure 5.13, results in a 92.55% efficiency

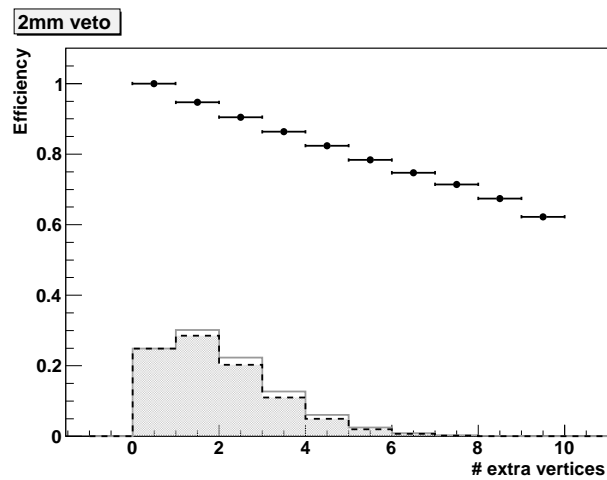


Figure 5.13: Track-based exclusivity efficiency vs. the number the number of visible vertices derived from the "fake vertex" method in ZeroBias data (black dots). Plain line shows the  $(N - 1)$  vertices distribution derived from inclusive  $\mu^+\mu^-$  data, while the shaded zone is the multiplication of both.

correction for the whole Run2010 era, which is fully consistent with the 92.29% found with the nominal method, both with negligible statistical uncertainties.



## Chapter 6

# Measurements of exclusive dimuons with the CMS detector

*“The trouble with measurement is its seeming simplicity”*

Unknown author

### Work done in collaboration with Jonathan Hollar

First measurement is reported of the exclusive two-photon production of muon pairs,  $\gamma\gamma \rightarrow \mu^+\mu^-$ , in proton-proton collisions at  $\sqrt{s} = 7$  TeV. For the muon pairs with invariant mass above  $11.5 \text{ GeV}/c^2$ , and with  $p_T(\mu) > 4 \text{ GeV}/c$  and  $|\eta(\mu)| < 2.1$ , 148 candidates are found in the CMS data sample of  $39.7 \text{ pb}^{-1}$ , with roughly half of them being fitted as from elastic-elastic contribution.

It shows a proof-of-principle that one can select exclusive events produced in pileup conditions with the set of techniques developed in the previous chapter.

The characteristic distributions of the muon pairs produced via  $\gamma\gamma$  fusion are well described by the full Monte-Carlo simulation using the LPAIR event generator. Small and well understood Drell-Yan background to the process is observed.

The exclusive photo-production of vector mesons  $\gamma\mathbb{P} \rightarrow J/\Psi p$  (71 candidates) and  $\gamma\mathbb{P} \rightarrow \Upsilon$  (64 candidates) have also been observed.

## 6.1 Exclusive dimuon final states phenomenology

The two-photon production of muon pairs is a pure QED process: the incoming protons from the LHC beamline exchange photons with small virtualities. Photons fuse to produce a pair of muons which is possibly detected within the central CMS detector. After photon-exchange, the two protons remain intact and are scattered at small angle. The process is schematically represented by its Feynman diagram on the left side in Figure 6.1. Unless one can tag the protons with the High Precision Spectrom-

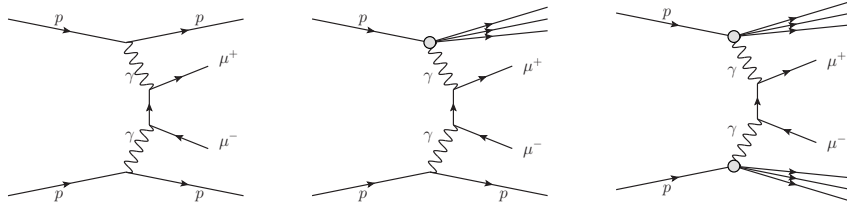


Figure 6.1: Feynman diagrams for exclusive and semi-exclusive dimuon signal: elastic-elastic  $\gamma\gamma \rightarrow \mu^+\mu^-$  (left), elastic-inelastic (middle) and inelastic-inelastic (right).

eter stations (which is not available in 2010-2011 runs), the semi-exclusive processes involving (*single-* and *double-*) inelastic photon exchange, hence leading to proton dissociation, become an irreducible background that needs to be suppressed (see middle and right side of Figure 6.1). The expectations from the LPAIR Monte-Carlo generator –for which the generation principles have been detailed in Section 2.3– for  $\sqrt{s} = 7$  TeV, with acceptance cuts on  $p_T(\mu) > 1.5$  GeV and  $|\eta(\mu)| < 3$  are:

$$\begin{aligned}
 \sigma(pp(\gamma\gamma) \rightarrow p\mu^+\mu^-p) &= 108.5 \text{ pb} \\
 \sigma(pp(\gamma\gamma) \rightarrow p\mu^+\mu^-Y) &= 122.1 \text{ pb} \\
 \sigma(pp(\gamma\gamma) \rightarrow Y_1\mu^+\mu^-Y_2) &= 47.4 \text{ pb}
 \end{aligned}
 \tag{6.1}$$

with  $Y$  representing the proton-dissociative part. The elastic-elastic cross-section is known at the impressive precision of  $\mathcal{O}(1\%)$ , which makes it a strong candidate process for the integrated luminosity calibration as detailed in Chapter 7.

On the contrary, inelastic photon-exchange processes are much less controlled theoretically, and require inputs from the proton structure function measurement and corrections for proton rescattering. One usually assigns a 20% uncertainty on the photon flux.

However, these semi-exclusive events have significantly modified kinematical distributions compared to the elastic-elastic signal, and thus allow for an efficient separation. The phenomenology of these different interactions is shown in Figure 6.2. Acceptance cuts  $p_T(\mu) > 3$  GeV and  $|\eta(\mu)| < 2.5$  are applied to all Monte-Carlo samples. From top to bottom, from left to right, the  $\mu^+\mu^-$  invariant mass, the single muon transverse momentum, the  $p_T$  balance  $|p_T(\mu^+) - p_T(\mu^-)|$  and the acoplanarity  $|\phi(\mu^+) - \phi(\mu^-)|/\pi$  are displayed. It clearly shows that, at least at generator level, the

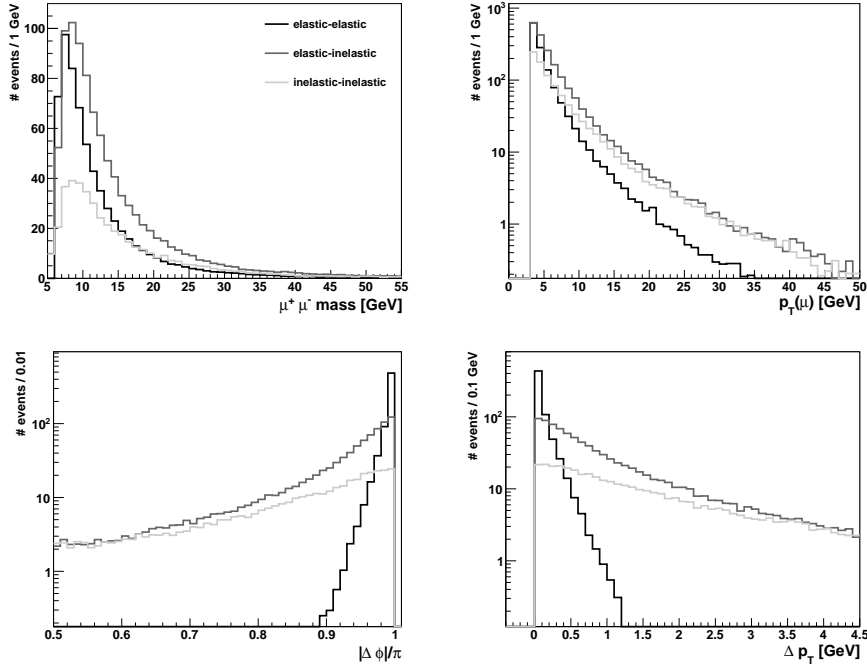


Figure 6.2: Muon kinematics comparison for elastic and inelastic photon-exchange processes, with  $p_T(\mu) > 3$  GeV and  $|\eta(\mu)| < 2.5$

elastic-elastic signal has the unique property to have muons produced back-to-back in the transverse plane ( $\Delta\phi \simeq \pi$ ) and balanced in  $p_T$  ( $\Delta p_T \simeq 0$ ). These striking features are present thanks to the very small virtualities of the exchanged photons.

Another source of exclusive muons comes from the photo-production of vector mesons  $J/\Psi$ ,  $\Psi(2S)$ ,  $\Upsilon(1S)$ ,  $\Upsilon(2S)$ ,  $\Upsilon(3S)$  decaying to two muons (see left side in Figure 6.3, resulting from the interaction of a pomeron with a  $q\bar{q}$  excitation from a photon).

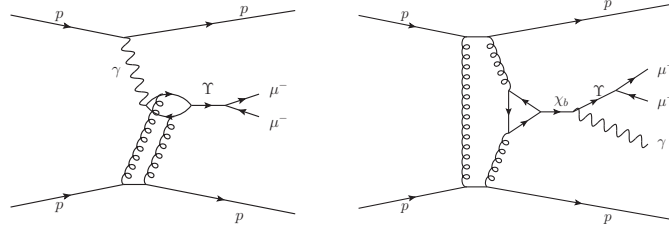


Figure 6.3: Feynman diagrams contributing to exclusive quarkonium signal: photo-production of  $\Upsilon$  (left) and CEP of  $\chi_b$  states (right). Similar diagrams can be drawn for the photo-production of  $J/\Psi$  and for the corresponding CEP of  $\chi_c$ .

While photo-produced events result from different physics process, their experimental signatures are very similar to the  $\gamma\gamma \rightarrow \mu^+\mu^-$  ones. However, they are easily suppressed by adding a cut window on the invariant mass reconstructed with the two muons. Kinematical distributions for the elastic  $J/\Psi$  and  $\Upsilon$  photo-production generated with StarLight ([90] and details in the corresponding sections) are displayed in Figure 6.4 with a comparison to the LPAIR prediction. Acceptance cuts  $p_T(\mu) > 1 \text{ GeV}$ ,  $|\eta(\mu)| < 2.5$  and  $m < 12 \text{ GeV}$  have been set to the whole Monte-Carlo samples. Specific studies of observation of exclusive  $J/\Psi$  and  $\Upsilon$  events at the LHC have been performed in Sections 6.6 and 6.5 respectively.

Finally, exclusive muon pairs may also arise from the Central Exclusive Production of  $\chi$  states. Strictly speaking, the muon pair is not produced exclusively as an extra photon is created from the  $\chi_c$  and  $\chi_b$  decays, as shown in Figure 6.3. However, the energy of the photon is usually too soft ( $\langle E \rangle < 1 \text{ GeV}$ ) to produce a significant signal above the calorimeter noise. The photon energy spectrum from the CEP of  $\chi_b$  (left) and  $\chi_c$  (right) as predicted by the SuperChic generator ([92] and details in the corresponding sections) is shown in Figure 6.5.

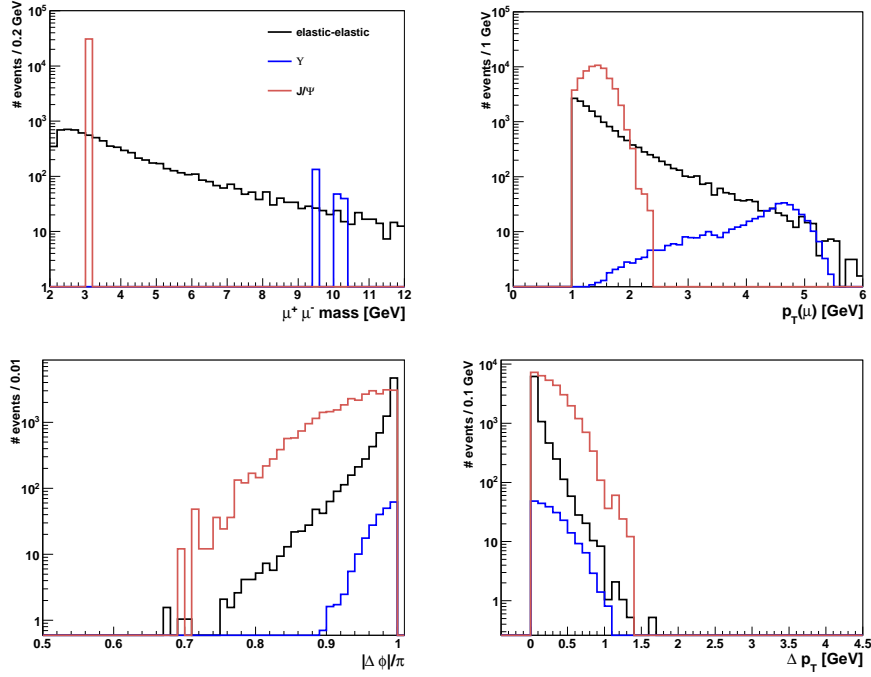


Figure 6.4: Muon kinematics comparison for elastic  $\gamma\gamma \rightarrow \mu^+\mu^-$  and  $\gamma p \rightarrow VMp$ . Details are given in the text.

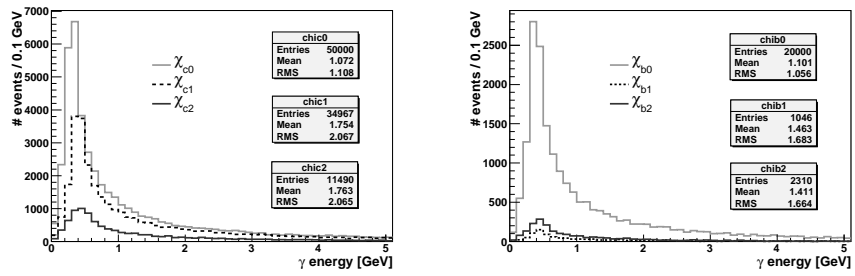


Figure 6.5: Energy spectrum of the photon in the decay  $\chi_c \rightarrow \gamma J/\Psi$  (left) and  $\chi_b \rightarrow \gamma \Upsilon$  (right) produced through CEP. The distributions are normalized to the expectation from Super-Chic.

## 6.2 Event selection

The dataset used for this analysis corresponds to an integrated luminosity of  $39.70 \text{ pb}^{-1}$ , collected at a center of mass energy  $\sqrt{s} = 7 \text{ TeV}$ . In order to maintain a consistent trigger selection across the entire dataset, several input Primary Datasets are used for different data-taking periods, similar as in [7].

The selection of signal proceeds in three steps. First, from the sample of triggered events, the exclusivity selection is performed to keep only events with no other tracks than the two muons. Then, the muons are required to satisfy some identification criteria. Finally, highly-constrained 4-momentum of the signal muons is used to apply strong kinematic cuts. All selection steps are described in the following.

### 6.2.1 Trigger and muon selection

Events were selected online by an algorithm trigger requiring the presence of two muons with a minimum  $p_T$  of 3 GeV. Muons are reconstructed offline by combining information from the muon chambers with charged tracks reconstructed in the silicon tracker, using a “tight” muon selection [89, 7]. We request a pair of oppositely charged muons, both passing the muon selection.

### 6.2.2 Vertexing and tracking exclusivity

The selection requires a valid vertex with exactly two muons, with very loose constraint on the observed  $\chi^2$ . The power of the selection criteria is illustrated in Figure 5.6 and commented in the text. The dimuon vertex is further required to be consistent with a collision in CMS, by requiring  $|z| < 24 \text{ cm}$ , and a transverse position  $0.05 < |d_{XY}| < 0.15 \text{ cm}$ . The asymmetric cut is due to the 1 mm difference between beam center and CMS origin coordinates in transverse plane.

In order to reduce the background from inclusive Drell-Yan and QCD dimuon productions, which typically have many tracks originating from the same vertex as a prompt muon pair, the dimuon vertex is required to be separated by  $> 2 \text{ mm}$  from any additional tracks in the event, using the method developed in Section 5.3.

### 6.2.3 Kinematic selection

In order to minimize systematic uncertainties related to modelling of the muon efficiencies, only muons with  $p_T > 4 \text{ GeV}$  and  $|\eta| < 2.1$  are retained. In addition, the

contribution from exclusive photo-production of  $\gamma p \rightarrow \Upsilon p \rightarrow \mu^+ \mu^- p$  is removed by requiring the muons have an invariant mass  $m(\mu\mu) > 11.5$  GeV.

A possible contamination could arise from cosmic muons, which will produce similar signature as the signal from exclusive  $\gamma\gamma \rightarrow \mu^+ \mu^-$ . However, they will be back-to-back in the transverse and in the longitudinal planes. Requiring an opening angle smaller than  $0.95\pi$  will therefore eliminate any cosmic muons contribution as discussed in 7.3.7.

In order to further suppress the proton-dissociation background, the muon pair is required to be back-to-back in azimuthal angle ( $|\Delta\phi(\mu\mu)/\pi| > 0.9$ ) and balanced in momentum in the transverse plane ( $|\Delta p_T(\mu\mu)| < 1.0$  GeV).

The effect of each step of the selection on the data and signal and background Monte-Carlo samples is shown in Table 6.1. After all selection criteria are applied 148 events remain, where from simulation half are expected to be signal *Elastic-Elastic* events. The contribution from exclusive production of  $\Upsilon$  and  $\chi_b$  is not simulated here, and

Selection	Data	Signal	p diss	Double p diss	DY
Trigger	7.87M	301.44	522.89	276.80	54563
Vertex + Track-exclusivity	921	246.91	436.85	197.12	55.88
Muon ID	724	193.38	335.46	159.59	52.84
$p_T > 4$ GeV, $ \eta  < 2.1$	438	131.68	240.83	106.42	19.70
$m(\mu\mu) > 11.5$ GeV	270	94.52	187.26	85.79	12.49
3D-angle $< 0.95\pi$	257	87.18	178.43	83.33	12.06
$1 -  \Delta\phi/\pi  < 0.1$	203	87.18	126.22	41.01	8.33
$ \Delta p_T  < 1.0$ GeV	148	86.39	78.63	16.06	2.74

Table 6.1: Number of events selected in data and number of signal and background expected from simulation for an integrated luminosity of  $39.7$   $pb^{-1}$  at each selection step. For entries in the line ‘‘Muon ID’’ and below, all efficiency corrections are applied to the simulation.

therefore contributes in the data before requiring  $m(\mu\mu) > 11.5$  GeV.

Two event display of exclusive dimuon events passing the above selection and recorded with single interaction beam-crossing are shown in Figure 6.6. The same display properties than in Figure 1.5 have been used:  $E_T(\text{ECAL}) > 400$  MeV,  $E_T(\text{HCAL}) > 1$  GeV,  $p_T(\text{track}) > 100$  MeV. Except the HCAL energy deposit

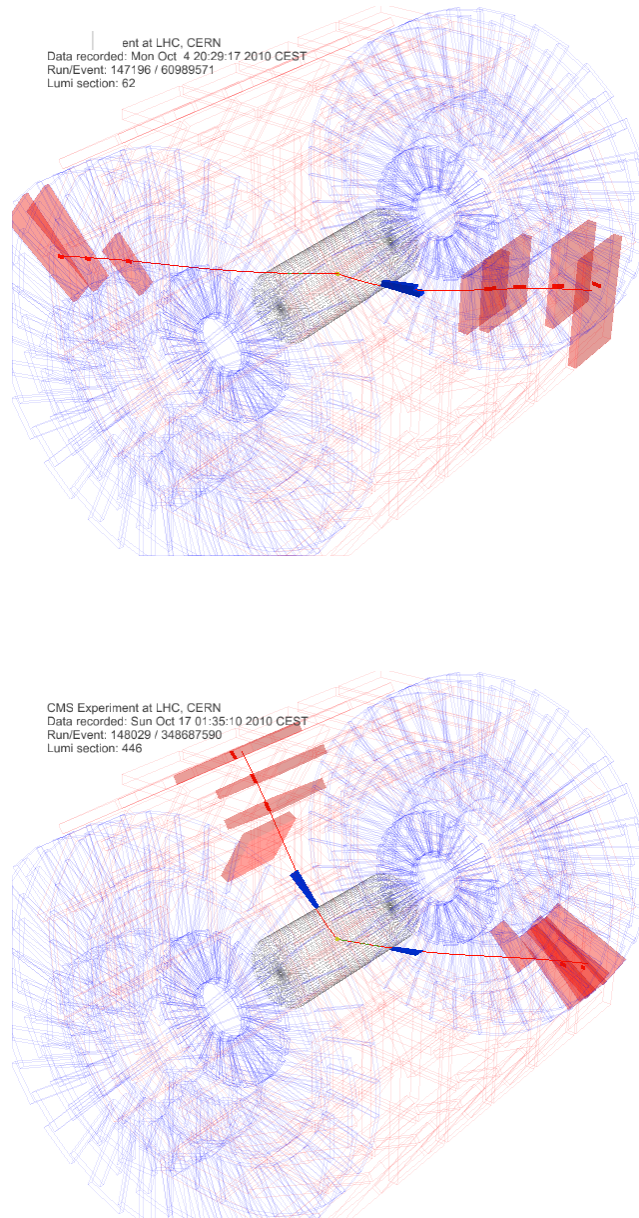


Figure 6.6: Event display of exclusive dimuon events in single interaction beam crossing.

## 6.3 Data-driven efficiency correction

### 6.3.1 Muons efficiency

The trigger and offline muon selection efficiencies are obtained from the Tag-&-Probe [89] method using the samples of inclusive  $J/\psi \rightarrow \mu\mu$  and  $Z \rightarrow \mu\mu$  events from data and Monte-Carlo. These control samples are triggered on one leg only, such that the other track leg used to evaluate the efficiency is unbiased. Below  $p_T = 20$  GeV muons from  $J/\psi$  are used, while above 20 GeV muons from  $Z$  are used. The efficiencies are measured in bins of  $p_T$ , unsigned  $\eta$ , and charge. In addition, due to the change in  $L1$  trigger and the introduction of the cascade algorithm at  $HLL$ , the efficiencies are separated between Run2010A and Run2010B. The resulting efficiency corrections are displayed in Figures 6.7, where the relative difference between data and Monte-Carlo simulation shown in each bin is applied as a correction to the Monte-Carlo. It has to be noticed that the applied efficiencies are also computed as function of the muon charge, while it is integrated over for the plot.

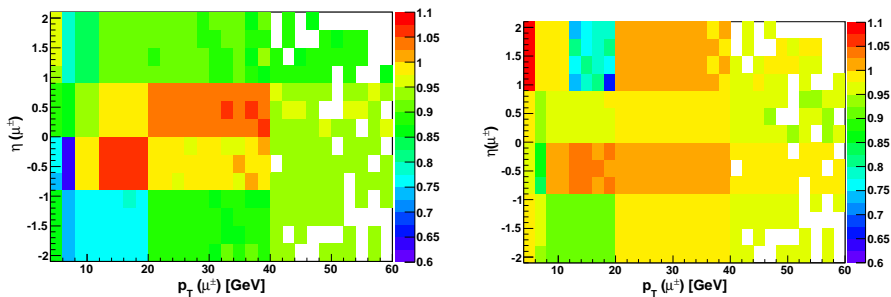


Figure 6.7: Single Muon efficiency correction for  $HLL + \text{Muon } ID$  steps as a function of  $p_T(\mu)$  and  $\eta(\mu)$  integrated on charge, for Run2010A (left) and Run2010B (right) periods.

### 6.3.2 Tracking and Vertexing efficiency

The tracking efficiency is determined using the Tag-&-Probe method on  $J/\psi \rightarrow \mu^+\mu^-$  events. This is done by requiring a muon tag that, when combined with a stand-alone muon reconstructed without the silicon tracking, is consistent with a  $J/\psi$ . The tracking efficiency is then measured on the unbiased stand-alone muon probe leg. The efficiencies are measured in data and Monte-Carlo simulations integrated over

$|\eta| < 2.1$ ,  $p_T > 4$  GeV, and taken to be uncorrelated between the two tracks. The resulting data/MC ratio for the pair of  $(99.18 \pm 0.14)\%$  is applied as a correction to the efficiency.

As the vertexing efficiencies between data and simulation agrees at a 99.97%-level (see Section 5.3), no correction is applied for such effects.

### 6.3.3 Pileup efficiency

Another correction is applied to the Monte-Carlo simulation to account for pileup events in the triggered data, while LPAIR and Pythia Monte-Carlo samples were generated without any extra simultaneous interaction. In the full data sample the average number of extra vertices is 2-3, with less than 10% with  $\geq 4$  extra vertices. Following the computations from Section 5.4, corrections of 95.69% for Run2010A and 91.85% for Run2010B are used.

## 6.4 Observation of exclusive $\gamma\gamma \rightarrow \mu^+\mu^-$

The final invariant mass distribution in the signal region, after applying all selections and efficiency corrections is shown in Figure 6.8. The Monte-Carlo contribution has

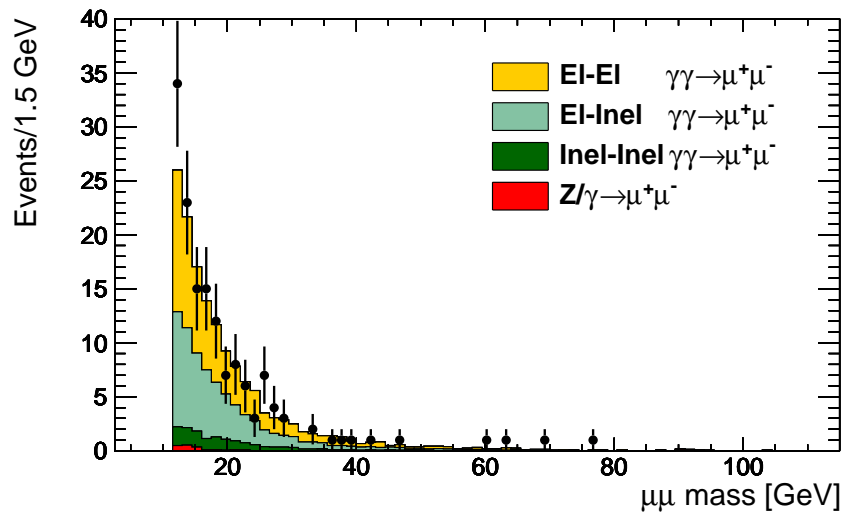


Figure 6.8: Invariant mass spectrum, with all selections applied.

been normalized to the best-fit signal and background yield from the luminosity study in Section 7.2.

The highest-mass event is at 76 GeV; no events consistent with  $Z \rightarrow \mu^+\mu^-$  are observed, as expected for exclusive production in which the  $\gamma\gamma \rightarrow Z$  process is forbidden at tree-level.

In Figures 6.9- 6.11, the data and Monte-Carlo expectations are similarly compared for the  $p_T, \eta, \phi$  of single muons passing all selections, but the one displayed if relevant.

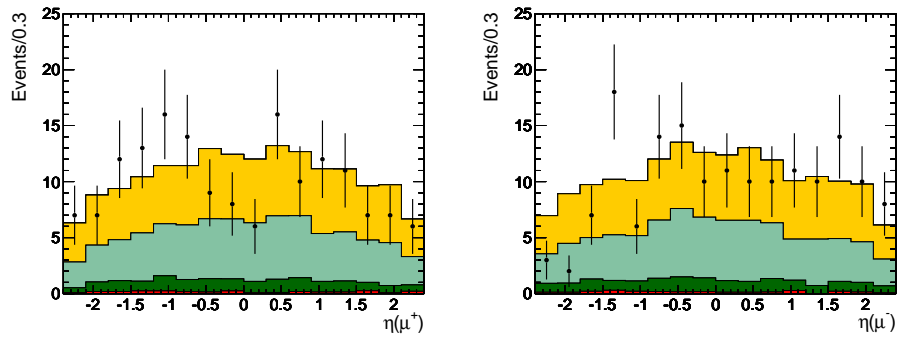


Figure 6.9: Single muon pseudo-rapidity with all selections applied but the  $\eta$  cut, for  $\mu^+$  (left) and  $\mu^-$  (right)

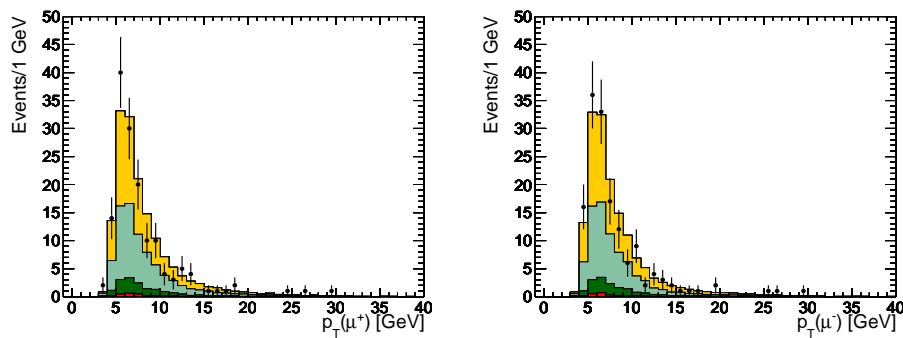


Figure 6.10: Single muon transverse momentum with all selections applied but the  $p_T$  cut, for  $\mu^+$  (left) and  $\mu^-$  (right).

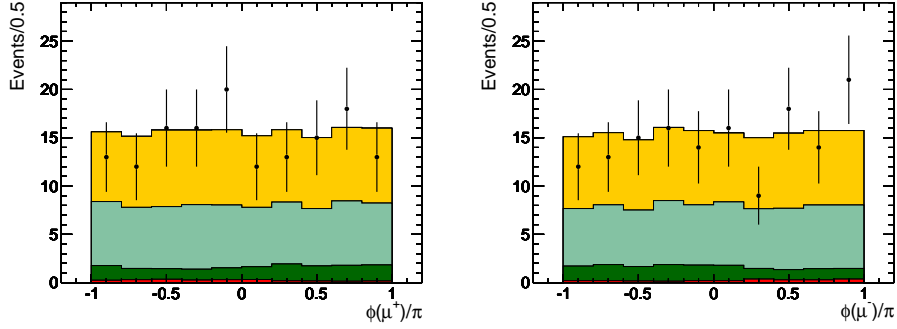


Figure 6.11: Single Muon  $\phi$  angle with all selections applied, for  $\mu^+$  (left) and  $\mu^-$  (right).

In Figures 6.12- 6.14 the  $p_T$ ,  $\eta$ ,  $\Delta p_T$ ,  $\Delta\phi$ ,  $\Delta\eta$  are plotted for the muon pair.

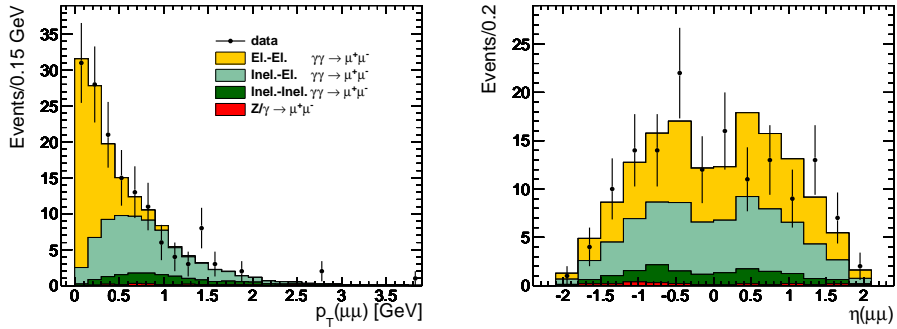


Figure 6.12: Muon pair transverse momentum (left) and pseudo-rapidity (right).

The detection of exclusive muon pairs produced through two-photon interactions is the concrete *in – situ* demonstration of the performance of the methods for selecting exclusive events developed in the previous chapter and driven by need to make it within pileup environment.

The characteristic distributions of the muon pairs produced via  $\gamma\gamma$  fusion, as the distributions of pair acoplanarity and its transverse momentum, are well described by the full Monte-Carlo simulation using the matrix-element LPAIR event generator and the single muon corrections for muon triggering, tracking and reconstruction from Tag-&-Probe method. The observed background from inclusive Drell-Yan and detection

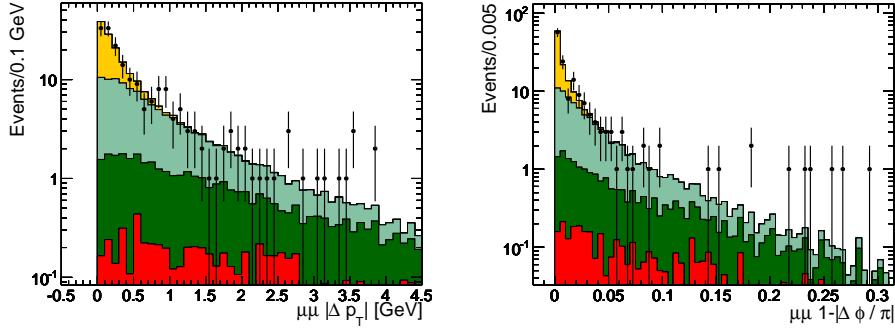


Figure 6.13: Transverse momentum difference (left) and acoplanarity (right), with all other selections applied.

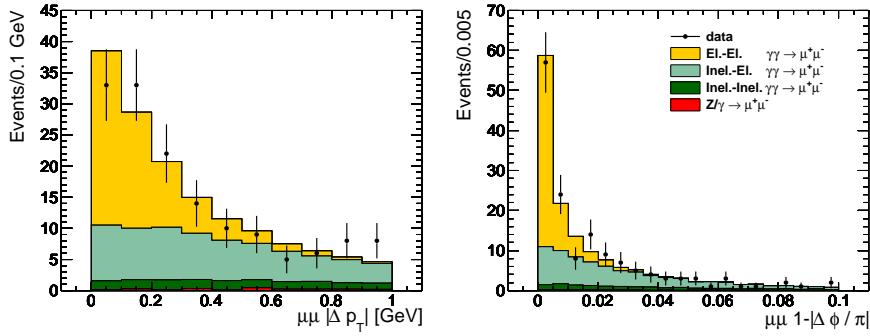


Figure 6.14: Transverse momentum difference (left) and acoplanarity (right), with all selections applied.

is well understood, and the detection efficiencies are under good control, including corrections for the significant event pileup.

This observed agreement between data and MC predictions reinforces the idea to use deviations from the Standard Model rates and kinematics to probe new physics, as in the search for anomalous quartic gauge couplings. In addition, these reactions are good candidates for the absolute luminosity calibration (Chapter 7) and for the a precision calibration of momentum scale and resolution of HPS.

In  $39.7 \text{ pb}^{-1}$ , the measured cross-section for the  $pp \rightarrow p\mu^+\mu^-p$  prediction in the kinematic region  $p_T(\mu) > 4 \text{ GeV}$ ,  $|\eta| < 2.1$  is  $3.352_{-0.534}^{+0.571} \text{ (stat.)} \pm 0.146 \text{ (sys.) pb}$  with respectively statistical and systematic errors. The systematic errors are coming

from studies performed in the next chapter. That values has to be compared to  $4.079 \pm 0.163(\text{lumi.}) \pm 0.041(\text{theory})$  pb predicted by LPAIR, with the 4% uncertainty on the delivered luminosity at CMS.

## 6.5 Observation of $\gamma p \rightarrow \Upsilon p$

The search for exclusive Upsilon photo-production is performed using the same selections and cuts than for the  $\gamma\gamma \rightarrow \mu^+\mu^-$  one. The mass window is however restricted to  $8.5 < m < 11.5$  GeV only for the search, and in  $9.1 < m < 10.6$  GeV for the data and Monte-Carlo comparison.

The mass spectrum is shown in Figure 6.15, among with the expectation of two-photon processes from LPAIR, inclusive Drell-Yan from Pythia and  $\gamma\mathbb{P} \rightarrow \Upsilon \rightarrow \mu^+\mu^-$  from StarLight [90].

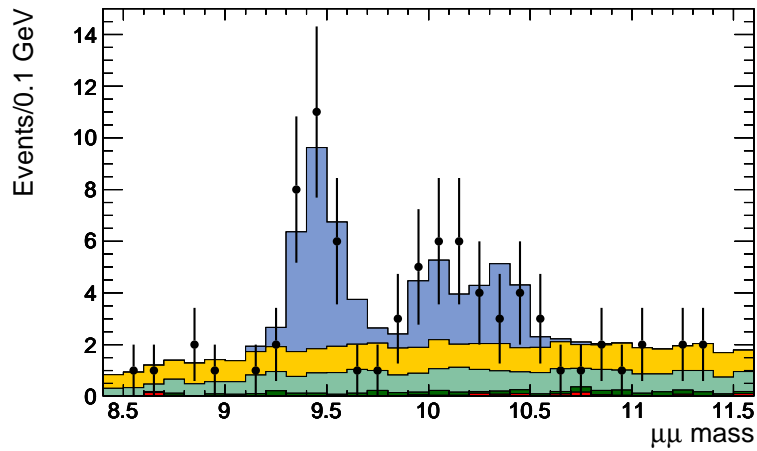


Figure 6.15: Invariant mass spectrum in  $\Upsilon$  mass range, with all selections applied. Data is compared to the prediction from StarLight (blue), exclusive LPAIR (orange) and semi-exclusive LPAIR (green).

The StarLight Monte-Carlo generator is meant for, among other processes, the simulation of exclusive photo-production of vector meson  $pp(\gamma\mathbb{P}) \rightarrow pVMp$ . The generator uses the usual equivalent photon spectrum for the  $\gamma$  side, and photon-proton cross section as measured by experiments at HERA and at fixed target experiments with lepton

beams are used as input for the  $\mathbb{P}$  side. For the Upsilon photo-production, the parameterization  $\sigma_{\gamma p} = 0.06 W_{\gamma p}^{1.7}$  pb (with  $W$  in GeV), which is in agreement with both HERA results, was used to compute the cross-section. Taking into account the branching ratios  $\Upsilon(nS) \rightarrow \mu^+ \mu^-$ , the StarLight predictions for  $\sqrt{s} = 7$  TeV are:

$$\begin{aligned} \sigma(pp(\gamma\mathbb{P}) \rightarrow p\Upsilon(1S)p) \times \mathcal{BR}(\Upsilon(1S) \rightarrow \mu^+ \mu^-) &= 13.5 \text{ pb} \\ \sigma(pp(\gamma\mathbb{P}) \rightarrow p\Upsilon(2S)p) \times \mathcal{BR}(\Upsilon(2S) \rightarrow \mu^+ \mu^-) &= 4.5 \text{ pb} \\ \sigma(pp(\gamma\mathbb{P}) \rightarrow p\Upsilon(3S)p) \times \mathcal{BR}(\Upsilon(3S) \rightarrow \mu^+ \mu^-) &= 3.6 \text{ pb} \end{aligned} \quad (6.2)$$

The expectation of StarLight Monte-Carlo, with all muon, tracking and pileup corrections applied is 36.8 events. However, one needs to remind that inelastic  $\Upsilon$  photo-production simulation is not included.

Alternatively, a fit on the data is performed to retrieve the actual yield. A single Gaussian with floating mean and width is used for the  $\Upsilon(1S)$  resonance, a flat background for the continuum  $\gamma\gamma \rightarrow \mu^+ \mu^-$ , and the  $\Upsilon(2S)$  and  $\Upsilon(3S)$  means and widths are fixed to the nominal PDG values. The fit results predict yields of roughly 27 : 13 : 6 events for  $\Upsilon(1 : 2 : 3S)$  respectively.

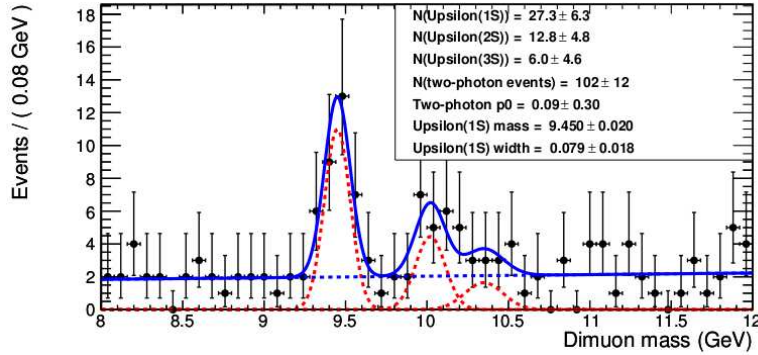


Figure 6.16: Fit on the invariant mass spectrum. Details in the text.

The comparison of the data and the Monte-Carlo simulation is done in Figures 6.17 to 6.19, with the mass window restricted to  $9.1 < m < 10.6$  GeV and all other selection cuts as before. From top to bottom, plots show the dimuon-related kinematics  $p_T^2(\mu\mu)$

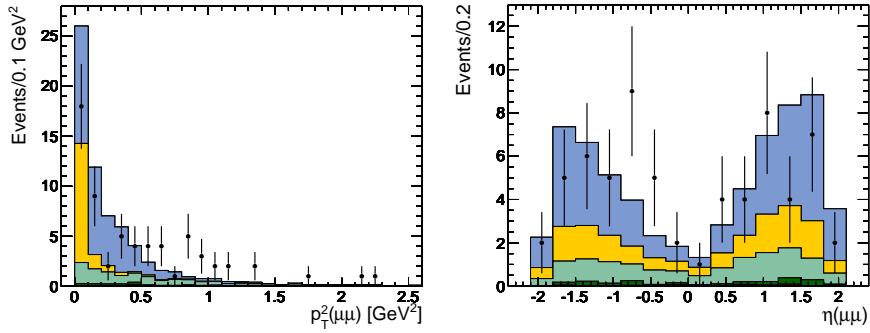


Figure 6.17: Muon pair transverse momentum squared (left) and pseudo-rapidity (right).

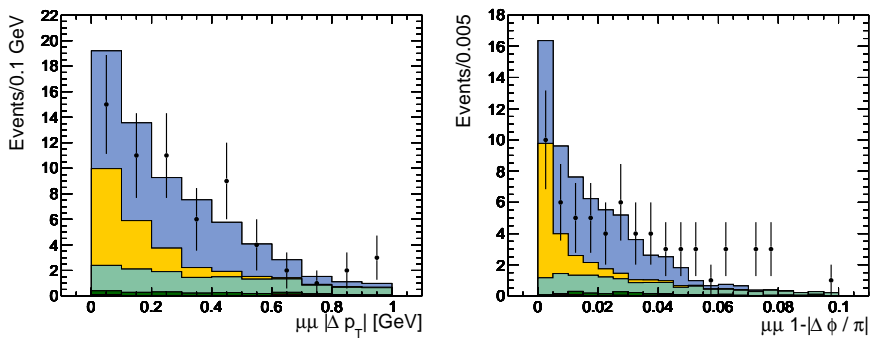


Figure 6.18: Transverse momentum difference (left) and acoplanarity (right).

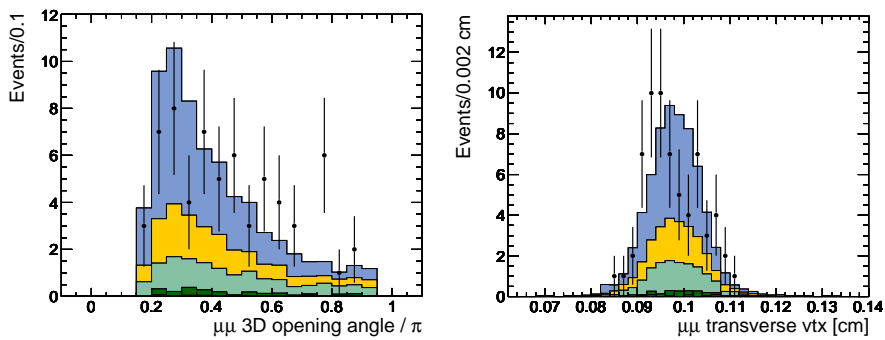


Figure 6.19: 3-dimensional dimuon opening angle (left), and transverse vertex position (right).

and  $\eta(\mu\mu)$ ; the acoplanarity and  $p_T$ -balance; the  $3D$  opening angle and the transverse vertex position.

Assuming that the differences in the data and Monte-Carlo comparisons come only from the StarLight exclusive  $\Upsilon$  part, as the agreement of the LPAIR two-photon production of muon pairs with the data outside the Upsilon mass range was excellent, several conclusions may be drawn, with the large caution that no inelastic photo-produced events and no CEP processes were included in the simulation.

With limited statistics, one can however shows that the  $p_T^2$  spectrum is not well reproduced by the StarLight plus LPAIR Monte-Carlo samples. The reasons for such difference may be double. First, as demonstrated in [90] quantum mechanical interferences although it does not affect the cross-section value in a significant way, it may alter the  $p_T$  spectrum near mid-rapidity. Secondly, inelastic photo-production should contribute at higher  $p_T$  values, where precisely Monte-Carlo expectation is in deficit.

Similar discrepancies are also visible in the  $\Delta\phi$  spectrum, where more data populate the tail than expected with purely exclusive  $\Upsilon$  plus LPAIR; but fewer are found in the first bin.

Among the other distributions, once can notice that no events are found with a highly-displaced transverse vertex, which would have been the sign of a possible contamination by inclusive  $\Upsilon$  events.

### Contamination from $pp(\text{CEP}) \rightarrow p\chi_b p$

The contribution of events in the  $\Upsilon(1S)$  peak due to central exclusive production of  $\chi_b$  was investigated through the simulation of such processes with the SuperChic generator [92], based on publications [93, 94, 95]. One of the major ingredient for the cross-section estimation is the value of the survival probability  $\langle S^2 \rangle$  that the protons will survive despite soft rescattering between the protons (noted  $S_{eik}^2$  for eikonal factor) and the interactions between intermediate partons (noted  $S_{eng}^2$  for enhanced factor).

Using the nominal survival factor of  $S_{eik}^2 = 3.6\%$ ,  $11\%$  and  $8.8\%$  respectively for  $\chi_{b0}$ ,  $\chi_{b1}$  and  $\chi_{b2}$ , and  $S_{eng}^2 = 45\%$  for all, the production cross-sections lead to significant rate of exclusive  $\chi_b$  states produced during the 2010 period at the LHC, up to 105 pb for the CEP of  $\chi_b(0^{++})$ . However, taking into account the recently published measurements of  $\chi_{b,J} \rightarrow \gamma\Upsilon(1s)$  branching ratios from CLEO [96], and the

decay rate of  $\Upsilon(1S)$  into two muons from the PDG, one gets:

$$\begin{aligned}\sigma(pp(\text{CEP}) \rightarrow p\chi_{b0}p) \times \mathcal{BR}(\chi_{b0} \rightarrow \gamma \Upsilon(1S) \rightarrow \gamma \mu^+ \mu^-) &= 0.0494 \text{ pb} \\ \sigma(pp(\text{CEP}) \rightarrow p\chi_{b1}p) \times \mathcal{BR}(\chi_{b1} \rightarrow \gamma \Upsilon(1S) \rightarrow \gamma \mu^+ \mu^-) &= 0.0026 \text{ pb} \\ \sigma(pp(\text{CEP}) \rightarrow p\chi_{b2}p) \times \mathcal{BR}(\chi_{b2} \rightarrow \gamma \Upsilon(1S) \rightarrow \gamma \mu^+ \mu^-) &= 0.0057 \text{ pb}\end{aligned}$$

Generated events were passed through the same reconstruction and analysis procedure. With all corrections applied, the prediction is only of 0.263 events for the data collected in  $39.7 \text{ pb}^{-1}$  with the present selection criteria.

## 6.6 Observation of $\gamma p \rightarrow J/\Psi p$

Due to different kinematics involved in the process, the analysis of exclusive  $J/\Psi$  production requests different selection criteria. Indeed, because of the low-mass of the  $J/\Psi$  around 3.1 GeV and since the vector meson state is produced almost at rest in the transverse plane but boosted in one direction in  $z$ , final state muons are in general of very low- $p_T$  and high- $\eta$ . That demands by consequence a modification of the requirement at each steps of the selection, from the trigger to the kinematics.

On online selected events by a special *HLLT* path (see Appendix A), looser muon reconstruction criteria than before are applied, keeping only the requirement to have tracker muons. Since the reconstruction has been seeded by any tracker track with  $p_T > 0.5 \text{ GeV}$  matching at least one muon segment, a specific muon identification<sup>1</sup> has to be applied to discriminate between real muons which have tendency to penetrate through the whole muon system or fake signal from kaons and hadrons which are usually stopped earlier [97].

To account for specific kinematics of the  $J/\Psi$  events,  $p_T$  threshold was removed and in addition, the pseudo-rapidity cut was enlarged to  $|\eta| < 2.4$  instead of 2.1 in the other analyzes. To avoid displaced vector meson vertices from inclusive production, we restricted the allowed transverse vertex position to  $[0.8, 1.2] \text{ cm}$  instead of the usual  $[0.5, 1.5] \text{ cm}$ . The same tracking and vertexing exclusivity conditions than before were applied.

The mass spectrum, from the lowest-mass exclusive dimuon event recorded ( $m = 2.64 \text{ GeV}$ ) to 4.5 GeV is shown in Figure 6.20 with the expectation from exclusive

<sup>1</sup>TMLastStationAngLoose

$pp(\gamma\mathbb{P}) \rightarrow pJ/\Psi p$  process generated with StarLight, and the central exclusive productions of  $\chi_{c0}$ ,  $\chi_{c1}$  and  $\chi_{c2}$ . One can notice a clear peak round the vector meson mass, plus a second around 3.7 GeV corresponding to the exclusive  $\Psi(2S)$  photo-production.

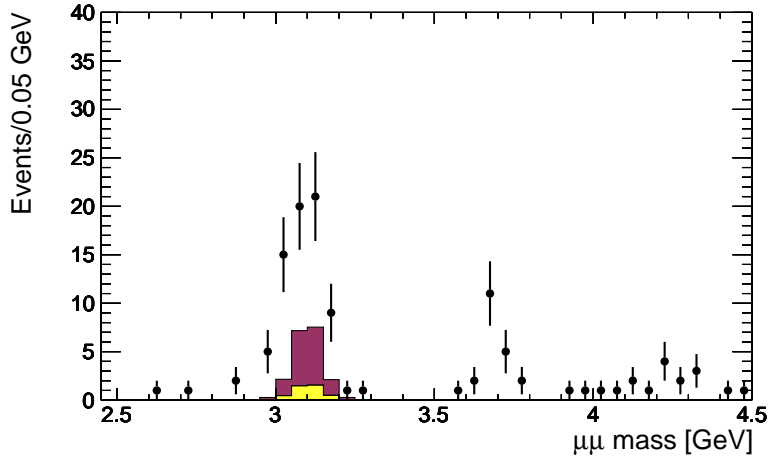


Figure 6.20: Invariant mass spectrum in  $J/\Psi$  mass range. Uncorrected Monte-Carlo predictions from StarLight (pink) and SuperChic (yellow) are also displayed.

The parameterization used to compute the  $J/\Psi$  photo-production production cross-section,  $\sigma_{\gamma p} = 1.5 W_{\gamma p}^{0.8}$  pb (with  $W$  in GeV), gives the following prediction for  $\sqrt{s} = 7$  TeV:

$$\sigma(pp(\gamma\mathbb{P}) \rightarrow pJ/\Psi p) \times \mathcal{BR}(J/\Psi \rightarrow \mu^+ \mu^-) = 3024.3 \text{ pb} \quad (6.3)$$

However, it clearly shows that other sources of exclusive  $J/\Psi$  production than the elastic photo-production generated by StarLight contribute to the signal. The background from two-photon interactions can be estimated by fitting the side-bands out of the  $J/\Psi$  peak and extrapolating into the signal region; it predicts a contamination of 1.875 events. Contamination from inclusive  $J/\Psi$  samples should also be very limited thanks to the tight transverse vertex cut that is set ( $\pm 0.2$  mm around the beam spot).

Therefore, the other components should be the inelastic  $\gamma\mathbb{P}$  production, and the Central Exclusive Production of  $\chi_c$  meson which decays to a  $J/\Psi$  plus a soft photon. The prediction from SuperChic [92] computed with the PDG values of the branching ratios

gives:

$$\begin{aligned}
\sigma(pp(\text{CEP}) \rightarrow p\chi_{c0}p) \times \mathcal{BR}(\chi_{c0} \rightarrow \gamma J/\Psi \rightarrow \gamma \mu^+ \mu^-) &= 188.40 \text{ pb} \\
\sigma(pp(\text{CEP}) \rightarrow p\chi_{c1}p) \times \mathcal{BR}(\chi_{c1} \rightarrow \gamma J/\Psi \rightarrow \gamma \mu^+ \mu^-) &= 129.47 \text{ pb} \\
\sigma(pp(\text{CEP}) \rightarrow p\chi_{c2}p) \times \mathcal{BR}(\chi_{c2} \rightarrow \gamma J/\Psi \rightarrow \gamma \mu^+ \mu^-) &= 43.06 \text{ pb}
\end{aligned}$$

which are much higher than the ones for central exclusive production of  $\chi_b$ 's states. The values of the eikonal survival factor for these processes are 3.7%, 11% and 8.4% respectively. The enhanced survival probability was computed to be 32% for whole of them. One expects therefore a larger contamination in the  $J/\Psi$  peak than it was the case for the  $\Upsilon(1S)$  analysis. Numbers of the cross-section values are directly comparable with the one of  $J/\Psi$  photo-production quoted above.

As we are dealing with a very unusual kinematical regions of high- $\eta$  and low- $p_T$  muons, muons simulation and reconstruction in this range are not perfectly controlled. Extra efforts have to be done to get the correct efficiency to apply to those muons for a full analysis, and to have a clear knowledge of the different contributions from CEP and photo-production.

In addition, as it was demonstrated in [98], the theoretical uncertainty on the gluon density and the experimental uncertainty on the pomeron remnant visibility are such that non-exclusive background from double-pomeron exchange processes could be of similar level as the exclusive  $\chi_c$  signal at the LHC, and have to be considered in the present analysis.

### Exclusive photo-production at the LHC

Although photo-production processes come from different type of physics involving photon and hadronic objects, their final states are produced with similar experimental signature of exclusive muon pairs with striking kinematics than two-photon type of events. Therefore, all selection techniques developed for the selection of  $pp(\gamma\gamma) \rightarrow p\mu^+\mu^-p$  events are directly applicable to detect exclusive photo-production. With the observation of the  $J/\Psi$ ,  $\Psi(2S)$  and  $\Upsilon(nS)$  peaks in the invariant mass distribution of exclusive muon pairs, new possibilities to study diffraction at high energy appear.

The measurement of any cross-section is a difficult study to tackle. Indeed, the value of  $\sigma(\gamma p \rightarrow VMp)$  is irrelevant if not quoted as a function of  $W_{\gamma p}$ , the photon-proton center of mass. At HERA, this task was simplified by the fact that the 'proton side' and the 'photon side' were clearly identified, and the recoils easily measurable. On the contrary at the LHC, there is no possibility to distinguish which proton emitted the pomeron or the photon.





## Chapter 7

# Absolute luminosity calibration

*“For offline analyzes, the design goal is a systematic accuracy of 5%, although every reasonable effort will be made to produce a more accurate result”*

CMS TDR, 'Luminosity' chapter (2006)

The integrated luminosity is a fundamental quantity to all physics analyzes for an absolute normalization of the observed cross-section. This is essential when the results have to be put in perspective with the expectation from the theory, for instance to claim a discovery or to release precision measurement. The determination of the absolute luminosity, *i.e.* the number of delivered collisions between protons, has therefore to be measured with the highest accuracy.

### 7.1 LHC Luminosity determination

Within CMS, the instantaneous and integrated luminosities for the 2010 data were initially measured from the occupancy of the HF detector [99]. Two different methods to get the real-time luminosity are used: the measurement of the average fraction of empty HF towers to derive the mean number of interactions per bunch crossing (“zero-counting” method), or alternatively the measurement of average energy per tower which scales linearly with the luminosity. Overall calibration is performed with Van der Meer scans aiming to measure size and shape of the interaction region by recording the relative interaction rate as a function of transverse beam separation. The overall systematic error on the absolute *lumi* value of 4% is dominated by the LHC

beam current intensity uncertainty (1.7%), by the variation between both methods (2.5%) and by length-scale for beam-separation determination (1.2%).

An alternative method to normalized the luminosity is to monitor the production rate of  $W$  and  $Z$  vector bosons and compare them to NNLO calculations [100]. The main issues are from the uncertainties on the PDF and the geometric acceptance of the detectors.

Since the exclusive two-photon production of lepton pairs is basically a pure QED process, with small theoretical uncertainties and striking kinematic distributions, it comes to be an attractive candidate for absolute calibration of luminosity of  $pp$  collisions [31, 32]. Indeed, detailed studies showed that corrections due to hadronic interactions between the elastically scattered protons are well below 1% and can be safely neglected [31].

## 7.2 Signal selection

After all selections and muon corrections applied, prediction from the Table 6.1 is that the sample of exclusive dimuon consists roughly of 50% of signal and 50% of irreducible background dominated by single photon-exchange processes. For the future luminosity calibration, ones wants to extract only the exact contribution from elastic-elastic signal, with a minimum of contamination from (single and double) inelastic photon-exchange backgrounds. Hopefully, as it can been observed on generator-level distributions in Figure 6.2, these processes have significantly modified kinematics, which allow for an effective separation.

The elastic  $pp(\gamma\gamma) \rightarrow p\mu^+\mu^-p$  contribution is therefore extracted by performing a 1-D binned maximum-likelihood fit to the  $p_T(\mu\mu)$  distribution. Monte-Carlo templates are used for the elastic-elastic signal, single inelastic, double inelastic, and Drell-Yan contributions for  $L = 39.7 \text{ pb}^{-1}$  and all corrections applied, as displayed in Figure 7.1. This variable has the advantage to be directly related to the  $t$  variable and therefore expects significantly different shapes for the signal and the background: the elastic-elastic  $\gamma\gamma \rightarrow \mu^+\mu^-$  process is peaked in the 'small- $p_T(\mu\mu)$  region', and drops rapidly with almost no contribution above  $p_T(\mu\mu) = 0.5 \text{ GeV}$ ; while for the single-inelastic processes, events rather populate the 'high- $p_T(\mu\mu)$  region' with a large tail.

The fit contains 3 free parameters: one for the global normalization and two for the single inelastic process modelling: one parameter to correct its yield relative to the

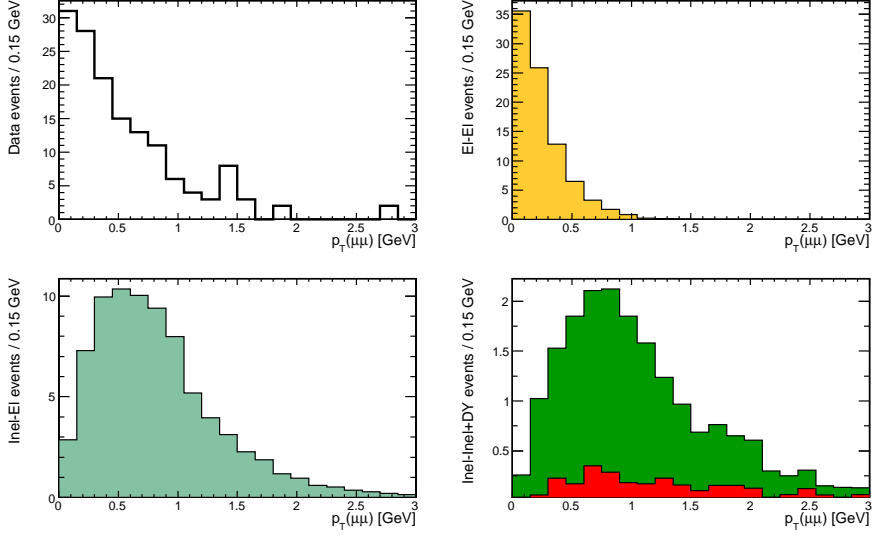


Figure 7.1: Input data (top left) and Monte-Carlo templates for the fit, with elastic-elastic (top right), elastic-inelastic (bottom left), inelastic-inelastic and Drell-Yan (green and red in bottom right) contributions. For each process, all muon efficiency corrections are applied and distributions are normalized to  $39.7 \text{ pb}^{-1}$ .

LPAIR prediction ( $N$ ) and another to correct the slope of proton distribution with an exponential factor ( $a$  in  $e^{-ap_T^2}$ ) are introduced. The third parameter ( $L$ ), applied to all templates, is the Monte-Carlo normalization to the data, and is directly equivalent to the elastic signal yield relative to the LPAIR prediction for  $39.7 \text{ pb}^{-1}$ . The double-inelastic and Drell-Yan  $p_T(\mu\mu)$  shapes are fixed from simulation, while the small contribution from exclusive  $\gamma\gamma \rightarrow \tau^+\tau^-$  is neglected (see discussions in the systematics section).

Procedure can be schematically summarized as:

$$h_{Data} \rightarrow \text{fit}([h_{El-El} + h_{DY} + h_{Inel-Inel}] \times L + [h_{Inel-El}] \times L \times N \times e^{-ap_T^2})$$

with  $h_X$  the Monte-Carlo template of the  $p_T(\mu\mu)$  distribution for process  $X$ .

The philosophy of this parameterization is to use the advantage of the extremely well predicted yield and shape of the elastic-elastic signal to fit the correction to the absolute luminosity as the global yield normalization. Indeed, previous and current measurements of exclusive lepton pairs at H1 [101], CDF [102] and LHC-b [103] are in agreement with the LPAIR predictions. The major irreducible background consisting

in the single-inelastic process, is treated separately in the fit as large uncertainties remain, by allowing for a separate data-driven normalization and shape modelling.

The nominal fit procedure is done with a 0.15 GeV bin width in the range  $[0, 3]$  GeV. The resolution, purity and stability of each bin has been computed using LPAIR Monte-Carlo signals. The absolute resolution is obtained by fitting the distribution of  $(reco - gen) p_T$  distribution with a Gaussian of null mean, and use the  $\sigma$  values and their errors to build the plot in Figure 7.2. The resolution is rather constant around 70 MeV.

The purity (as a function of  $reco p_T$ , fraction of events which originate from this bin at  $gen$  level) and stability (as a function of  $gen p_T$ , fraction of events which remain after  $reco$  step) plots also show constant result over the whole  $p_T$  spectrum, but for the first bin in which a bias is introduced due to the fact that  $p_T$  cannot be reconstructed with negative value.

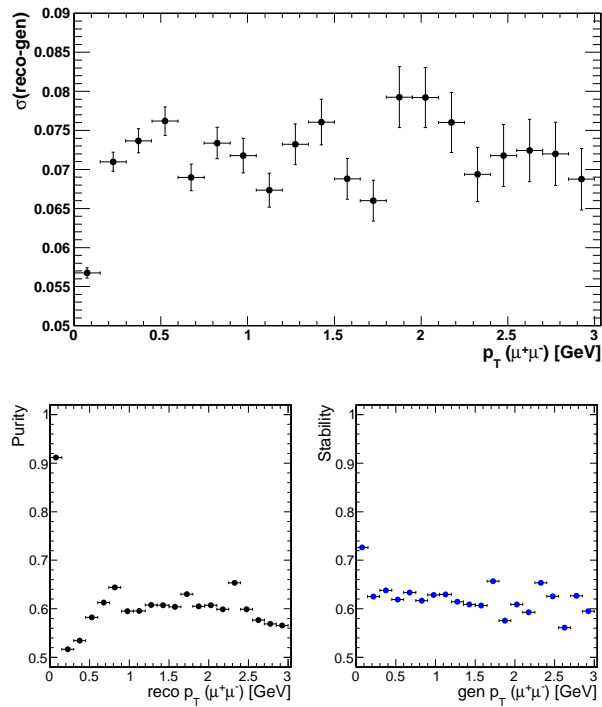


Figure 7.2: Absolute resolution on  $p_T(\mu\mu)$ , purity and stability vs.  $p_T(\mu\mu)$ .

The best fit to the data is shown in Figure 7.3, which shows that the best-fit curve is consistent with the observed  $p_T(\mu\mu)$  distribution within the experimental errors. The

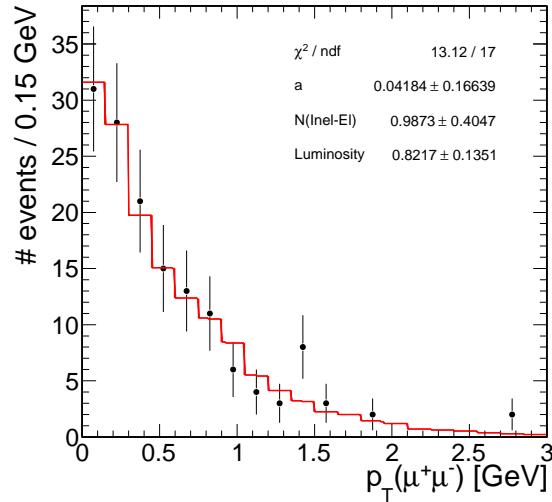


Figure 7.3: Best fit to the  $p_T(\mu\mu)$  distribution.

use the log-likelihood method ensures that the likelihood is built assuming a Poisson distribution in each bin, such that empty data bins in the background region are treated correctly. The fit result on the luminosity and inelastic correction parameters gives:

$$\begin{aligned}
 \text{slope: } & a = 0.042^{+0.200}_{-0.148} \\
 \text{inelastic yield: } & N = 0.987^{+0.495}_{-0.346} \\
 \text{luminosity: } & L = 0.822^{+0.140}_{-0.131}
 \end{aligned} \tag{7.1}$$

with statistical asymmetric errors computed with `Minos`, *i.e.* with other parameters fixed to their best-fit value. The luminosity correction factor and the single-inelastic yields in particular are highly correlated:

Parameter	Global	slope	inelastic yield	luminosity
slope	0.732	1.000	0.607	0.255
inelastic yield	0.912	0.607	1.000	-0.813
luminosity	0.866	0.255	-0.813	1.000

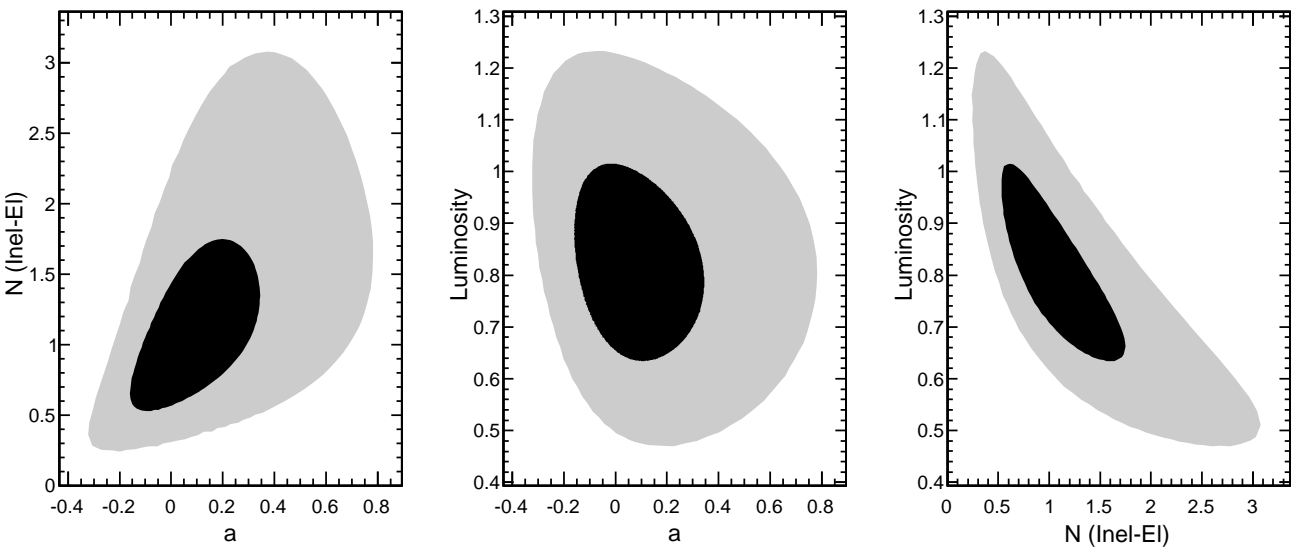


Figure 7.4: 1 and 2 sigma contours in the plane of fitted parameters. From left: inelastic yield vs slope, slope vs. Luminosity, luminosity vs. inelastic yield.

The resulting  $1\sigma$  and  $2\sigma$  intervals projected onto each pair of fit variables are displayed in Figure 7.4.

For any values of the inelastic yield ratio and slope correction within their  $1\sigma$  contour, the extreme values of the luminosity calibration are 63% and 101%. In particular, the no-correction value for the luminosity ( $L = 100\%$ ) may be obtained for an integrated single-inelastic normalisation (*i.e.* the effect of  $N$  and  $a$  combined) of 63% to 68% with respect to the LPAIR prediction.

## 7.3 Systematic effects

Systematic uncertainties related to the pileup efficiency correction, muon trigger and reconstruction efficiency corrections, momentum scale, LHC crossing angle and description of the backgrounds in the fit are considered.

### 7.3.1 Pileup correction systematics

The track-veto efficiency is studied in ZeroBias data by varying the nominal veto distance from 1.0 to 4.0 mm, and by varying the quality cuts and number of hits on tracks considered for the veto. The same method as described in Section 5.3 has been used, *i.e.* compute the track-veto efficiency around a fake 2-tracks vertex and reweight each efficiency by the relative instantaneous luminosity for each bunch-crossing. The resulting changes from the nominal 92.29% efficiency are shown in Table 7.1. The results are further compared to the effect of applying the same variations to the selected sample of dimuon events, removing the  $\Upsilon$  mass cut  $m < 11.5$  GeV to increase the statistics with exclusive Upsilon photo-produced events; in both samples the relative change in selected events is consistent.

Any efficiency dependence with the pileup conditions has been found by splitting the whole sample into two almost equivalent parts. In the first  $19.03pb^{-1}$  where the pileup efficiency correction is 94.29%, 78 events have been found, in which the fit extracts an Elastic-Elastic contribution of  $41.0^{+9.2}_{-8.4}$  events; while for the last  $20.95pb^{-1}$  with a PU correction of 90.18%, a total of 70 events are selected, with fitted signal contribution of  $29.8^{+8.3}_{-7.3}$  events. Both are consistent within  $1\sigma$ , and even more if one remembers that the signal and background yields are highly anti-correlated such that  $(N, L)$  couple values extend to large part of the phase space.

Exclusivity-selection	ZB data	$\mu\mu$ data	ZB ratio	$\mu\mu$ ratio
track-distance < 1.0 mm	95.01%	270	0.971	0.981
track-distance < 2.0 mm	92.29%	265	1	1
track-distance < 3.0 mm	89.61%	259	1.030	1.023
track-distance < 4.0 mm	87.16%	254	1.059	1.043
high-purity tracks	93.14%	269	0.991	0.985
> 10 track hits	94.04%	270	0.981	0.982
high-purity with > 10 track hits	94.07%	270	0.981	0.981

Table 7.1: Selection efficiencies for different track-veto size and quality selections. Columns 3 and 4 show the relative difference from the nominal 2 mm veto, for ZeroBias data and selected dimuon events.

### 7.3.2 Muon efficiencies

The statistical uncertainty on the efficiency correction for trigger and offline muon selection is evaluated by performing a toy Monte-Carlo study in which each single muon efficiency correction is varied independently within its statistical uncertainty derived from the Tag-&-Probe study. Variations of both muons of the pair are then used to recompute the overall dimuon efficiency correction. From 1000 pseudo-experiments, the RMS of the distribution results in an uncertainty of 0.80% which is used as a systematic uncertainty.

Additional systematic effects may come from the different properties of muons in the  $J/\psi$  or  $Z$  control sample versus the  $\gamma\gamma \rightarrow \mu^+\mu^-$  signal. As the Tag-&-Probe study is only sensitive to single muon efficiency, and since the corrections applied are taken as the product of the two muon efficiencies of the pair, therefore the effect of the correlations between muons are not modelled. A check is performed by removing, in the  $J/\psi$  control sample, events in which the two muons bend towards each other in the  $r - \phi$  plane. Such events may introduce a correlation in the dimuon efficiency that wouldn't be present in highly-separated muons like for the signal ones. Repeating the luminosity extraction with this change results in a difference of 0.25% from the nominal yield.

### 7.3.3 Crossing angles

The non-null crossing angle of the LHC beams lead to a "kick" of the system in the  $x$  direction. Consequently, the  $p_T$  of the pair is over-estimated by a few MeV, especially for high-mass dimuon events. The data have been corrected for this effect by applying

a Lorentz boost, assuming all collisions happened in the  $xz$  plane:

$$\begin{pmatrix} E \\ p_x \\ p_z \end{pmatrix}' = \begin{pmatrix} 1/\cos(\phi) & -\sin(\phi) & -\text{tg}(\phi)\sin(\phi) \\ -\text{tg}(\phi) & 1 & \text{tg}(\phi) \\ 0 & -\sin(\phi) & \cos(\phi) \end{pmatrix} \times \begin{pmatrix} E \\ p_x \\ p_z \end{pmatrix}$$

with  $\phi$  the half-crossing angle in the  $xz$  plane, with a value set to  $100 \mu\text{rad}$  for all runs but  $170 \mu\text{rad}$  for LHC fill 1439. The fitted value of the luminosity factor changes by 0.96% relatively from nominal fit when applying the corrections.

### 7.3.4 Energy and momentum scale

Using studies of the muon momentum scale derived from  $Z \rightarrow \mu^+\mu^-$ , the  $p_T$  of the muons are shifted by the observed bias,  $\Delta(p_T)$ ,  $\Delta(\phi)$  and other kinematics are re-evaluated; and then the nominal fit re-performed. The resulting relative change in the luminosity fitted value is 0.33%.

As a cross-check on a sample kinematically similar to the signal, we apply all selection cuts except the veto on the  $\Upsilon$  mass region, and perform a fit to the invariant mass spectrum in data (Figure 6.16 and details in the text). The resulting uncertainty on the  $\Upsilon(1S)$  mass is 20 MeV. The nominal signal fit is then performed with the data shifted in  $p_T(\mu)$  by  $\pm 0.02$  GeV, and other kinematical quantities recomputed. No change in the fitted signal yield is observed.

### 7.3.5 Tracking and vertexing efficiency

The vertexing efficiencies between data and Monte-Carlo agrees at a 99.97%-level, and the 0.09% uncertainty on data efficiency is taken as a systematic error.

The resulting data/MC ratio for the pair of  $(99.18 \pm 0.14)\%$  is applied as a correction to the efficiency, and the statistical error on the correction taken as a systematic error.

### 7.3.6 Fit stability

Different bin width and fit ranges have also been tested. Starting from the nominal number of 20 bins in the range  $0-3$  GeV, variations in the bin width ( $0.15 \pm 0.05$  GeV) and fit range ( $[0; 3 \pm 1]$  GeV) show relative deviations by at most  $\sim 3.5\%$  with respect to the nominal yield as shown on the Table next page.

Fit parameters	Variation from nominal yield
[0; 2] GeV	1.76%
[0; 4] GeV	2.63%
100 MeV width	2.69%
200 MeV width	3.65%

However, the variations in the fit range are not physically justified. Extending the range to  $p_T(\mu\mu) = 4$  GeV, one starts to enter the region where the signal is mainly dominated by doubly-inelastic photon exchanges, and therefore the  $N$  and  $a$  parameters are fitted to model both single-inelastic and double-inelastic processes. On the contrary, restricting the range to  $p_T(\mu\mu) = 2$  GeV only, the side-band used for the single-inelastic yield and shape modelling is limited to reduced statistics.

For smaller bin width, the problem appears that the  $p_T(\mu\mu)$  absolute resolution (70 MeV) becomes as large as the bin width. Therefore, the computed values of stability and purity are lowered by  $\sim 10\%$  with respect to the 150 MeV binning. For larger binning, the number of degrees of freedom becomes limited, such that the majority of the elastic-elastic signal is concentrated in the first bin. The fit owns only roughly one bin to discriminate the global yield normalization. Any systematic errors due to the binning or range is therefore considered.

The fit bias is studied by performing a series of toy Monte-Carlo experiments with different input values of the luminosity  $L$  and inelastic yield  $N$ . For each benchmark point, the number of pseudo-data is generated with a Poisson distribution with mean as expected by the Monte-Carlo simulation. The mean and  $1-\sigma$  values of the pull

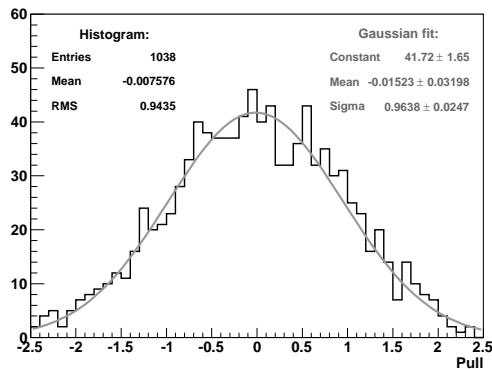


Figure 7.5: Sanity check of the fit stability with the pull of the fitted value of the luminosity for 1038 toy experiments. Results are compatible with a Gaussian of null mean and  $\sigma = 1$ .

distributions are consistent with zero and unity values respectively, as shown in Figure 7.5 for 1038 experiments with fixed  $L = 90\%$  and  $N = 110\%$  for the simulation.

As a cross-check of the template shape, the shape of the  $p_T(\mu^+\mu^-)$  distribution in data is compared to the LPAIR Monte-Carlo sample in the background-dominated regions  $|\Delta\phi(\mu\mu)/\pi| < 0.9$  and  $|\Delta p_T(\mu\mu)| > 1.0$  GeV. No source of strong disagreement is visible with limited statistics available.

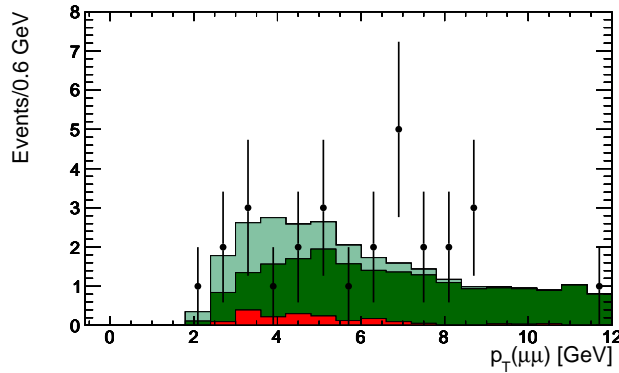


Figure 7.6:  $p_T(\mu\mu)$  distribution in data (points) and simulation (histograms) for the sideband region in  $1 - |\Delta\phi(\mu\mu)|/\pi$  and  $|\Delta p_T(\mu\mu)|$ .

Finally, as another verification, a fit to the  $1 - |\Delta\phi/\pi|$  distribution is performed with the luminosity correction and inelastic ratio to LPAIR as free parameters. The shape of the single-inelastic photon-exchange process is fixed from the simulation, without reweighting of the slope with the  $a$  parameter as previously done. The resulting value of the signal ratio for the best fit value of the luminosity gives  $0.79^{+0.14}_{-0.13}(\text{stat.})$  which is consistent with the nominal result.

### 7.3.7 Backgrounds

#### Collision backgrounds

The yields of the double-inelastic and Drell-Yan contributions are fixed in the nominal fit. The fit is repeated with each of these varied independently by a factor 2. The resulting change in the fitted signal yield is  $< 1\%$  (Table 7.3).

### Other exclusive backgrounds

Another exclusive process not taken into account in the previous lines is the exclusive production of tau pairs  $pp(\gamma\gamma) \rightarrow p\tau^+\tau^-p$ , with fully leptonic decay of the taus in muons. From a Monte-Carlo sample of exclusive  $\tau$  pairs simulated with LPAIR, the contamination after all selection and cuts applied is only 0.0015 pb, as shown in Table 7.2.

Another source of exclusive-like dimuon is the single-diffractive and double diffractive production of lepton pairs, through pomeron exchange(s). Although the production of the muon pair is usually accompanied by extra tracks produced from the pomeron remnant, they may still fake an exclusive state as these tracks are usually produced at low- $p_T$ . The contamination from single pomeron exchange (SPE) and double pomeron exchange (DPE) has therefore been checked with the help of the Pomwig Monte-Carlo generator [104]. Schematic Feynman diagrams for the DPE and SPE production of muon pairs are drawn in Figure 7.7.

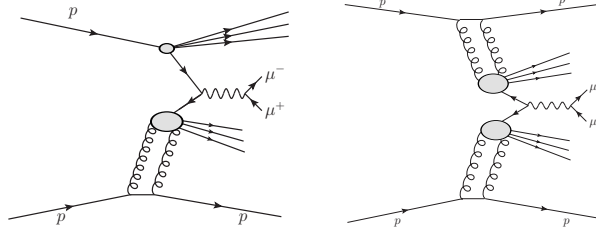


Figure 7.7: Feynman diagrams for Single Pomeron Exchange (left) and Double Pomeron Exchange processes with  $\mu^+\mu^-$  final state. The emission of a pomeron is always accompanied by the  $\mathbb{P}$  remnant.

For the DPE process, the visible cross-section when multiplied by the assumed 5% survival probability is only 1.42 pb, for  $10 < m_{\mu\mu} < 120$  GeV. The generated events were passed to the same reconstruction and analysis procedure than the LPAIR signal, and cumulative result of the selection steps are shown in Table 7.2. A very low contamination, of the order of half-an-event, is expected in the 2010 data. The major reduction of the background is done when applying exclusivity conditions, since DPE production of Drell-Yan is accompanied with two pomeron remnants produced close the primary vertex. The only source of veto-inefficiency arises when the  $p_T$  spectrum of the remnant content is not large enough to produce detectable tracks.

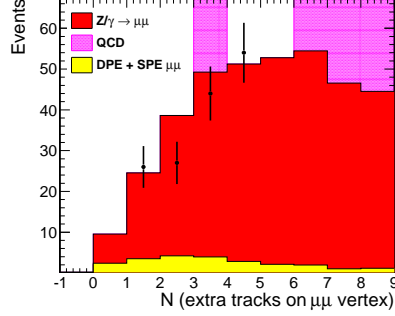


Figure 7.8: Multiplicity of extra tracks associated to dimuon vertex, with all other selections applied. The data is shown compared to the expected contributions from Drell-Yan (Z2 tune, solid histogram), dimuon-enriched QCD (light histogram) and SPE, DPE processes (yellow) zoomed on the region near  $N_{tracks} = 0$ .

The effect is even stronger for SPE processes as vertexing and tracking exclusivity conditions only retains  $\sim 2\%$  of the events. This is due to the fact that only one side is diffractive with surviving proton, while on the other side the usual proton remnant hadronisation takes place. With all selection criteria applied, the expected number of SPE events from Pomwig is around 0.75. Although it remains a large uncertainty on

Selection	$\gamma\gamma \rightarrow \tau^+\tau^-$	<b>SPE <math>\mu^+\mu^-</math></b>	<b>DPE <math>\mu^+\mu^-</math></b>
Trigger	6.12	335.01	15.79
Vertex + Track-exclusivity	0.48	6.08	1.23
Muon ID	0.42	6.00	1.00
$p_T > 4 \text{ GeV},  \eta  < 2.1$	0.24	4.47	0.82
$m(\mu\mu) > 11.5 \text{ GeV}$	0.16	3.64	0.57
$3D\text{-angle} < 0.95\pi$	0.16	3.55	0.55
$1 -  \Delta\phi/\pi  < 0.1$	0.16	2.11	0.50
$ \Delta p_T  < 1.0 \text{ GeV}$	0.05	0.74	0.42

Table 7.2: Number of reducible background events expected from simulation for an integrated luminosity of  $39.7 \text{ pb}^{-1}$  at each selection step, with the 82.2% correction to the luminosity included. For entries in the line “Muon ID” and below, all efficiency corrections are applied to the simulation. A survival factor value of 5% was assumed for both SPE and DPE processes. Diffractive processes have been generated with  $m > 10 \text{ GeV}$  such that numbers prior to mass cut have therefore to be understood as partial numbers.

the survival probability, even a 10% factor applied to both DPE and SPE would result in only 2.5 events contaminating our sample.

It is also worth to mention that the nominal inclusive Drell-Yan sample, which was generated with Pythia Tune Z2 settings, was done with PDFs which already include a diffractive part. However, the present version of Pythia does not simulate correctly hard diffraction, in the sense that it does not produce enough rapidity gaps in the Monte-Carlo with respect to what is observed in the data. On the contrary, if one considers only the hard scatter, it should be correctly simulated with the same set of Tune Z2 parameters, as they were meant to reproduce the track multiplicity and the  $p_T$  spectrum observed at  $\sqrt{s} = 7$  TeV with the CMS detector. Some "double counting" of the Monte-Carlo estimation is therefore happening when Pythia inclusive (which correctly models the hard scatter final states) and the Pomwig diffractive (which correctly models the forward gaps) productions are added together.

### Non-collision backgrounds

The possibility of a large contamination from cosmic muons, which may fake a signal since they will not be correlated with other tracks in the event, is studied comparing the vertex position and three-dimensional opening angle in data and collisions simulation. In Figure 7.9, the three-dimensional opening angle<sup>1</sup> is compared between data and simulation for events passing and failing the nominal  $0.05 < |d_{XY}| < 0.15$  cm requirement for the transverse vertex position. A total of 3 events fail the vertex position selection, all having large opening angles consistent with the expected signature of a cosmic muon. In Figure 7.10, the transverse and  $Z$  vertex positions are compared

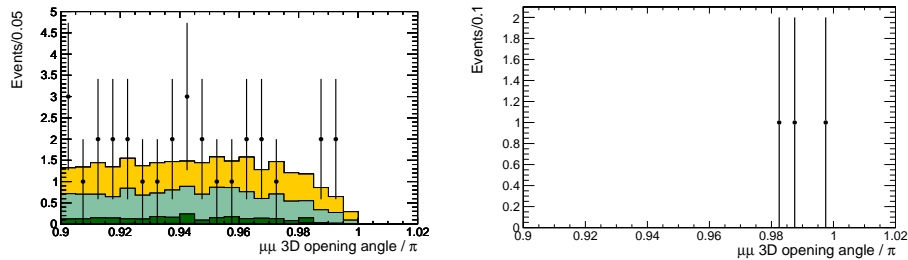


Figure 7.9: Left: tail of the three-dimensional dimuon opening angle in data and simulation. Right: three-dimensional opening angle for events failing the nominal vertex transverse position selection.

in data and simulation for all events having a three-dimensional opening angle greater than  $0.95\pi$ . We conclude that no systematic error needs to be assigned to the  $3D$ -

<sup>1</sup>The 3D-opening angle is defined as the arcsine of the scalar product of the muon momentum vectors

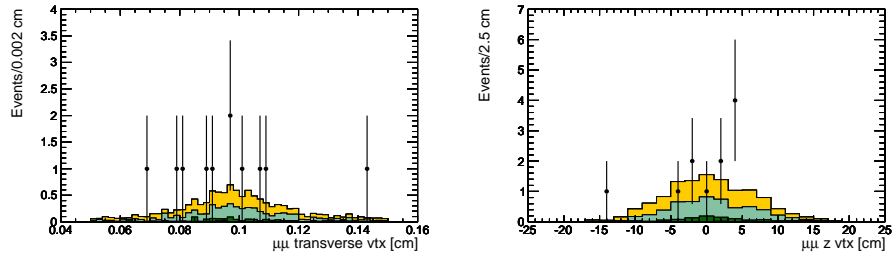


Figure 7.10: Left: Dimuon vertex transverse position for all events with three-dimensional opening angle  $> 0.95\pi$ . Right: Dimuon vertex  $Z$  position for all events with three-dimensional opening angle  $> 0.95\pi$ .

opening angle cut.

As a similar check for contamination from halo muons is performed by applying the nominal analysis selection to events triggered with the BPTX\_OR. Within the limited statistics, zero event pass all the analysis selections.

### 7.3.8 Fit systematics

The overall systematic uncertainty is evaluated by performing the fit with each variation applied individually. The relative difference with respect to the nominal fit is taken as a systematic.

Selection	Variation from nominal yield
track-distance < 1.0 mm	2.12%
track-distance < 3.0 mm	3.79%
high-purity tracks	0.10%
> 10 track hits	1.35%
high-purity with > 10 track hits	1.36%
Drell-Yan $\times 2$	0.39%
Drell-Yan $/2$	0.16%
double inelastic $\times 2$	0.99%
double inelastic $/2$	0.13%
Momentum scale	0.33%
Crossing-angle	0.96%
Tracking efficiency	0.14%
Vertexing efficiency	0.09%
Cow-boys veto	0.25%
Muon eff. variation	0.82%

Table 7.3: Variation in fitted signal yield.

For each variation, the largest relative difference with the nominal fit is taken as a systematic error. Summing quadratically all these contributions gives 4.375%.

## 7.4 Results and prospects

In officially recorded  $39.7 \text{ pb}^{-1}$  by the CMS detector in 2010, the measured ratio  $R$  of the  $pp \rightarrow p\mu^+\mu^-p$  yield to the LPAIR prediction in the kinematic region  $p_T(\mu) > 4 \text{ GeV}$ ,  $|\eta| < 2.1$  is

$$R = 0.822_{-0.131}^{+0.140}(\text{stat.}) \pm 0.036(\text{syst.}) \pm 0.040(\text{lumi.}) \quad (7.2)$$

taking the uncertainty on the delivered luminosity apart. Turning this result into a luminosity measurement would give:

$$\int \mathcal{L} dt = 32.62_{-5.20}^{+5.56}(\text{stat.}) \pm 1.43(\text{syst.}) \text{ pb} \quad (7.3)$$

Because of the strong correlation of the statistical error with the uncertainty on the inelastic yield  $N$ , the value for the absolute luminosity is measured to be between 63% and 101% for the  $1\sigma$  contour of  $N$ . In particular, the highest value is obtained for a inelastic yield ratio with LPAIR prediction of  $\sim 60\%$ .

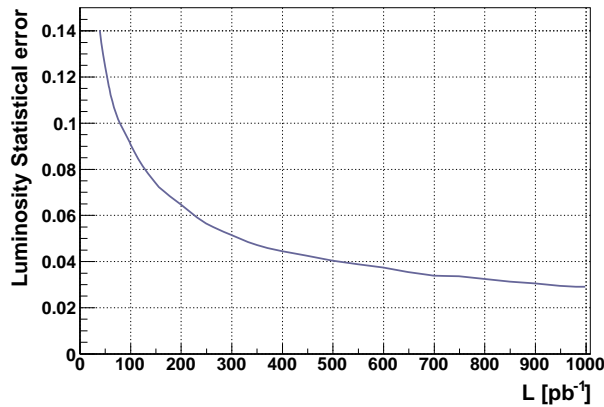


Figure 7.11: Evolution of the statistical error on the luminosity correction fitted value with respect to the true luminosity.

Assuming the same fitting procedure, the evolution of the statistical error on the luminosity correction value has been derived from fit results on pseudo-data built with known true luminosity. Obviously, identical performances for triggering, tracking and pileup rejection than obtained in 2010 have been assumed. The result is shown in

Figure 7.11 for integrated luminosity up to  $1 \text{ fb}^{-1}$ , where the method seems to reach a minimum of  $\sim 3\%$  precision on the statistical uncertainty.

However, with higher statistics than available in 2010 runs, different methods of signal extraction can be thought as multi-dimensional fit ( $\Delta\phi, \Delta p_T, p_T(\mu\mu)$ ), or a reweighting of the inelastic background with the mass of the proton remnant.

Systematic uncertainties are also assumed to shrink with accumulated integrated luminosity, as most of them (tracking, vertexing, energy scale, ...) are derived from the data directly. Similarly the largest uncertainty, which is coming from track-quality and veto-size variations, could be better controlled by applying dynamic cut based on the event-by-event position resolution and  $\chi^2$  of the vertex and tracks.





## **Part IV**

# **The look forward**



## Chapter 8

# Two-photon exclusive production of supersymmetric pairs

*“Supersymmetry is a concrete sound bridging the gap  
between silence and noise that can only be picked up  
under immense concentration”*

Critics of album 'Supersymmetry' from band 'Underwater Getdow'

Two-photon production of charged supersymmetric pairs has a clean and unique signature of 2 forward scattered protons, 2 opposite sign leptons and large missing energy (8.1). Consequently, search for supersymmetry through two-photon channels has the advantage to propose a simpler event topology and cleaner final states than other SUSY searches in  $pp$  collisions at the LHC which have to deal with complex cascade decay chains containing several types of unknown particles. This vantage has already been pointed out by Ohnemus, Walsh and Zerwas in 1993 in [22], where they first proposed to search for non-strongly interacting SUSY particles in  $\gamma\gamma$  collisions. However, authors did not discuss the experimental aspects linked to the detection of such events.

An exploratory study has therefore been performed at the generator level, with realistic acceptance cuts applied for the central and forward detections. It aimed to determine if these processes could be visible and to quantify the benefits associated to the detection of the forward protons in HPS.

For low-mass SUSY scenarios, significant cross-sections are expected and background processes are well controlled. Measurements of the forward proton energies would allow for a precise mass reconstruction of the lightest SUSY particle and right-handed sleptons (8.3.1, 8.3.2, 8.4) with a few GeV resolution. Methods to reduce backgrounds at high luminosity resulting from accidental coincidences between central and forward detectors are discussed in 8.5.

## 8.1 Two-photon production of SUSY pairs

The two-photon production of pairs of charged massive particles offers an interesting potential for the search of 'beyond the Standard Model' (BSM) particles. The production cross-section for charged pairs is displayed in Figure 2.7 as a function of the particle mass for different spin states. The photon fluxes parameterization with the Equivalent Photon Approximation, as discussed in Section 2.2, can be successfully used for the physics cases developed below, and therefore the rate of produced particles at the LHC can be well predicted. For instance, the cross-section for the (elastic-elastic) production of scalars, fermions and vector pairs of 100 GeV is 0.7 fb, 4.1 fb and 52.0 fb respectively for  $\sqrt{s} = 14$  TeV. The survival probability, which is assumed to be large for two-photon interactions as argued in Section 2.2, is taken to be 100% for the next studies.

Supersymmetry, as it predicts new scalar and fermionic particles above the electroweak scale, is therefore an excellent candidate for novel and complementary searches in  $\gamma\gamma$  interactions at the LHC. Because of the relative low cross-sections for these processes, it requests large integrated luminosity to obtain a significant amount of statistics. With the LHC nominal plans, that also means that this analysis has to be performed at the design luminosity, when the mean number of pileup events per bunch-crossing becomes of significant concern. However, thanks to striking experimental signatures, backgrounds are expected to be quite low and well under control.

The relevant Feynman diagrams for the two-photon production of slepton and chargino pairs are shown in Figure 8.1. In order to ensure the cleanest event signature, only the fully leptonic final states are considered in the following. With the techniques of selection for exclusive events developed in Chapter 5 for dileptons and the successful application to the  $\gamma\gamma \rightarrow \mu^+\mu^-$  process in Chapter 6, we ensure that the exclusive dilepton final states are selected with high-efficiency.

As it is shown in the same Figure, supersymmetric final states are also characterized by the presence of large missing energy, which is carried out by the neutrinos and

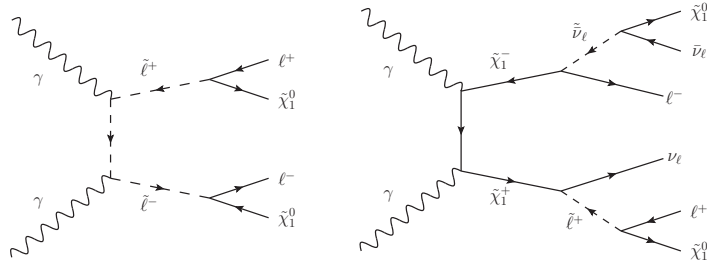


Figure 8.1: Relevant Feynman diagrams for the two-photon production of slepton pairs (left) and charginos pairs (right), with 2 leptons final state.

neutralinos which escape the detector without being detected. Of course, even though SUSY is taken as main framework to perform the analysis, similar final states can also be obtained in other BSM theories as in two-higgs doublet models, or with heavy stable charge particles, . . . Therefore, the supersymmetric choice has to be understood as an academic case to display the power of the method, which can be extended to any 'new physics' signal sharing similar characteristics. In order to have a framework of realistic physics case, the study has been performed for a specific benchmark point, usually referred to as the LM1 point in the literature.

The MSSM parameters, together with the associated production cross-sections, are detailed in Appendix C. The relevant contribution to the exclusive dilepton signal comes from the two-photon production of right-handed slepton pairs, for a total of 0.8 fb, which is 140 times smaller than the SM  $\gamma\gamma \rightarrow W^+W^-$  process. The simulation of the exclusive states has been performed using the calcHEP Monte-Carlo generator, and then passed to Pythia where the decay and hadronisation steps were performed.

## 8.2 Detection of exclusive SUSY pairs

The requested final state, that is applied in for this LM1 study but could be generalized to any low-mass SUSY scenarios with low- $\tan(\beta)$ , involves

- 2 leptons of opposite charge within CMS acceptance,
- 2 forward scattered protons hits in HPS,
- missing energy

The only irreducible background process for this event topology is the exclusive two-photon production of pairs of  $W$  bosons. The cross-section for two-photon production of  $W^+W^-$  with fully leptonic decay reaches almost 7 fb.

The direct lepton pairs two-photon production  $pp(\gamma\gamma) \rightarrow p\ell^+\ell^-p$  (with  $\ell = e, \mu, \tau$ ) can be easily suppressed by requiring large acoplanarity and/or large missing energy. For the final figures as well as in Table 8.1, the reverse of cuts used in the exclusive dimuon selection have been applied:

$$|(\phi(\ell^+) - \phi(\ell^-))/\pi| < 0.9, \quad |p_T(\ell^+) - p_T(\ell^-)| > 1.5 \text{ GeV} \quad (8.1)$$

Assuming a LHC multi-purpose detector like CMS, the following cuts have been applied on the leptons in order to simulate the acceptance region of the central detector:

$$p_T(e^\pm) > 10 \text{ GeV}, \quad p_T(\mu^\pm) > 7 \text{ GeV}, \quad |\eta(\ell^\pm)| < 2.5, \quad (8.2)$$

which are expected threshold for lepton pair triggering at high luminosity. The lepton energy and momentum scales are supposed to be precisely known at that point, such that null  $p_T$  resolution will be assumed in the next.

Protons have been transported through the beamline using the HECTOR software with same beam optics and same station locations and distances-to-beam (2.5 mm for HPS-240, 4 mm for HPS-420) than for the results of Section 4.3. The efficiency of detecting both forward protons (among those with detected central activity) is then around 74%, so almost the whole relevant photon spectrum is probed.

The expected rates of events within  $100 \text{ fb}^{-1}$ , with 2 detected leptons with/without doubly-tagged requirement are indicated in Table 8.1 for the signal and  $W^+W^-$  background. Because the branching ratio  $BR(\tilde{\ell}^+ \rightarrow \ell^+ + \tilde{\chi}_1^0) \simeq 100\%$ , selectron and smuon pairs are the major expected contribution in the analysis of dileptonic final states. In addition, almost 65% of right sleptons and 75% of left ones fall within the acceptance window. On the contrary, pairs of charginos have other significant decay modes (including hadronic decays) therefore only 7% of the produced chargino pairs will be detected. Staus, since they decay into tau leptons, will produce mostly two  $\tau$ -jet final states, hence only 1 and 6% of the  $\tilde{\tau}_1$  and the  $\tilde{\tau}_2$  pairs pass acceptance cuts, respectively. Finally, no relevant signal of the charged Higgs boson pairs can be seen, since  $H^+ \rightarrow \bar{b}t$  is the dominant decay mode.

The signal to noise ratio, although it already reaches a value close to 1/5 after lepton acceptance, can be improved considering only same flavor dileptonic events. Indeed,

because the signal is dominated by  $\tilde{\ell}_R$  and  $\tilde{\ell}_L$  pair decays, around 90% of the LM1 events is composed of  $e^+e^-$  and  $\mu^+\mu^-$  leptons. At the same time the background  $W$  pairs are suppressed by a factor 2 by selecting same flavor leptons.

Similarly, as the LM1 benchmark point doesn't stand in the high  $tg(\beta)$  region where couplings to (s)taus are enhanced, one can reject events with leptons from  $\tau$  decays on a displaced vertex veto. A conservative value of 1 mm transverse displacement with respect to the beamline has been assumed such that, at the generator level, 66% of the leptons from tau decays are flagged as displaced.

The lepton transverse momentum spectrum of events with central plus forward detections is also shown on Figure 8.2 for the events passing the lepton acceptance cut, the same flavor requirement and the  $\tau$ -veto. One can notice that the lepton energies are significantly larger than the ones involved in the  $pp(\gamma\gamma) \rightarrow p\mu^+\mu^-p$  analysis, with a maximum around 15 GeV. That also shows that, even for low-mass SUSY scenario, a stronger cut on the  $p_T$  would not affect the triggering efficiency dramatically.

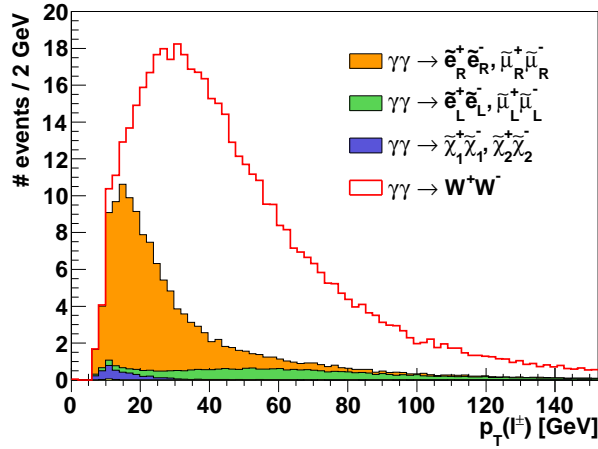


Figure 8.2: Transverse momentum spectrum for the signal (stack histogram) and the background separately, assuming an integrated luminosity of  $100 \text{ fb}^{-1}$ . Events passing the lepton acceptance and with doubly-HPS tag are considered.

### 8.3 Very forward detector information

In contrast to the nominal  $pp$  studies which can only use kinematical quantities measured with the central tracker, calorimeters and the muon system, the main experimental advantage of the two-photon processes relies on the detection in HPS of the two forward scattered protons. Indeed, beyond simply tagging exclusive interactions by looking at coincident signals on both sides of the IP in HPS, measurement of the proton energy in the forward detector –and hence the reconstruction of the proton energy lost and the photon energies– is a unique and precise tool to derive the initial conditions of the event. In nominal  $pp$  interactions, as the proton remnant is emitted at small angle and hence undetectable, the initial energy and momentum of the incoming partons remain unknown.

For tagged protons, the photon energy reconstruction is assumed to be performed with a resolution of

$$\sigma(E_\gamma) = \max(E_\gamma/100, 1.5 \text{ GeV}) \quad (8.3)$$

for all protons, following the results obtained in [81].

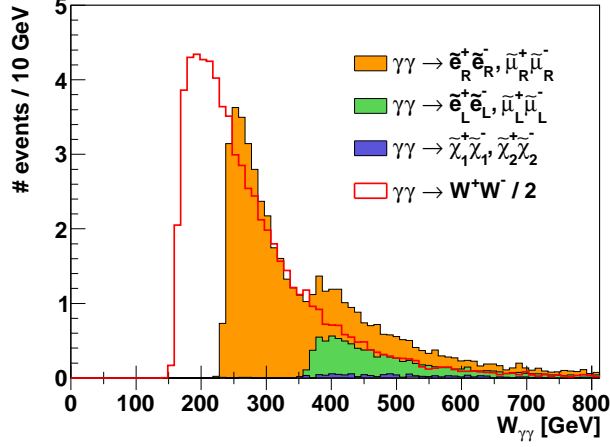
#### 8.3.1 Two-photon invariant mass reconstruction

The first obvious useful quantity reconstructed from the two photons energy to discriminate between the signal and background is the two-photon 'initial conditions' of the event:

$$W_{\gamma\gamma} = 2\sqrt{E_{\gamma_1}E_{\gamma_2}} \quad (8.4)$$

where  $E_{\gamma_1}$ ,  $E_{\gamma_2}$  are the reconstructed energies of two colliding photons. Expected distribution is shown in Figure 8.3 for  $L=100 \text{ fb}^{-1}$ . One can see two significant peaks due to the production thresholds of right slepton (around 250 GeV) and of left sleptons (around 400 GeV) for the LM1 case. In this way, the slepton mass spectrum can be probed by measuring the threshold energy for each peak, which is approximately equal to the sum of masses of the two produced sparticles. It should be stressed that the mass determination in this method depends only on the HPS energy resolution, and not on the resolutions of the central detectors. Actual precision of  $\tilde{\ell}_R^\pm$  and  $\tilde{\ell}_L^\pm$  mass determination is then mostly driven by available statistics.

Moreover, this quantity can also be used to suppress the background since the  $W_{\gamma\gamma}$  shape distribution for  $W$  pairs is well known and starts at about  $2m_W$ . The choice of

Figure 8.3: Two-photon invariant mass reconstruction for  $100 \text{ fb}^{-1}$ .

the analysis cut  $W_{\gamma\gamma}^{\text{min}}$  could be then changed along the LHC running period according to the SUSY mass constraints coming from nominal  $pp$  studies.

### 8.3.2 Missing mass reconstruction

Informations from both central and forward detectors can also be combined to extract the mass of the LSP. Indeed, the missing energy carried away by the neutrinos and the neutralinos can be estimated as

$$E_{\text{miss}} = E_{\gamma_1} + E_{\gamma_2} - E_{l_1} - E_{l_2} \quad (8.5)$$

where  $E_{l_1}$ ,  $E_{l_2}$  are the measured leptons energies. A conservative correction is made to account for the *bremsstrahlung* in electronic decays. It is assumed that the soft bremsstrahlung photons,  $p_T(\gamma) < 10 \text{ GeV}$ , are not detected. This results in the biased  $E_{\text{miss}}$  in a small fraction of events, but otherwise leptons are very well reconstructed in the central detectors. Therefore, as it is assumed that the energy and momentum of the leptons are known exactly, the resolution of the reconstructed kinematical variables is dominated by the photon energy resolutions in HPS.

The missing invariant mass distribution can then be defined as

$$W_{\text{miss}} = \sqrt{E_{\text{miss}}^2 - P_{\text{miss}}^2} \quad (8.6)$$

where  $P_{miss}$  is the event missing momentum and is calculated in analogy to  $E_{miss}$ . Missing mass is on average larger for the SUSY event sample since a supersymmetric event will always produce at least two massive LSPs. This can be seen in figure 8.4 where the expected distributions of  $W_{miss}$  for  $100 \text{ fb}^{-1}$  is shown.

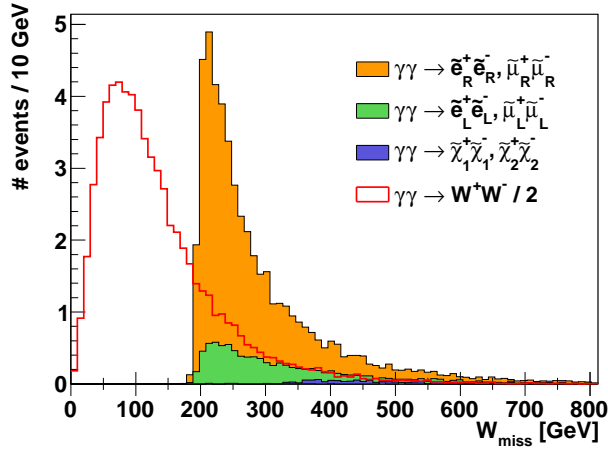


Figure 8.4: Two-photon missing mass reconstructed with  $100 \text{ fb}^{-1}$ .

SUSY distribution is peaked slightly above 200 GeV, which is twice the mass of the lightest neutralino in this model, while it starts at zero for the SM contribution. This quantity allows for measuring the LSP mass with a high resolution by performing a mass edge study. It also provides a powerful tool to suppress the  $W^+W^-$  background by requiring a  $W_{miss}^{min}$  cut.

### 8.3.3 Significance

Applying the following analysis cuts driven by the prior studies:

- acceptance cuts (8.2),
- same flavor lepton selection,
- $\tau$ -flagged rejection,
- $W_{\gamma\gamma} > 235 \text{ GeV}$  and  $W_{miss} > 195 \text{ GeV}$ ,
- lepton pairs acoplanarity and unbalanced  $p_T$  (8.1),

one reaches a  $S/B$  ratio close to 1.5. The various contributions for the signal are given in Table 8.1 for the integrated luminosity  $L = 100 \text{ fb}^{-1}$ , and  $S \simeq 36$  and  $B \simeq 25$  events.

<b>Process</b>	$\ell^+\ell^-$	$pp$	$W^{miss}$	$\Delta\phi/\pi$
	selection	selection	& $W_{\gamma\gamma}$	& $\Delta p_T$
$pp(\gamma\gamma) \rightarrow p\tilde{\mu}_R^+\tilde{\mu}_R^-p$	28.40	21.79	21.51	15.81
$pp(\gamma\gamma) \rightarrow p\tilde{e}_R^+\tilde{e}_R^-p$	23.78	18.21	17.98	12.81
$pp(\gamma\gamma) \rightarrow p\tilde{\mu}_L^+\tilde{\mu}_L^-p$	6.76	4.14	4.12	3.31
$pp(\gamma\gamma) \rightarrow p\tilde{e}_L^+\tilde{e}_L^-p$	6.51	4.10	4.07	3.35
$pp(\gamma\gamma) \rightarrow p\tilde{\tau}_1^+\tilde{\tau}_1^-p$	0.06	0.04	0.04	0.02
$pp(\gamma\gamma) \rightarrow p\tilde{\tau}_2^+\tilde{\tau}_2^-p$	0.06	0.04	0.04	0.03
$pp(\gamma\gamma) \rightarrow p\tilde{\chi}_1^+\tilde{\chi}_1^-p$	1.86	1.08	1.08	0.67
$pp(\gamma\gamma) \rightarrow p\tilde{\chi}_2^+\tilde{\chi}_2^-p$	0.42	0.09	0.09	0.08
$pp(\gamma\gamma) \rightarrow pW^+W^-p$	168.41	137.00	31.16	24.53

Table 8.1: Expected number of events for  $L = 100 \text{ fb}^{-1}$  after each selection step. Details on the cuts are in the text.

The  $5\sigma$  discovery for the LM1 left and right sleptons is then reached already after  $45 \text{ fb}^{-1}$  thanks to strong suppression of the irreducible background. It could still get better by using additional model-dependent cuts exploring  $\Delta\eta$  and  $\Delta R$  angles as it is done in [8], where the  $5\sigma$  is reached only after  $25 \text{ fb}^{-1}$ .

Finally, it could be improved even further by including the inelastic two-photon production, in this case however only one proton is detected and the kinematical reconstruction is not so effective. For the same benchmark point, the nominal proton-proton studies claim  $5\sigma$  discovery after about  $10 \text{ fb}^{-1}$  [106]. However, determination of particle masses in this case is much more complicated. Although this benchmark point has already been excluded by the first LHC data, the method remains valid for higher masses.

## 8.4 SUSY mass reconstruction

The main advantage of the two-photon analysis is large sensitivity to sparticle masses. However, the mass determination of  $\tilde{\ell}_R^\pm$ ,  $\tilde{\ell}_L^\pm$  and  $\tilde{\chi}_1^0$  using the production threshold values in  $W_{\gamma\gamma}$  and  $W_{miss}$  distributions is limited by the number of selected events. Another approach, based on other kinematic quantities, can provide a method to measure mass of the sleptons rather on an event-by-event basis.

The two-dimensional plots in Figure 8.5 represent event distributions on the  $W_{\gamma\gamma}$ ,  $W_{miss}$  plane for the MSSM processes and for the  $W^+W^-$  background, after acceptance cuts. One can observe that for the signal events these two variables are strongly correlated, and much less for the background. Moreover, it can be shown that the width of the distribution is related to the mass of the produced sparticles. This demonstrates a close relationship between the MSSM masses, the  $\gamma\gamma$  invariant mass and the missing mass. An empirical quantity has been built in order to take into account this observation:

$$(2m_{reco})^2 = W_{\gamma\gamma}^2 - ([W_{miss}^2 - 4m_{\tilde{\chi}_1^0}^2]^{1/2} + [W_{lep}^2 - 4m_{lep}^2]^{1/2})^2 \quad (8.7)$$

where  $W_{lep}$  is the invariant mass of the two lepton system, and  $m_{lep}$  is the lepton mass, and  $2m_{reco}$  is the reconstructed mass of the produced sparticles. It can be understood as the total available energy of the interaction on which we subtract the missing energy and the leptons energy, both corrected with mass of the produced states. That relation does not work well for  $\tilde{\tau}$  and  $\tilde{\chi}$  pairs because in general they decay into final states with more neutrinos and neutralinos. The only needed input in this method is the value of the LSP mass, which can be derived from the  $W_{miss}$  distribution.

The reconstruction power of this empirical quantity is illustrated in Figure 8.6 for the integrated luminosity  $L = 100 \text{ fb}^{-1}$ . A narrow peak centered at  $2m_{reco} = 236 \text{ GeV} = 2 \times 118 \text{ GeV}$ , allows for efficient and direct determination of the  $\tilde{e}_R^\pm$  and  $\tilde{\mu}_R^\pm$  mass. A second peak, centered at  $2m_{reco} = 370 \text{ GeV} = 2 \times 187 \text{ GeV}$ , with larger width, corresponds to  $\tilde{e}_L^\pm$  and  $\tilde{\mu}_L^\pm$  pairs but is not so well visible. Right selectron and smuon mass might be determined using this empirical method with a few GeV resolution.

## 8.5 Pileup effect

At the instantaneous luminosities at which this analysis has to be performed, the large number of extra overlap events leads to high probability to get accidental coincidence

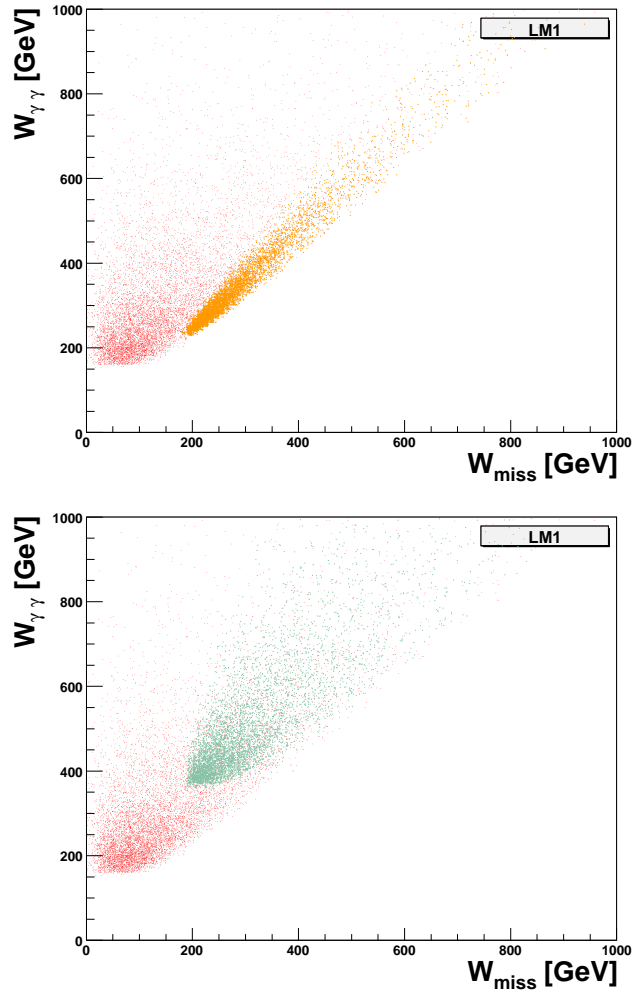


Figure 8.5: Scatter plots for the LM1 signal and the  $WW$  background on the  $W_{miss}, W_{\gamma\gamma}$  plane. Upper:  $\tilde{\mu}_R^+ \tilde{\mu}_R^-$  events (orange) and  $W^+ W^-$  events (red). Lower:  $\tilde{\mu}_L^+ \tilde{\mu}_L^-$  events (green) and  $W^+ W^-$  events (red).

background when a dileptonic event detected in the central CMS sub-detectors and the two forward scattered protons in HPS don't come from the same interaction. From detailed studies in Section 4.4, the associated probability to have 2 accidental proton hits in HPS per beam crossing is at the level of 1.32% and 24.59% for 'low' and 'high' luminosity respectively, if one sums contribution from  $[p][X][p]$  and  $[pp][X]$  in equa-

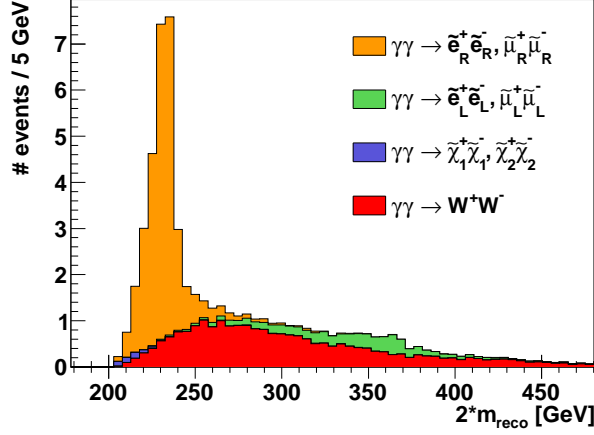


Figure 8.6: Reconstructed  $2 m_{reco}$  variable for the LM1 benchmark point and  $L = 100 \text{ fb}^{-1}$ .

tions 4.8 and 4.9.

The considered inclusive processes with dileptonic final states, likely to mimic an exclusive SUSY signature if HPS hits match, are the inclusive boson pairs production  $pp \rightarrow W^+W^- \rightarrow \ell^+\ell^- \nu s$ ,  $pp \rightarrow ZZ \rightarrow \ell^+\ell^- + jets$  and the inclusive Drell-Yan  $pp \rightarrow Z/\gamma^* \rightarrow \ell^+\ell^-$  processes, for which production cross-sections reach  $7.4 \cdot 10^3 \text{ fb}$ ,  $1.1 \cdot 10^4 \text{ fb}$  and  $1.3 \cdot 10^7 \text{ fb}$  respectively. The expected number of dileptonic events after applying the same lepton selection than for SUSY search (opposite sign, same flavor,  $\tau$ -veto and within  $p_T$ ,  $\eta$  acceptance) is shown in first column of Table 8.2 and has to be compared with values from Table 8.1 for the SUSY signal.

As the dominant component of inclusive dilepton is coming from Drell-Yan processes, analysis selection with pileup includes cuts on  $p_T^{miss}$  and on  $W_{lep}$ , both built from the leptons kinematics information in order to reduce the ' $\gamma^*$  part' and the ' $Z$  part' of the spectrum respectively. The considered cuts for Drell-Yan veto in the next will be set as

$$P_T^{miss} > 10 \text{ GeV}; \quad W_{lep} \notin [87 \text{ GeV}; 95 \text{ GeV}] \quad (8.8)$$

which will remove approximately 60% of the remaining Drell-Yan events while keeping 93% of the SUSY signal.

<b>Process</b>	$\ell^+\ell^-$ selection	track exclusivity	$pp$ selection	$W^{miss}$ & $W_{\gamma\gamma}$	$\Delta\phi/\pi$ & $\Delta p_T$	Drell-Yan veto
$pp \rightarrow Z/\gamma^*$ (low PU)	208M	43k	531.95	201.85	55.39	21.38
(high PU)			10.6k	4035.40	1107.43	427.52
$pp \rightarrow ZZ$ (low PU)	87k	25.62	0.32	0.08	0.06	0.02
(high PU)			6.30	1.69	1.19	0.48
$pp \rightarrow W^+W^-$ (low PU)	100k	40.47	0.50	0.15	0.11	0.11
(high PU)			9.95	2.97	2.29	2.16

Table 8.2: Expected number of events for  $L = 100 \text{ fb}^{-1}$  after each selection step. Details on the cuts are in the text.

This accidental coincidence background can be reduced at higher level trigger stage using kinematic constraints as consistency between the central and the forward systems in rapidity and mass. It can be further reduced using the fact that in general the number of tracks associated to the dilepton vertex is much smaller in exclusive events than in generic collisions, and used similar methods for selecting exclusive processes as the ones developed in Section 5.3. The performances of the two-tracks vertexing and the extra -track veto has proved to work in pileup conditions through the measurement of the  $pp(\gamma\gamma) \rightarrow p\mu^+\mu^-p$  process.

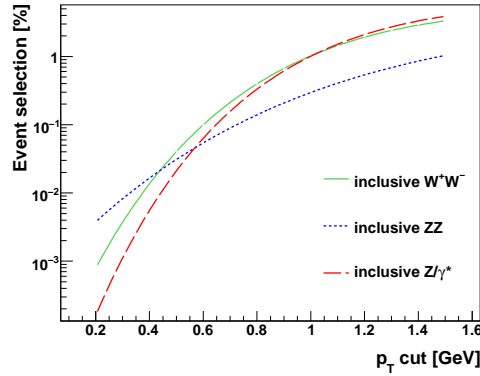


Figure 8.7: Background selection efficiency or 'no extra track with  $p_T > p_T$ ' cut condition

For illustration, track-based exclusivity conditions inefficiency is shown in Figure 8.7 as a function of the minimum  $p_T$  value for track reconstruction. The high performance of the central tracking detector to reconstruct tracks even at low  $p_T$  has been proved in Figure 5.9. One can notice that additional tracks within the 2 mm veto size around the exclusive vertex are reconstructed down to  $\sim 100$  MeV. To keep a conservative value of a 100% track reconstruction efficiency, we request no extra track to the  $\ell^+\ell^-$  vertex with  $p_T > 0.5$  GeV. No veto-size is applied as, at generator-level, all the particles arise from the same point. With  $p_T > 0.5$  GeV, the extra track veto method provides a reduction factor around 2500 for inclusive  $WW$ , 3000 for inclusive  $ZZ$  and 4500 for Drell-Yan production. However, it has to be emphasized that these reduction factor are strongly dependent on the Multiple Parton Interaction model used, and then have large uncertainty of factor 2.

The effect of the accidental coincidence background with track-based exclusivity conditions only is shown in top row of Figure 8.8 for low and high luminosities. For the lower one, the inclusive background remains on an acceptable level, so that  $\tilde{e}_R^\pm$  and  $\tilde{\mu}_R^\pm$

masses could still be reconstructed with a few GeV resolution (top left). However, in case of high luminosity, the probability to have a central dileptonic event accidentally associated to HPS hits is so large that peak signal from exclusive supersymmetric pairs is hidden (top right).

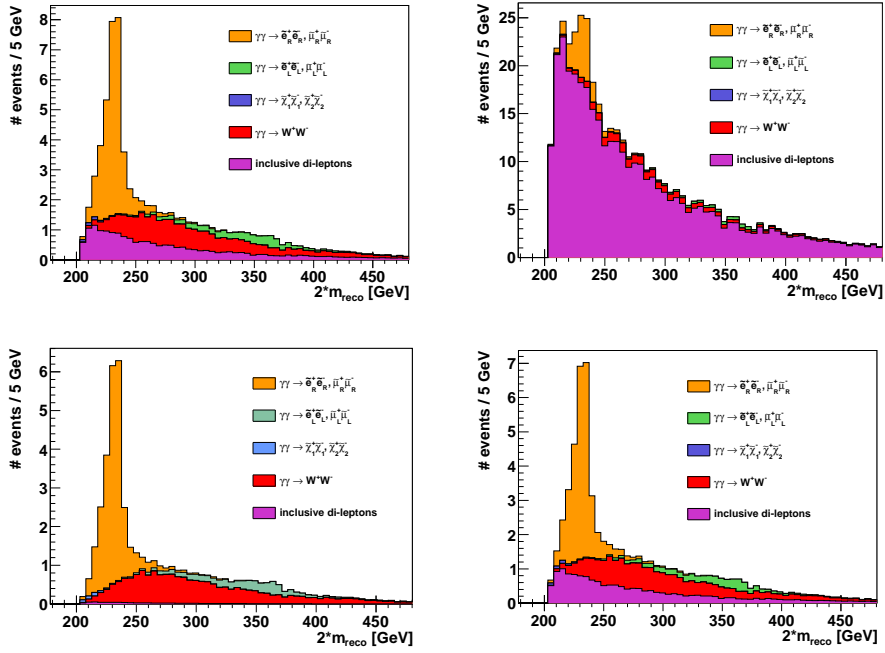


Figure 8.8: Reconstructed  $2 m_{reco}$  variable for different pileup environment. Left:  $= 2 \cdot 10^{33} \text{cm}^{-2} \text{s}^{-1}$ , Right:  $= 10^{34} \text{cm}^{-2} \text{s}^{-1}$ . Top: track-based exclusivity conditions, Bottom: track-based exclusivity conditions plus forward-central vertices matching requirement.

For such harsh environment conditions, precise time-of-flight detectors with few pico-second resolution have to be installed in association to the proton detector aiming to measure the relative time of arrival of protons at each stations  $t_L$  and  $t_R$ . With the  $z$ -by-timing method, the vertex position of an hypothetical events with triple coincidence can be reconstructed as

$$z_{pp} = \frac{1}{2}(t_L - t_R) \times c \quad (8.9)$$

and should match with the central vertex reconstructed within CMS for a real exclusive event. On the contrary, for overlap background events, the position measurements of forward and central vertices disagree for a large majority of them (see Section 4.4).

Such high background suppression is only possible if proton time of arrival measurement is performed with very-fast detector. Indeed, from a timing resolution of 10 ps on single proton measurement, the  $pp$  vertex position is reconstructed with a 2 mm uncertainty. So fast detector is already available, as the current prototypes of GASTOF showed a resolution of 10 ps during test beam.

Thus, assuming a timing resolution of 10 ps, and a vertex window size of  $1.5\sigma_{pp} \simeq 3$  mm, the corresponding matching efficiencies from Table 4.2 have been applied to the signal and the inclusive overlap background, and expected distributions are displayed on bottom row of Figure 8.8. The large overlap background suppression from vertices matching requirement is very powerful to get the SUSY signal well visible in the spectrum.

## 8.6 Summary and prospects

The present study, although it was restricted to a specific benchmark point, can be generalized to any other point of the MSSM plane or to any search of BSM charged particles. The only limitation to the method is the amount of statistics which will be collected at the LHC, otherwise it can be used for any considered BSM spectrum. As an example, three other benchmark points with different topology are briefly considered:

### LM3-like benchmark

For this point and in the region around  $m_0 = 330$  GeV,  $m_{1/2} = 240$  GeV, the exclusive supersymmetric signal is supposed to be dominated by the production of charginos ( $\sigma(pp(\gamma\gamma) \rightarrow p\tilde{\chi}_1^+\tilde{\chi}_1^-p) \simeq 0.649$  fb), decaying with the same branching ratios than the  $W^+$  ( $\mathcal{B.R.}(\tilde{\chi}_1^+ \rightarrow \ell^+\tilde{\chi}_1^0) = 31.5\%$ ). Therefore, SUSY searches with fully leptonic final states with same and different lepton flavor final states can be performed. In addition, the selection with different flavor would highly suppress the inclusive Drell-Yan background which will survive only through  $\gamma/Z \rightarrow \tau^+\tau^-$ .

### LM2-like benchmark

Within all the MSSM region around  $m_0 = 185$  GeV,  $m_{1/2} = 350$  GeV, the exclusive SUSY signal would also be composed of  $\tilde{\chi}_1^+\tilde{\chi}_1^-$  ( $\sigma = 0.144$  fb). However, as the point LM2 stands in a high- $tg(\beta)$  regime ( $tg(\beta) = 35$ ), the production of  $\tilde{\tau}_1^+\tilde{\tau}_1^-$  (0.166 fb) is contributing for roughly the same amount. Furthermore, the high- $tg(\beta)$  value enhances the couplings to tau and stau such that the phenomenology of the final states

is modified as  $\mathcal{B.R.}(\tilde{\chi}_1^+ \rightarrow \tilde{\tau}_1^+ \nu_\tau) = 95\%$  and  $\mathcal{B.R.}(\tilde{\tau}_1^+ \rightarrow \tau^+ \tilde{\chi}_1^0) = 100\%$ . Although dileptonic final states have been considered previously as to have the cleanest final state possible, one can also perform similar research for semi-leptonic or fully hadronic final states in the central detector. However, the exclusivity conditions are much difficult to establish. That would demand an extremely high accuracy to determine which tracks originating from the neighborhood of the vertex belongs to the jet, and which are due to proton remnants hadronisation or multiple parton interactions. . . with everything enveloped in high-pileup environment!

### Sweet-Spot

In addition, in some non-common SUSY theories, the LSP is not  $\tilde{\chi}_1^0$  as in MSSM but rather the gravitino. One interesting framework in which that occurs is the *Sweet Spot SUSY* [107], where the next-to-LSP is predicted to be the lightest tau  $\tilde{\tau}_1^+$ , with low mass around 116 GeV. It would be quasi-stable, with a decay time of  $\mathcal{O}(3000s)$ . Production of  $\tilde{\tau}_1^\pm$  pairs in photon-photon interactions will then be detected by observing very exclusive final states – two heavy and stable, opposite charge particles produced centrally plus two forward scattered protons. Using the phenomenological spectrum of [107], one finds the cross section for the two-photon  $\tilde{\tau}_1^+$  production of about 0.43 fb.

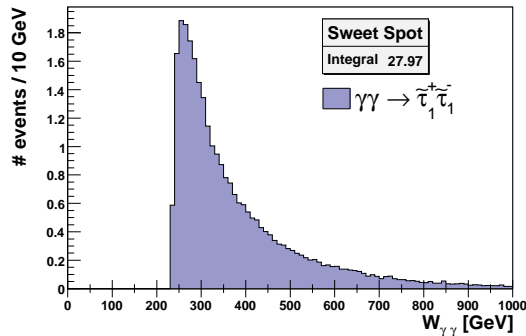


Figure 8.9: Photon-photon invariant mass distribution after the integrated luminosity  $L = 100 \text{ fb}^{-1}$  for  $pp(\gamma\gamma) \rightarrow \tilde{\tau}_1^+ \tilde{\tau}_1^- pp$  with  $p_T(\tilde{\tau}_1^\pm) > 10 \text{ GeV}$  requirement.

A usual method in  $pp$  studies to detect such heavy lepton like pairs relies on the use of the  $dE/dx$  variable, or time of flight measurements, and results in a poor reconstruction using calorimeters and muon chambers [108]. On the contrary, in the two-photon

analysis, almost all the kinematic information is available, again thanks to the detection of the forward scattered protons. For example, the two-photon invariant mass  $W_{\gamma\gamma}$  as shown in figure 8.9 for the integrated luminosity  $L = 100 \text{ fb}^{-1}$ , assuming detection if both staus with  $p_T(\tilde{\tau}_1^\pm) > 10 \text{ GeV}$ , and of two forward protons in the full HPS setup. The stau mass can then be directly measured by comparing the two-photon invariant mass with the stau momenta. Such a event-by-event measurement has a very good resolution, of about 5 GeV. Finally, the stau spin could be determined by analyzing the stau angular distributions in their center-of-mass reference system.

### Forward trigger

Another possible constraint for the nominal search with fully leptonic final state is the limited bandwidth for triggering low- $p_T$  lepton pairs. At  $\mathcal{L} = 10^{34} \text{ cm}^{-2} \text{ s}^{-1}$ , most of the  $L1$  bits will be probably used for BSM search in  $pp$  interactions, by requested high- $p_T$  jet and large missing energy signatures. Exclusive selection of leptons could therefore suffers from this limitation. However, two arguments may improve the situation. On the first hand, as it is shown in Figure 8.2, even low-mass SUSY scenarios are leading to relatively high lepton transverse momentum, such that one could imagine to trigger only lepton pairs with  $p_T > 20 \text{ GeV}$  without losing all the signal.

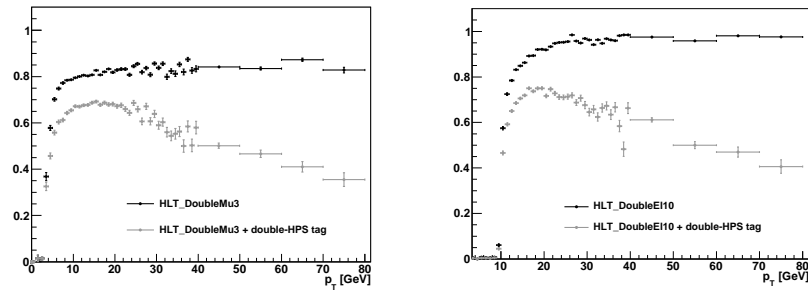


Figure 8.10: Triggering performance from HLT\_DoubleMu3 and HLT\_DoubleE110 computed with OpenHLT with/without double tag requirement as a function of the most energetic lepton of the pair.

On the second hand, with the future increase of the  $L1$  latency, one may even hope to have special triple coincidences trigger with the central detector and 240m stations. The effect of such a system is demonstrated in Figure 8.10, where the triggering efficiency is shown as a function of the most energetic lepton of the pair for two trigger

paths already existing in the current *HLT* menu<sup>1</sup>. The efficiencies have been computed using  $pp(\gamma\gamma) \rightarrow p\tilde{\ell}_R^+\tilde{\ell}_R^-p$  Monte-Carlo events generated at the LM1 point and information from HLT process. The simulation of the proton propagation in the beam-line is done with HECTOR assuming the usual set of forward detectors. The binning changes between  $p_T$  below 40 Gev ( $1 \text{ GeV}^{-1}$ ) and above ( $10 \text{ GeV}^{-1}$ ) due to statistics matter.

One can notice that up to  $p_T = 30 \text{ GeV}$ , the efficiency curves for the event tagged in HPS follow the ones with central detection only, with a difference of the order of 20% less due to intrinsic forward detector acceptance. After this threshold, the produced dileptonic events are usually too heavy to have their 2 forward protons tagged, and then efficiency starts to decrease.

## Summary

The first exploratory study of two-photon production of BSM pairs showed that interesting results can be extracted with significant statistics available, though the production rates are low relative to  $pp$  rates. As an academic example, the present study showed that for a signal cross-section 140 times smaller than the SM background (0.8 vs 108.5 fb), an efficient selection leads to a significant amount of exclusive signal over a largely-suppressed background. For higher mass searches, stringent cuts on  $W_{miss}$  and  $W_{\gamma\gamma}$  would compensate the decrease of expected signal rate.

It also proves that the insertion of a dedicated very-forward proton detection system, when accompanied with fast timing detectors, would bring valuable and accurate measurements of the BSM model properties, as the mass spectrum.

---

<sup>1</sup>HLT\_DoubleMu3 and HLT\_DoubleEle10



# Conclusion

Two-photon interactions at the LHC, although they suffer from relative low cross-sections, turn out to be an important physics channel to consider in order to achieve the CMS goal to probe various new sectors in physics. Expected rates and available  $\gamma\gamma$  energies allow for novel and unique measurements already at  $\sqrt{s} = 7$  TeV.

The first measurement of two-photon production at the with the CMS detector showed the feasibility to select effectively exclusive pairs even within pileup environment. With limited statistics, the exclusivity and kinematics selections demonstrated the capability to discriminate the elastic-elastic signal from other sources of (semi-exclusive and inclusive) dimuon events.

In particular, the application of track-based exclusivity conditions, which consist to veto events with any track originating from 2 mm around the dimuon vertex, proved to be an excellent alternative to the usual calorimeter veto in order to suppress inclusive events. Remaining background was separated from fitting the singular kinematical distribution of the  $p_T$  of the pair. Although it exists limited statistics in the side-band region which bring large uncertainty on the inelastic yield, an excellent agreement between data and the LPAIR predictions are observed when applying the best-fit values. That is the case for the single muon quantities ( $\phi$ ,  $p_T$ ,  $\eta$ ) as well as for muon pairs kinematics ( $p_T(\mu\mu)$ ,  $\eta(\mu\mu)$ ,  $\Delta p_T$ ,  $\Delta\phi$ , ...)

With additional events which will be recorded in 2011, a clearer modelling of the single-inelastic component will be possible. And hence, the total integrated luminosity could be measured with a few percent uncertainty only.

The observation of  $J/\Psi$  and  $\Upsilon$  photo-produced events also opens up the ability to measure exclusive vector meson cross-sections at an energy well above the HERA scale. Backgrounds still need to be understood, including the inelastic component and the contamination from central exclusive production of  $\chi$  states. In addition, for the

low-mass states, it also needs to come with an accurate simulation of the endcap region for the detection of low- $p_T$  muons.

The agreement between data and  $\gamma\gamma \rightarrow \mu^+\mu^-$  Monte-Carlo expectations also tends to promote this process to calibrate the future High Precision Spectrometer, aiming to detect forward scattered protons. The integration of such dedicated forward tracking system into the CMS trigger and reconstruction scheme would bring an enormous advantage to the two-photon physics. Since both hard scatter and outgoing protons would be detected, a useful set of extra information is available for physics analysis. For instance, for the two-photon production of supersymmetric pairs, the  $\gamma\gamma$  invariant mass and the missing mass distributions contain directly valuable information on the SUSY mass spectrum without recourse to complex analysis methods. Combination of both even leads to precise mass reconstruction of some SUSY particles on an event-by-event basis with a few GeV resolution.

Although the benchmark point studied has already been ruled out by the first 2010 data analysis, the method remains valid and extremely powerful to detect and measure two-photon production of more massive SUSY pairs, or any other 'new physics' signal produced exclusively. The only limitation comes from the statistics collected and the maximum photon energy tagging limited to  $\sim 700$  GeV.

With realistic physics case and LHC beam parameters, simulations show that contamination from accidental forward proton hits in coincidence with triggered event in the central CMS detector would contribute at a negligible level for relatively low pileup environment ( $\langle N \rangle \simeq 5$ ). Such suppression of the overlap background may be achieved using similar techniques of track-veto exclusivity conditions as the one developed in the  $\gamma\gamma \rightarrow \mu^+\mu^-$  analysis.

However, with the increase of luminosity, the rate of accidental triple coincidence background becomes so large that an extra technique of background suppression has to be added. Comparing the central vertex and the "pp" vertex reconstructed with  $z$ -by-timing method, it was demonstrated that roughly 95% of the overlap background are rejected through this method with a 10 ps resolution on proton time of arrival. Such precisions have already been achieved with GASTOF prototypes at recent Test Beam, and some improvements are yet possible (mirror beam wall, lens, etc.). The C++ simulation of the detector developed may be of help to search for the best design.

The study of two-photon interactions at the LHC brought me the opportunity to be in touch with various aspects of the modern high-energy physics. From the Monte-Carlo generation of these processes, with the complex simulation of the proton remnant hadronisation. Through the experimental characterization of the exclusivity conditions, dealing with standard high-level objects from the CMS reconstruction and with sub-detectors components. Also through the creation of an analysis code to effectively select events of interest among the huge amount of available data, by applying both purity and physics-motivated criteria. Finally, with the statistical treatment of these data and their interpretation. For the GASTOF project, I entered in the world of fast electronic, precision measurement and hardware R&D, which were far from my initial skills. In conclusion, a bit of everything . . .



## Appendix A

# Trigger muon paths

The HLT online muon selection is actually a chain composed of two different types of pieces: the muon reconstruction ones and the filter logic ones. The muon reconstruction is common to all paths containing muons and is performed, independently of the trigger path called, on all muon candidates (up to 4) which have passed an initial filter based on  $L1$  trigger info. The full  $HLT$  reconstruction processes in 5 steps:

1. seed creation from  $L1$  muon candidates
2.  $L2$  (stand-alone) muon reconstruction
3. calorimetric isolation
4.  $L3$  (global) muon reconstruction
5. tracker isolation

with a series of filters, specific to each path, placed among reconstruction steps to stop the trigger sequence if the muon candidates don't satisfy some given conditions.

The 3 double muon trigger paths used for the online selection are:

- `HLT_DoubleMu0`: Seeded by the  $L1$  bit `L1_DoubleMuOpen`, it requests at least two  $L3$  muons, without any  $p_T$  cut. Each  $L3$  muon is seeded by a  $L2$  muon, also without any  $p_T$  cut, and must be separated by at most 2 cm from the beam spot (in  $\Delta(XY)$ ).

- HLT\_DoubleMuOpen: Seeded by the *L1* bit `L1_DoubleMuOpen`, it requests a muon pairs without any further selection beyond *L1*.
- HLT\_DoubleMu3: Seeded by the *L1* bit `L1_DoubleMu3` (up to run 147116) or `L1_DoubleMuOpen` (from run 147196), it requests two *L3* muons with  $p_T > 3$  GeV. Each *L3* muon is seeded by a *L2* muon with  $p_T > 3$  GeV and must be separated by at most 2 cm from the beam spot (in  $\Delta(XY)$ ).
- HLT\_DoubleMu0\_Quarkonium\_v1: Available in the menu `2E32`, it similar to the `HLT_DoubleMu0` except that it triggers only on opposite sign muons, and for masses within  $1.5 < m < 14$  GeV.

At the boundary between Run2010A and Run2010B eras, a major modification was done in the reconstruction algorithm of the *L3* muons, therefore changing the name `HLT_DoubleMu3` to `HLT_DoubleMu3_v2`. In the first period, the *Outside – InState* algorithm was used, consisting in a usual propagation of the *L2* state to the outer tracker layer and the use of that seed for the tracker pattern recognition.

On the contrary, the "cascade" algorithm is an intelligent combination of the different *L3* seeders which work separately and sequentially: first the *Outside – InState* seed builder, then the *Outside – InHit* seed builder (use of the propagated *L2* state plus one hit to make the seed), and finally the *Inside – outHit* seed builder (use of pixel pairs or triplets in the tracking region around *L2* state as a seed). The cascade stops when one algorithm leads to a *L3* muon, otherwise goes to the next seeder. In 95% of the time, the cascade coincides with the *OIState* algorithm, but in 5% of failure the *OIHit* and *IOHit* are increasing the efficiency, especially for low- $p_T$  *L2* muons.

## Appendix B

# Ray Tracing plots

Technical plots, mainly dependence of reflection/refraction/transmission power with the incoming photon wavelength, are shown in Figures B.1 to B.7 as they are in use for the ray tracing simulation.

The distribution of proton initial positions is shown in Figure B.1 in 2 dimensionnal view. On the  $x$  axis, the origin  $x = 0$  stands on the position of the closest GASTOF wall to the beam, and corresponds to a beam-distance of 2.5 mm which is assumed for HPS-240 ( $z > 0$ ), *i.e.*  $x = 0$  on the plot corresponds to  $x = 2.5$  mm with respect to the LHC coordinates.

The refraction index of the  $C_4F_{10}$  gas running with the incoming proton energy is displayed in Figure B.2. It varies from  $n = 1.0017$  to  $1.0013$  in the energy regime of work.

The mirror reflectance is shown in Figure B.3 as a function of the photon wavelength, derived from "Optics for Reasearch" web data[109]. One can notice that the metallic front-surface mirror used has reflectance between 60% and 90% in the ultra-violet regime.

The lens transmission power from Figure B.4 has been derived from "Edmund Optics" web data[110]. The transmission is constant around 90% for the wavelengths under

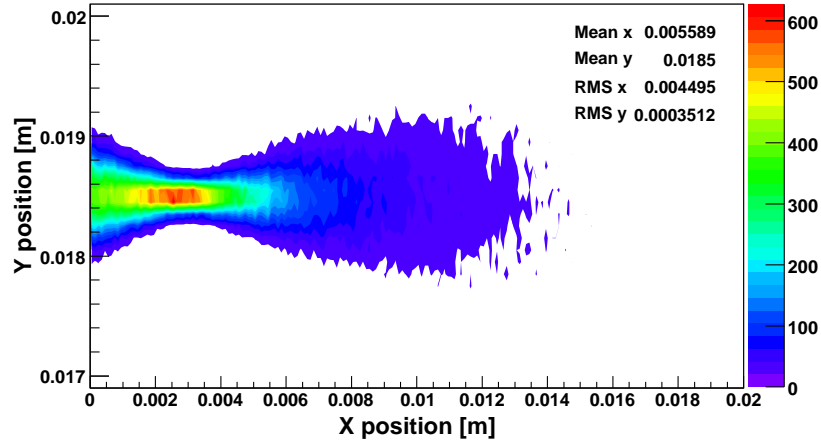


Figure B.1: Two-dimensionnal distribution of the proton entrance positions in GASTOF, derived from realistic scattered forward proton distributions from  $pp(\gamma\gamma) \rightarrow pW^+W^-p$  processes with protons detected on both sides and  $|\eta(X)| < 2.5$ .

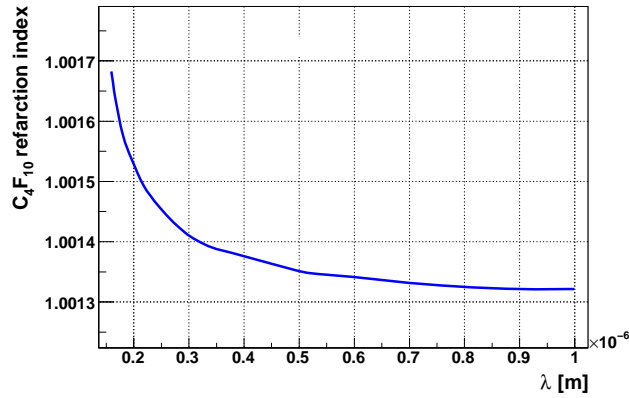


Figure B.2: Refractive index dependence of the  $C_4F_{10}$  gas with the wavelength.

consideration.

The quartz refractive index, which is used to simulated the time delay in the 3.2 mm quartz layer front of the photo-cathode, is shown in Figure B.5, derived from a for-

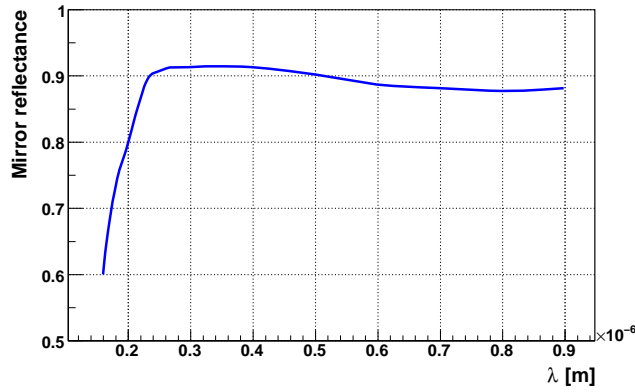


Figure B.3: Metallic Ultraviolet mirror reflectance dependence with the wavelength.

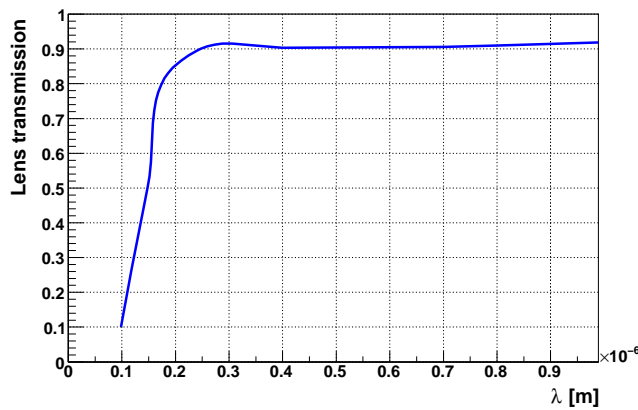


Figure B.4: Calcium Fluoride lens transmission dependence with the wavelength.

mula in [111].

The quantum efficiency of 2 tubes used in the prototypes, are displayed in Figure B.6 (right). One can notice a drop of the efficiency outside the  $\square$  nm range for the commonly used R3809U-50. The QE has been derived from the photo-cathode sensitivity taken from "Hamamatsu" web data [112] and displayed on the same figure.

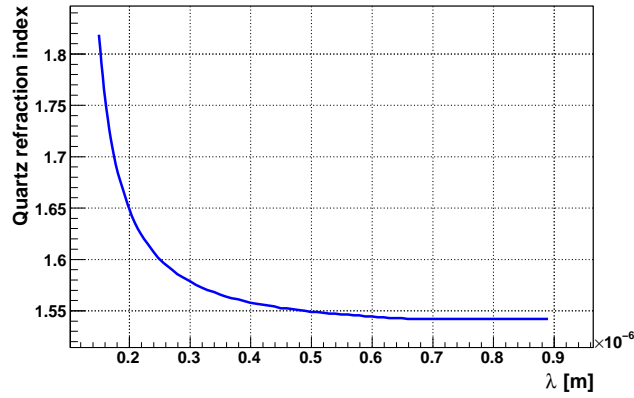


Figure B.5: Quartz refractive index dependence with the wavelength.

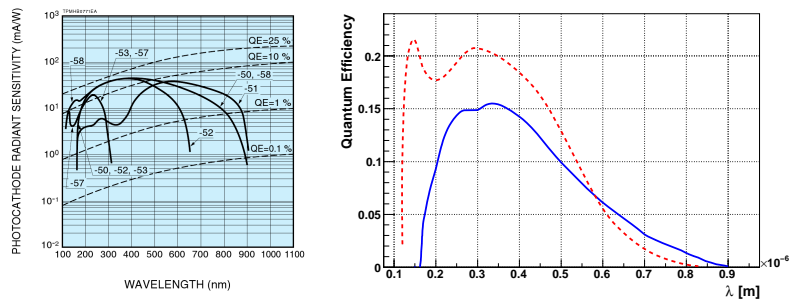


Figure B.6: Photo-cathode sensitivity and derived quantum efficiency for R3809U-50 (blue plain) and R3809U-58 (dash red) MCP-PMTs.

Finally, the single photo-electron response modelling has been taken from the Pulse Height distribution from Figure B.7 taken from [112].

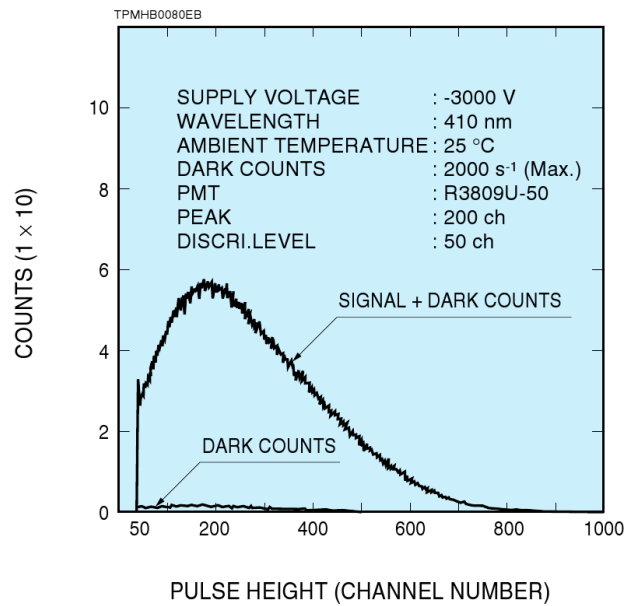


Figure B.7: Measured pulse-height distribution for single photo-electron signal.



## Appendix C

# The LM1 supersymmetric benchmark point

The MSSM parameters for the LM1 point considered in the analysis are the following:

$$m_0 = 60 \text{ GeV}, \quad m_{1/2} = 250 \text{ GeV}, \quad tg(\beta) = 10, \quad sign(\mu) = +1, \quad A_0 = 0;$$

and the corresponding masses of supersymmetric particles derived from running the renormalization group equations from parameters above are listed below, together with the cross-section value for two-photon production using the EPA:

• $m(\tilde{e}_R^\pm) = m(\tilde{\mu}_R^\pm) = 118 \text{ GeV}$	$\sigma(pp(\gamma\gamma) \rightarrow p\tilde{\ell}_R^+\tilde{\ell}_R^-p) = 0.399 \text{ fb}$
• $m(\tilde{e}_L^\pm) = m(\tilde{\mu}_L^\pm) = 187 \text{ GeV}$	$\sigma(pp(\gamma\gamma) \rightarrow p\tilde{\ell}_L^+\tilde{\ell}_R^-p) = 0.091 \text{ fb}$
• $m(\tilde{\tau}_1^\pm) = 111 \text{ GeV}$	$\sigma(pp(\gamma\gamma) \rightarrow p\tilde{\tau}_1^+\tilde{\tau}_1^-p) = 0.518 \text{ fb}$
• $m(\tilde{\tau}_2^\pm) = 190 \text{ GeV}$	$\sigma(pp(\gamma\gamma) \rightarrow p\tilde{\tau}_2^+\tilde{\tau}_2^-p) = 0.085 \text{ fb}$
• $m(\tilde{\chi}_1^\pm) = 178 \text{ GeV}$	$\sigma(pp(\gamma\gamma) \rightarrow p\tilde{\chi}_1^+\tilde{\chi}_1^-p) = 0.602 \text{ fb}$
• $m(\tilde{\chi}_2^\pm) = 360 \text{ GeV}$	$\sigma(pp(\gamma\gamma) \rightarrow p\tilde{\chi}_2^+\tilde{\chi}_2^-p) = 0.041 \text{ fb}$
• $m(H^\pm) = 381 \text{ GeV}$	$\sigma(pp(\gamma\gamma) \rightarrow pH^+H^-p) = 0.041 \text{ fb}$

The Lightest Supersymmetric Particle (LSP) in this model is the first neutralino  $\tilde{\chi}_1^0$  with a corresponding mass of 96 GeV.

The Pythia software was used to perform the decay and hadronisation steps. The dominant branching ratios for various SUSY states are listed in Table C.1.

Process	Branching Ratio	Process	Branching Ratio
$\tilde{\ell}_L^- \rightarrow \tilde{\chi}_1^0 + \ell^-$	91.82%	$\tilde{\tau}_2^- \rightarrow \tilde{\chi}_1^0 + \tau^-$	85.88%
$\tilde{\chi}_1^- + \nu_\ell$	5.53%	$\tilde{\chi}_1^- + \nu_\tau$	9.34%
$\tilde{\chi}_2^0 + \ell^-$	2.65%	$\tilde{\chi}_2^0 + \tau^-$	4.77%
$\tilde{\ell}_R^- \rightarrow \tilde{\chi}_1^0 + \ell^-$	100%	$\tilde{\chi}_1^+ \rightarrow \tilde{\tau}_1^+ + \nu_\tau$	46.44%
$\tilde{\tau}_1^- \rightarrow \tilde{\chi}_1^0 + \tau^-$	100%	$\tilde{\nu}_\tau + \tau^+$	19.01%
		$\tilde{\nu}_e + e^+$	17.03%
		$\tilde{\nu}_\mu + \mu^+$	17.03%
		$\tilde{\chi}_1^0 + W^+$	0.48%

Table C.1: Relevant decay processes for produced supersymmetric particles in the LM1 benchmark point.

# List of Figures

1.1	Correction to Higgs boson mass . . . . .	12
1.2	Evolution of the inverse of the gauge constants . . . . .	14
1.3	Higgs search in the SM . . . . .	15
1.4	CERN acceleration chain . . . . .	16
1.5	Inclusive event display . . . . .	18
1.6	SUSY limits in CMS . . . . .	19
2.1	$pp(\gamma\gamma) \rightarrow pXp$ process . . . . .	22
2.2	$pp(\gamma\hat{p}) \rightarrow pXN'$ and $pp(\gamma\mathbb{P}) \rightarrow pXp$ processes . . . . .	24
2.3	Diffraction vector meson photo-production measurements at HERA. . . . .	25
2.4	$pp(\gamma\gamma) \rightarrow pXN$ process . . . . .	28
2.5	Photon spectrum $dN/dx$ . . . . .	29
2.6	Relative and integrated photon-photon luminosity . . . . .	30
2.7	Two-photon pair production cross-sections . . . . .	32
2.8	LPAIR philosophy . . . . .	34
2.9	$\eta$ distribution of particles from proton dissociation . . . . .	35
2.10	$\eta_{min}$ vs. $m_N$ distribution of particles from proton dissociation . . . . .	36
2.11	Proton remnant visibility . . . . .	36
2.12	$pp(CEP) \rightarrow pXp$ process . . . . .	37
3.1	Total integrated luminosity . . . . .	44

3.2	CMS detector 3D view . . . . .	44
3.3	CMS detector 2D view . . . . .	46
3.4	Tracker cross-section . . . . .	48
4.1	Forward scattered proton paths . . . . .	62
4.2	HPS forward positions and angles . . . . .	64
4.3	HPS forward positions . . . . .	65
4.4	Forward scattered proton spectrum . . . . .	66
4.5	HPS acceptance . . . . .	67
4.6	HPS distance-to-beam effect . . . . .	68
4.7	HPS shadowing effects . . . . .	69
4.8	$\gamma\gamma$ luminosity with HPS acceptance . . . . .	70
4.9	Overlap background illustration . . . . .	71
4.10	MinimumBias proton spectrum . . . . .	73
4.11	$z$ -by-timing method . . . . .	76
4.12	Total path length for 2-HPS hits protons. . . . .	77
4.13	3D view of Gastof detector . . . . .	78
4.14	2D view of Gastof detector . . . . .	79
4.15	GASTOF event display . . . . .	82
4.16	Photon hits distribution on the photo-cathode . . . . .	85
4.17	Photo-electrons spectrum . . . . .	85
4.18	Cerenkov photons spectrum . . . . .	86
4.19	Time-of-flight . . . . .	87
4.20	Pressure dependence . . . . .	88
4.21	Beam Wall material . . . . .	89
4.22	Lens effect on photons spot . . . . .	90
5.1	$\eta_{min}$ distribution from proton dissociation . . . . .	97

5.2	Leading calotower energy . . . . .	98
5.3	99% noise rejection threshold . . . . .	99
5.4	Calorimeter exclusivity efficiency vs. instantaneous luminosity . . . . .	100
5.5	Low- $p_T$ track reconstruction efficiency . . . . .	101
5.6	Tracks-on-vertex multiplicity . . . . .	102
5.7	Track-veto exclusivity efficiency . . . . .	103
5.8	Track-veto exclusivity efficiency . . . . .	104
5.9	Extra track properties . . . . .	104
5.10	Exclusivity efficiency vs. Run number . . . . .	105
5.11	Exclusivity efficiency vs. bunch-crossing . . . . .	106
5.12	Exclusivity efficiency vs. instantaneous luminosity . . . . .	106
5.13	Exclusivity efficiency vs. vertex multiplicity . . . . .	107
6.1	Elastic, single and double-inelastic $\gamma\gamma \rightarrow \mu^+\mu^-$ processes . . . . .	110
6.2	$\gamma\gamma$ muon kinematics comparison. . . . .	111
6.3	$\gamma\mathbb{P} \rightarrow \Upsilon$ and $\chi_b$ CEP processes . . . . .	112
6.4	$\gamma\mathbb{P}$ muon kinematics MC comparison. . . . .	113
6.5	$\gamma$ energy in $\chi$ decay MC . . . . .	113
6.6	Exclusive event display . . . . .	116
6.7	Tag-and-Probe efficiency . . . . .	117
6.8	Observed $\gamma\gamma \rightarrow \mu^+\mu^-$ mass spectrum . . . . .	118
6.9	Observed $\gamma\gamma \rightarrow \mu^+\mu^-$ single muon rapidity . . . . .	119
6.10	Observed $\gamma\gamma \rightarrow \mu^+\mu^-$ single muon $p_T$ . . . . .	119
6.11	Observed $\gamma\gamma \rightarrow \mu^+\mu^-$ single muon $\phi$ . . . . .	120
6.12	Observed $\gamma\gamma \rightarrow \mu^+\mu^-$ muon pair $p_T$ and $\eta$ . . . . .	120
6.13	Observed $\gamma\gamma \rightarrow \mu^+\mu^-$ muon pair (N-1) $\Delta p_T$ and $\Delta\phi$ . . . . .	121
6.14	Observed $\gamma\gamma \rightarrow \mu^+\mu^-$ muon pair $\Delta p_T$ and $\Delta\phi$ . . . . .	121
6.15	Observed $\gamma\mathbb{P} \rightarrow \Upsilon$ mass spectrum . . . . .	122

6.16	Fit on the $\gamma\mathbb{P} \rightarrow \Upsilon$ mass spectrum . . . . .	123
6.17	Observed $\gamma\mathbb{P} \rightarrow \Upsilon$ muon pair $p_T^2$ and $\eta$ . . . . .	124
6.18	Observed $\gamma\mathbb{P} \rightarrow \Upsilon$ muon pair $\Delta p_T$ and $\Delta\phi$ . . . . .	124
6.19	Observed $\gamma\mathbb{P} \rightarrow \Upsilon$ muon pair 3D-angle and vertex position . . . . .	124
6.20	Observed $\gamma\mathbb{P} \rightarrow J/\Psi$ invariant mass . . . . .	127
7.1	Input data and MC templates for the fit . . . . .	133
7.2	Absolute resolution on $p_T(\mu\mu)$ , purity and stability vs. $p_T(\mu\mu)$ . . . . .	134
7.3	Best fit to the $p_T(\mu\mu)$ distribution. . . . .	135
7.4	1 and 2 sigma contours of fit parameters . . . . .	136
7.5	Fit stability . . . . .	140
7.6	Observed $\gamma\gamma \rightarrow \mu^- \mu^+$ muon pair $p_T$ in the sideband region . . . . .	141
7.7	Single and Double Pomeron Exchange processes . . . . .	142
7.8	SPE-DPE extra track multiplicity . . . . .	143
7.9	Cosmics check: opening angle . . . . .	144
7.10	Cosmics check: vertex . . . . .	145
7.11	Luminosity prospects . . . . .	147
8.1	$\gamma\gamma \rightarrow \tilde{l}^+ \tilde{l}^-$ and $\gamma\gamma \rightarrow \tilde{\chi}^+ \tilde{\chi}^-$ processes . . . . .	155
8.2	SUSY and background $p_T$ distribution . . . . .	157
8.3	SUSY and background $\gamma\gamma$ invariant mass . . . . .	159
8.4	SUSY and background missing mass . . . . .	160
8.5	SUSY and background $W_{\gamma\gamma}$ vs. $W_{miss}$ . . . . .	163
8.6	Reconstructed SUSY mass . . . . .	164
8.7	Track-based exclusivity efficiency . . . . .	166
8.8	Reconstructed SUSY mass with pileup . . . . .	167
8.9	$\gamma\gamma \rightarrow \tilde{\tau}_1^+ \tilde{\tau}_1^-$ invariant mass . . . . .	169
8.10	Triple coincidence trigger performance . . . . .	170

---

B.1	$X - Y$ proton arrival position . . . . .	180
B.2	Gas refractive index . . . . .	180
B.3	Mirror reflectance . . . . .	181
B.4	Lens transmission . . . . .	181
B.5	Quartz refractive index . . . . .	182
B.6	Photo-cathode sensitivity and QE . . . . .	182
B.7	PMT pulse height . . . . .	183



# Bibliography

- [1] J. de Favereau de Jeneret *et. al.*, *High energy photon interactions at the LHC*, arXiv:0908.2020v1 [hep-ph].
- [2] CMS coll., *The CMS experiment at the CERN LHC*, JINST 3 (2008), S08004.
- [3] M. Albrow *et. al.*, *The FP420 R&D Project: Higgs and New Physics with forward protons at the LHC*, arXiv:0806.0302v2 [hep-ex].
- [4] N. Schul, *Two-photon exclusive production of supersymmetric pairs at the LHC*, DESY-PROC-2009-03 (2010), 27.
- [5] N. Schul and T. Pierzchala, , Presentation at Lyon timing workshop.
- [6] N. Schul, *Exclusive production at LHC*, PoS DIS2010 (2010), 092.
- [7] J. Hollar, K. Piotrkowski and N. Schul, *Measurement of exclusive  $\gamma\gamma \rightarrow \mu^+\mu^-$  production at  $\sqrt{s}=7$  TeV*, CMS Note AN-2011-039.
- [8] N. Schul and K. Piotrkowski, *Detection of two-photon exclusive production of supersymmetric pairs at the LHC*, Nucl. Phys. Proc. Suppl. 179-180 (2008), 289.
- [9] K. Piotrkowski and N. Schul, *Two-photon exclusive production of supersymmetric pairs at the LHC*, arXiv:0910.0202 [hep-ph].
- [10] R. Brout and F. Englert, *Broken Symmetry and the Mass of Gauge Vector Mesons*, Phys. Rev. Lett. 13 (1964), 321
- [11] P. Higgs, *Broken symmetries, massless particles and gauge fields*, Phys. Lett. 12 (1964), o32  
P. Higgs, *Broken Symmetries and the Masses of Gauge Bosons*, Phys. Rev. Lett. 13 (1964), 508  
P. Higgs, *Spontaneous Symmetry Breakdown without Massless Bosons*, Phys. Rev. 145 (1966), 1156.

- [12] The LEP working group for Higgs Boson Searches, *Search for the Standard Model Higgs Boson at LEP*, Phys. Lett. B565 (2003), 61.
- [13] CDF coll. and D0 coll., *Combined CDF and DZero Upper Limits on Standard Model Higgs-Boson Production with up to 6.7 fb<sup>-1</sup> of Data*, arXiv:1007.4587
- [14] H. Goldberg, *Constraint on the Photino Mass from Cosmology*, Phys. Rev. Lett. 50 (1983), 1419.
- [15] J. Ellis, G. Ridolfi and F. Zwirner, *Radiative corrections to the masses of supersymmetric Higgs bosons*, Phys. Lett. B257 (1991), 83.
- [16] H. Flächer, *et. al.*, *Revisiting the Global Electroweak Fit of the Standard Model and Beyond with Gfitter*, Eur. Phys. J. C 60 (2009), 543.
- [17] CMS coll., *Search for new physics with the jets and missing momentum signature at the LHC*, CMS PAS SUS-10-005 (2010).
- [18] CMS coll., *Further interpretation of SUSY searches*, CMS PAS SUS-11-001 (2011).
- [19] CDF coll., *Observation of Exclusive Electron-Positron Production in Hadron-Hadron Collisions*, Phys.Rev.Lett. 98 (2007) 112001.
- [20] CDF coll., *Observation of Exclusive Charmonium Production and  $\gamma\gamma \rightarrow \mu^+\mu^-$  in  $p\bar{p}$  Collisions at  $\sqrt{s} = 1.96\text{TeV}$* , Phys.Rev.Lett. 102 (2009), 242001.
- [21] F. Cuypers *et. al.*, *Supersymmetric signals in  $\gamma\gamma$  collisions*, Nucl.Phys. B409 (1993), 144.
- [22] J. Ohnemus, T. Walsh and P. Zerwas,  *$\gamma\gamma$  Production of non-strongly interacting SUSY particles at hadrons colliders*, Phys.Lett. B328 (1994), 369.
- [23] S. Atag, S. Inan, I. Sahin, *Extra dimensions in  $\gamma\gamma \rightarrow \gamma\gamma$  at the CERN-LHC*, JHEP 09 (2010), 042.
- [24] S. Atag, S. Inan, I. Sahin, *Extra dimensions in photon-induced two lepton final states at the CERN-LHC*, Phys. Rev. D80 (2009), 075009.
- [25] T. Douglas, D. Wick, *Dirac magnetic monopole production from photon fusion in proton collisions*, Eur. Phys. J 39 (2009), 213.
- [26] M. Chaichian *et.al.*, *Searching for triplet Higgs sector via central exclusive production at the LHC*, JHEP 0905 (2009), 011.
- [27] T. Pierzchala and K. Piotrkowski, *Sensitivity to anomalous quartic gauge couplings in photon-photon interaction at the LHC*, Nucl. Phys. Proc. Suppl 179-180 (2008), 257.

- [28] C. Royon, E. Chapon, O. Kepka, *Anomalous quartic  $WW\gamma\gamma$ ,  $ZZ\gamma\gamma$  and trilinear  $WW\gamma\gamma$  couplings in two-photon processes at high luminosity at the LHC*, Phys. Rev. D81 (2010), 074003.
- [29] O. Kepka, C. Royon, *Anomalous  $WW\gamma$  coupling in photon-induced processes using forward detector at the LHC*, Phys. Rev. D 78 (2008), 073005.
- [30] I. Sahin, C. Inan, *Probe of unparticles at the LHC in exclusive two leptons and two photon production via photon-photon fusion*, JHEP 0909 (2009), 069.
- [31] A. Khoze *et al.*, *Luminosity monitors at the LHC*, Eur. Phys. J. C19 (2001), 313.
- [32] A. Shamov and V. Telnov, *Precision luminosity measurement at LHC using two-photon production of  $\mu^+ \mu^-$  pairs*, Nucl. Instrum. Meth. A494 (2002), 51.
- [33] S. Oryn, *Associated  $W$  and Higgs boson photoproduction and other electroweak photon induced processes at the LHC*, Nucl. Phys. Proc. Suppl 179-180 (2008), 269.
- [34] A. Baltz *et al.*, *Photoproduction at collider energies: from RHIC and HERA to LHC*, arXiv:hep-ph/0702212.
- [35] V. Goncalves, M. Machado, *Quarkonium production in coherent hadron-hadron interactions at the LHC*, Phys. Rev. D77 (2008), 014037.
- [36] M. Albrow, T. Coughlin and J. Forshaw, *Central exclusive production at high-energy hadron colliders*, Progress in Particle and Nuclear Physics (2010), 149.
- [37] The H1 and ZEUS coll., *DVCS and vector meson production at HERA*, Nucl. Phys. B Proc. Suppl 198 (2010) 67.
- [38] E. Fermi, *Über die Theorie des Stoßes zwischen Atomen und elektrisch geladenen Teilchen*, Z. Phys. 29 (1924), 315-327.
- [39] C.F von Weizsäcker, *Ausstrahlung bei Stoßen sehr schneller Elektronen*, Z. Phys. 88 (1934), 612-625.
- [40] E.J. Williams, *Correlation of certain collision problems with radiation theory*, Kgl. Danske Videnskab. Selskab Mat.-fys.Medd. (1935),No.4.
- [41] V. M. Budnev *et al.*, *The two-photon particle production mechanism. Physical problems. Applications. Equivalent Photon Approximation*, Phys.Rep. 15 (1975), 180.
- [42] K. Piotrkowski, *Tagging Two-Photon Production at the LHC*, Phys.Rev.D63 (2001), 071502; arXiv:hep-ex/0009065

- [43] K. Piotrkowski, *High-Energy Two-Photon Interactions at the LHC*, arXiv:ihep-ex/0201027
- [44] J. de Favereau de Jeneret, *Tests of the standard model in photoproduction at HERA and the LHC*, UCLouvain thesis.
- [45] The CDF coll., *Observation of Exclusive Dijet Production at the Fermilab Tevatron  $p$ - $\bar{p}$  Collider*, Phys.Rev.D77 (2008), 052004.
- [46] V. Khoze, A. Martin and M. Ryskin, *Prospects for New Physics observation in diffractive processes at the LHC and the Tevatron*, Eur. Phys. J. C 23 (2002), 311.
- [47] V. Khoze, A. Martin and M. Ryskin, *Photon exchange processes at hadron colliders as a probe of the dynamics of diffraction*, Eur. Phys. J. C 24 (2002), 459.
- [48] V. Khoze, A. Martin and M. Ryskin, *Insight into double-pomeron-exchange Higgs production and backgrounds*, Phys. Lett. B 650 (2007), 41.
- [49] V. Khoze, A. Martin and M. Ryskin, *Can the Higgs be seen in rapidity gap events at the Tevatron or the LHC?*, Eur.Phys.J. C14 (2000), 525.
- [50] S. Baranov *et. al.*, *LPAIR - A generator for lepton pair production*, Proceedings of "Physics at HERA" (1991), 1478.
- [51] J. Vermaseren, *Two-photon processes at very-high energies*, Nucl. Phys. B229 (1983), 347.
- [52] S. Stein *et.al.*, *Electron Scattering at 4-Degrees with Energies of 4.5-GeV - 20-GeV*, Phys. Rev. D12 (1975), 1884.
- [53] B. Andersson, G. Gustafson, G. Ingelman and T. Sjöstrand, *Parton fragmentation and string dynamics*, Phys. Rep. 97 (1983), 31.
- [54] T. Sjöstrand, , Computer Physics Commun. 82 (1994) 74.
- [55] F.W. Brasse *et.al.*, *Parametrization of the  $Q^2$  dependence of virtual gamma  $p$  total cross-sections in the resonance region*, Nucl. Phys. B110 (1976), 413.
- [56] A. Suri and D.R. Yennie, *The space-time phenomenology of photon absorption and inelastic electron scattering*, Annals Physics 72 (1972), 43.
- [57] G. Brona *et.al.*, *Measurement of the energy flow at large pseudo-rapidities at the LHC at  $\sqrt{s} = 900, 2360$  and  $7000$  GeV*, CMS Analysis Note 2010/023.
- [58] G. Mavromanolakis, *Quartz fiber calorimetry and calorimeters*, physics/0412123v1.

- 
- [59] A. Penzoa and Y. Onel, *The CMS-HF quartz fiber calorimeters*, J. Phys.: Conf. Ser. 160 (2009) 012014.
- [60] CMS-CASTOR group, *CASTOR Engineering Design Review* (2007).
- [61] X. Aslanoglou *et.al.*, *Performance studies of the final prototype for the CASTOR forward calorimeter at the CMS experiment*, CMS Note 2008/022.
- [62] B. Roland, *Forward physics capabilities of CMS with the CASTOR and ZDC detectors*, DIS 2009 proceedings.
- [63] O. Grachov *et.al.*, *Status of the Zero Degree Calorimeter for CMS experiment*, AIP Conf. Proc. 867 (2006) 258.
- [64] R. Hall-Wilton *et.al.*, *Forward Shower Counters (FSC) in CMS*, CMS Internal Note 2008/012.
- [65] M. Albrow, R. Hall-Wilton *et.al.*, *Physics and Beam Monitoring with Forward Shower Counters (FSC) in CMS*, CMS Note 2010/015.
- [66] M. Albrow, *Forward Shower Counters: Status*, presentation at Exclusive subgroup meeting (Feb. 2011)
- [67] W. Adam, B. Mangano, T. Speer *et.al.*, *Track reconstruction in the CMS tracker*, CMS Note 2006/041.
- [68] T. Speer, K. Prokofiev, R. Fruehwirth *et.al.*, *Vertex Fitting in the CMS Tracker*, CMS Note 2006/032.
- [69] R. Fruehwirth, W. Waltenberger, P. Vanlaer, *Adaptive Vertex Fitting*, CMS Note 2007/008.
- [70] J. Bernadini *et.al.*, *A data-driven measurement of primary vertex resolution and efficiency*, CMS Note 2010/201.
- [71] CMS coll., *Tracking and primary vertex results in first 7 TeV collisions*, CMS PAS TRK-10-005.
- [72] G. Abbiendi *et.al.*, *Muon reconstruction in the CMS detector*, CMS Analyses Note 2008/097.
- [73] M. Gallinaro, *Prospects for diffractive physics with the CDF forward detectors at the Tevatron*, arXiv:hep-ex/0205030
- [74] A. Brandt *et. al.*, *A forward proton detector at D0*, FERMILAB-PUB-97/377.
- [75] P. van Esch *et. al.*, *The H1 forward proton spectrometer at HERA*, Nucl. Inst. Meth. A446 (2000), 409.

- [76] O'. Shaughnerry *et. al.*, *Testing and installation of ZEUS leading proton spectrometers detector planes*, Nucl. Inst. Meth A342 (1994), 260.i
- [77] S. Bultmaan *et. al.*, *The PP2PP experiment at RHIC: silicon detector installed in Roman Pots for forward proton detection close to beam*, Nucl. Inst. Meth. A535 (2004), 415.
- [78] W. Guryn, *Physics with tagged protons at RHIC*, Proposal to STAR collaboration (2005).
- [79] J. Kalliopuska *et. al.*, *Resolution studies for the leading proton measurement in exclusive central diffraction at LHC*, HIP-2003-11/EXP (2003).
- [80] J. Alwall *et al.*, *MadGraph/MadEvent v4: The New Web Generation*, JHEP 0709:028 (2007).
- [81] J. de Favereau de Jeneret, X. Rouby and K. Piotrkowski, *HECTOR: A Fast simulator for the transport of particles in beamlines*, JINST 2: P09005 (2007), arXiv:0707.1198v1 [physics.acc-ph]
- [82] M. Albrow and A. Rostovtsev, *Searching for the Higgs Boson at Hadron Colliders using the Missing Mass Method*, arXiv:hep-ph/0009336.
- [83] S. Pattalwar *et. al.*, *New connection cryostat to insert FP420 proton tagging detectors in the LHC ring*, TUPMA001.
- [84] B. Cox, F. Loebinger and A. Pilkington, *Detecting Higgs bosons in the bb decay channel using forward proton tagging at the LHC*, JHEP 0710:090 (2007).
- [85] S. White, *On the Correlation of Subevents in the ATALS and CMS/Totem Experiments*, arXiv:0707.1500.
- [86] L. Bonnet, T. Pierzchala, K. Piotrkowski and P. Rodeghiero, *GASTOF: Ultra-fast ToF forward detector for exclusive processes at the LHC*, arXiv:hep-ph/0703320.
- [87] Loic Quertenmont and Vincent Roberfroid, *FROG: The Fast & Realistic OPENGL Displayer*, arXiv:0901.2718v1.
- [88] CMS BRM group, *Evaluation of the oscilloscope-based BPTX read-out during SPS operation*, CMS Internal Note 2007/047.
- [89] CMS coll., *Performance of muon identification in pp collisions at  $\sqrt{s}=7$  TeV*, CMS PAS MUO-10-002 (2010).

- [90] S. Klein and J. Nystrand, *Photoproduction of quarkonium in proton proton and nucleus nucleus collisions*, Phys. Rev. Lett. 92 (2004) 142003  
J. Nystrand, *Photons and exclusive processes at hadron colliders*, Photon 2009 proceedings (2009), 286. arXiv:1011.1420 [hep-ph].
- [91] C. Amsler *et al.* (Particle Data Group), Phys. Lett. B667, 1 (2008).
- [92] <http://projects.hepforge.org/superchic>
- [93] L. Harland-Lang, V. Khoze, M. Ryskin, W. Stirling, *Central exclusive  $\chi_{c0}$  meson production at the Tevatron revisited*, Eur.Phys.J.C65 (2010), 433.
- [94] L. Harland-Lang, V. Khoze, M. Ryskin, W. Stirling, *Standard candle central exclusive processes at the Tevatron and LHC*, Eur.Phys.J.C69 (2010), 179.
- [95] L. Harland-Lang, V. Khoze, M. Ryskin, W. Stirling, *Central exclusive quarkonium production with tagged forward protons at RHIC*, Eur.Phys.J.C71 (2011), 1545.
- [96] CLEO coll., *Measurements of branching fractions for electromagnetic transitions involving the  $\chi_{bJ}(1P)$  states*, Phys.Rev.D83 (2011), 054003.
- [97] M. Mulders *et.al.*, *Muon Identification in CMS*, CMS Note 2008/098.
- [98] M. Rangel *et.al.*, *Diffractional  $\chi$  production at the Tevatron and the LHC*, Nucl. Phys. B774 (2007), 53.
- [99] CMS coll., *Absolute Calibration of Luminosity Measurement at CMS*, CMS Note AN-2010/093.
- [100] CMS coll. *Study of W and Z Boson Production at 7 TeV*, CMS PAS EWK-10-005.
- [101] H1 coll., *Muon pair production in ep collisions at Hera*, H1-prelim-02-061 (2002).
- [102] CDF coll., *First observation of exclusive electron pairs in hadron-hadron collisions*, CDF Note 8225 (2006).
- [103] LHCb coll., *Exclusive dimuon production at LHCb*, presentation at DIS11.
- [104] B. Cox, J. Forshaw, *POMWIG : HERWIG for diffractive interactions*, Comput.Phys.Commun.144 (2002), 104.
- [105] A. Goto and T. Kon, *Supersymmetric Particle Production at the TeV $\gamma\gamma$  Collider*, Europhys.Lett. 13 (1990), 211-215.

- 
- [106] Y. Andreev *et al.*, *Using  $\ell^+\ell^- + E_T^{\text{miss}} + \text{jet veto}$  signature for slepton detection*, CMS Note 2006/132.
- [107] M. Ibe, R. Kitano, *Sweet Spot Supersymmetry*, JHEP 0708:16 (2007).
- [108] M. Fairbairn *et al.*, *Stable Massive Particles at Colliders*, Phys. Rept. 438 (2007) 1.
- [109] Optics for Research data, [http://www.ofr.com/oc-12\\_metal\\_mirror.htm](http://www.ofr.com/oc-12_metal_mirror.htm)
- [110] Edmund Optics data, <http://www.edmundoptics.com/images/catalog/7011.gif>
- [111] W. Coode-Adams, *The refractive index of quartz*, Proceedings of the Royal Society of London. Series A, Vol. 117, Num 776 (1927), 209.
- [112] Hamamatsu data, [http://sales.hamamatsu.com/assets/pdf/parts\\_R/R3809U-50.TPMH1067E08.pdf](http://sales.hamamatsu.com/assets/pdf/parts_R/R3809U-50.TPMH1067E08.pdf)